Two-component Bose-Einstein condensates with competing interactions

by

Julio Sanz Sánchez

A thesis submitted in fulfillment of the requirements for the degree of Doctor of Philosophy in Photonics

Thesis supervisor: Prof. Dr. Leticia Tarruell
Ultracold Quantum gases group

The Barcelona Institute of Science and Technology - BIST
Institut de Ciències Fotòniques - ICFO
Universitat Politècnica de Catalunya - UPC

Chapter 3

Quantum liquid droplets in a mixture of Bose-Einstein condensates

Abstract

Quantum droplets are small clusters of atoms self-bound by the balance of attractive and repulsive forces. Here, we report on the observation of droplets solely stabilized by contact interactions in a mixture of two Bose-Einstein condensates. We demonstrate that they are several orders of magnitude more dilute than liquid helium by directly measuring their size and density via in situ imaging. We show that the droplets are stablized against collapse by quantum fluctuations and that they require a minimum atom number to be stable. Below that number, quantum pressure drives a liquid-to-gas transition which we map out as a function of interaction strength. These ultradilute isotropic liquids remain weakly interacting and constitute an ideal platform to benchmark quantum many-body theories.

Since the work explained in this chapter was detailed in the thesis from my predecessor C. R. Cabrera [65] and was published in reference [29], in the following chapter I will reproduce large fractions of the

article and its supplementary material without major modifications.

3.1 Introduction

In this chapter, we study the formation of composite quantum droplets stabilized by beyond mean field effects in a Bose-Einstein condensate with competing inter-actions [28]. In this system, repulsive intra-component interactions and attractive inter-component interactions can be adjusted so that the residual mean field in-teractions remain weakly attractive and comparable to the repulsive contribution stemming from quantum fluctuations. Strikingly, this leads to the formation of an ultra-dilute self-bound quantum liquid droplet in the weakly interacting regime, as proposed in 2015 by D. S. Petrov [28].

Previously the study of quantum liquids had been restricted to liquid Helium. For small particle numbers Helium forms nanometer-sized liquid droplets with a density such that the mean inter-particle distance is comparable to the effective range of the inter-atomic potential. Understanding their properties, which di-rectly reflect their quantum nature, is challenging and requires a good knowledge of the short-range details of the inter-atomic potential [113, 114]. Interestingly, ultracold atomic droplets are 8 orders of magnitude more dilute and their prop-erties can be described universally with the inter and intra-component scattering lengths to first approximation [28]. Therefore, these ultra-dilute systems enable a much simpler microscopic description, while remaining in the weakly interacting regime. They are thus amenable to well controlled theoretical studies of beyond mean field effects.

Shortly after the proposal from D. S. Petrov, ultra-dilute liquid droplets were observed in ultracold dipolar systems by the groups of T. Pfau, with Dysprosium (^{164}Dy), and F. Ferlaino, with Erbium (^{166}Er) atoms. In this system, repulsive s-wave interactions and attractive dipolar interactions can be tuned, depending on the trapping geometry, so that the residual mean field attraction is balanced with the repulsion stemming from quantum fluctuations. These experiments were followed by our observation of quantum droplets in a Bose-Bose mixture formed by two internal states of ^{39}K in a quasi-2D and quasi-1D geometries [29, 30] at first, and in a 3D geometry by the LENS group shortly afterwards [31]. Whereas

for dipolar systems, the anisotropic character of the magnetic dipole-dipole force leads to the formation of filament-like self-bound droplets with highly anisotropic properties [50, 115, 116], for Bose-Bose mixtures the contact character of the interactions makes the droplets isotropic [28].

This chapter is organized as follows. In section 3.2, we will introduce the theoretical framework to understand the beyond mean field origin responsible for the stabilization of quantum liquid droplets in composite mixtures. Then, in section 3.3 we will introduce the state of the art on another type of ultracold quantum liquids: dipolar droplets. Subsequently, in section 3.5 we will present our work on the observation of composite quantum liquid droplets in a mixture of Bose-Einstein condensates in a quasi-2D geometry. The conclusions that we obtained from the comparison between experiment and theory will be introduced in section 3.6 and contrasted in section 3.7 to the experiments performed at LENS and the possible beyond LHY effects [117–119]. Finally, in section 3.8 we present the possibility of future experiments opened up by our work.

3.2 Theoretical framework

3.2.1 Stabilization of composite quantum droplets through quantum fluctuations

The stabilization of attractively interacting gases requires the existence of a repulsive force which prevents the system from collapsing. To illustrate the stabilization mechanism of quantum droplets we will start by introducing the physics of homogeneous Bose gases with attractive interactions. For a single component BEC with attractive interactions the mean field energy per unit volume $\mathcal{E}_{\mathrm{MF}} = E_{\mathrm{MF}}/V = \frac{1}{2}gn^2$ is reduced when the density increases, where $g = 4\pi\hbar^2 a/m$ is the interaction strength. Thus, the condensate will tend to collapse into a single point with infinite density. Before the BEC reaches an infinite density, three-body recombination processes induce losses at high densities [120, 121] and the BEC will be lost.

The collapse of the condensate can also be understood from the excitation spectrum of the system, also known as the Bogoliubov spectrum. When the

interactions in a BEC are attractive, the Bogoliubov spectrum at low momentum is imaginary and therefore the system becomes mechanically unstable. As a consequence, very small fluctuations in the density of the condensate grow exponentially due to the attractive non-linearity and induce the collapse of the BEC.

For a two-component BEC with repulsive inter-component and attractive intra-component interactions, the mean field energy density of the system is $\mathcal{E}_{\mathrm{MF}} = \frac{1}{2}g_{\uparrow\uparrow}n_\uparrow^2 + \frac{1}{2}g_{\downarrow\downarrow}n_\downarrow^2 + g_{\uparrow\downarrow}n_\uparrow n_\downarrow$, where we have identified the two components as $\uparrow$ and $\downarrow$ and $g_{\uparrow\uparrow}$, $g_{\downarrow\downarrow}$ and $g_{\uparrow\downarrow}$ correspond to the inter-component and intra-component interaction strengths respectively. The mean field energy of the system can be rewritten in such a way that there is a contribution depending on the sum and difference of the density of the components $\mathcal{E}_{MF} \propto g(n_\uparrow - n_\downarrow)^2 + \frac{\delta g}{2}(n_\uparrow + n_\downarrow)^2$, where we have considered the case where $g_{\uparrow\uparrow} = g_{\downarrow\downarrow} = g$ for simplicity and $\delta g = g_{\uparrow\downarrow} + \sqrt{g_{\uparrow\uparrow}g_{\downarrow\downarrow}}$. When $\delta g < 0$, the minimization of the energy of the system has two consequences. To reduce the energy of the sum term, the system tends to lock the ratio between the densities. Generally, the density ratio is locked to $n_\uparrow/n_\downarrow = (g_{\downarrow\downarrow}/g_{\uparrow\uparrow})^{1/2}$. To reduce the energy of the difference term, the system tends to increase the density until collapse is reached.

The same phenomena can be understood from the Bogoliubov spectrum. For a two component BEC, the spectrum contains two sound branches. The lowest energy branch is known as the soft branch and corresponds to the density excitations. The highest energy branch, known as the hard mode, corresponds to the spin excitations. To minimize spin excitations the density ratio adjusts to $n_\uparrow/n_\downarrow = (g_{\downarrow\downarrow}/g_{\uparrow\uparrow})^{1/2}$. When $\delta g < 0$ the soft branch becomes imaginary at low momenta and the BEC tends to collapse.

Up to now we have only considered the physics of attractive condensates at the mean field approximation. What happens if we take into account beyond mean field corrections? The first correction to the mean field energy corresponds to the zero point motion energy of the Bogoliubov excitations. In other words, the vacuum of Bogoliubov phonons in a condensate has a finite energy due to the presence of quantum fluctuations. This correction to the energy was first computed for a single component BEC by T.D Lee, K. Huang and C. N. Yang [122], and is commonly known as the Lee-Huang-Yang (LHY) energy. In the

single component case the LHY energy density is proportional to $(gn)^{5/2}$, and thus for small gas parameters $na^3 \ll 1$, the LHY energy is really small and not able to prevent the collapse of an attractive BEC.

In this case of a two-component BEC the interaction energy for the attractive two-component BEC contains two contributions. The residual mean field attraction $\mathcal{E}_{\text{MF}} \propto \delta g \; n^2$, and the repulsive contribution from quantum fluctuations $\mathcal{E}_{\text{LHY}} \propto (gn)^{5/2}$, which is also known as the LHY correction. Although this correction to the mean field energy is a very small correction in the weakly interacting regime, it scales with the interaction strength g, whereas the MF energy density scales with δg. Therefore, both terms can stabilize the system into a self-bound quantum droplet. In other words, although the soft branch induces a mechanical instability, the spin branch remains hard and the LHY correction is able to prevent the collapse of the condensates and stabilize the system into a quantum liquid droplet. In analogy to classical liquids, these droplets are self-bound even in the absence of a trapping container.

In the weakly interacting regime, the equilibrium density of the system at which the two contributions balance is such that $n_{\text{eq}} \propto (\delta g)^2/g^5$. Typical equilibrium densities of these droplets are orders of magnitude much more dilute than liquid Helium and are denser than common BECs.

Up to now we have only discussed the stabilization of quantum droplets in homogeneous systems. But what happens if we put quantum droplets in a trap? If the harmonic oscillator length is bigger than the size of the droplets, the system is in 3D and the physics of the droplets are essentially described by the high atom number limit where trapping and kinetic energies can be neglected. Indeed, in this regime, the density of quantum droplets shows a flat-top profile followed by a surface with a thickness on the order of the density healing length ξ_d.

For smaller atom numbers the flat-top density profile disappears and the droplet has a gaussian shape with a size on the order of ξ_d, see Fig. 3.1 (a). In this regime, the kinetic energy of the droplet must be taken into account. Indeed, for very small atom numbers the system cannot be self-bound anymore. While $\mathcal{E}_{\text{LHY}} \propto N^{5/2}$ and $\mathcal{E}_{\text{MF}} \propto N^2$, the kinetic energy density $\mathcal{E}_{\text{K}} \propto N$. Hence, at very low atom numbers the kinetic energy becomes more relevant and drives a liquid to gas phase transition.

If the mixture is strongly confined we can reduce the dimensionality of the system. Since composite quantum droplets have two excitation branches, there are two healing lengths associated with the droplets. The density and spin healing lengths $\xi_d = \hbar/\sqrt{2}mc_d$ and $\xi_s = \hbar/\sqrt{2}mc_s$, where c_d and c_s are the corresponding density and spin velocities. Therefore, the mixture can have a different dimensionalities for the density and spin degrees of freedom. In the experiments described in this chapter, we work in a trapping geometry which is in the quasi-2D regime with respect to the density degrees of freedom and 3D with respect to the spin degrees of freedom. This is because for $\delta g \sim 0$, the density branch softens and the associated healing length ξ_d becomes large. Instead, the spin branch remains hard. Hence, we will take into account the LHY correction in 3D.

To do a proper analysis of the phase diagram of quantum droplets we will introduce a variational calculation of an extended Gross-Pitaevskii equation where we have included the effect of quantum fluctuations as an effective potential. Before doing so, let us introduce the particular excitation spectrum of homogeneous droplets.

3.2.2   Excitation spectrum

The composite quantum droplets are predicted to have a peculiar excitation spectrum. In figure 3.1 (b) the different modes $\tilde{\omega}_l$ are shown as a function of the total atom number above the critical atom number, where l represents the angular momentum. The $l = 0$ mode, in red, represents the breathing mode and the modes with $l > 1$ represent the surface modes. The $l = 1$ mode corresponds to the dipole/center-of-mass mode. The spectrum was computed in the absence of a trap. Hence, $\tilde{\omega}_{l=0} = 0$.

Together with the excitation spectrum, the chemical potential is represented in blue. For energies above this limit, it is energetically more favorable to remove particles from the droplet than exciting a particular mode. For this reason, the chemical potential sets the particle emission threshold. This has particular consequences for the range of atom numbers denoted with the gray area, where no modes are present below the particle emission threshold. Therefore, in this regime, it is not possible to excite the quantum droplet since any excitation will result in the evaporation of particles in order to minimize the energy. Hence,

quantum droplets can be regarded as true zero temperature macroscopic objects in this regime. Just above the no-excitation regime, the excitation of the breathing mode is not possible since the compressibility of this liquid phase is very small and it requires a lot of energy to modify the density of the droplets. It is not until larger atom numbers when the excitation of the breathing mode is comparable in energy with very high angular momentum modes.
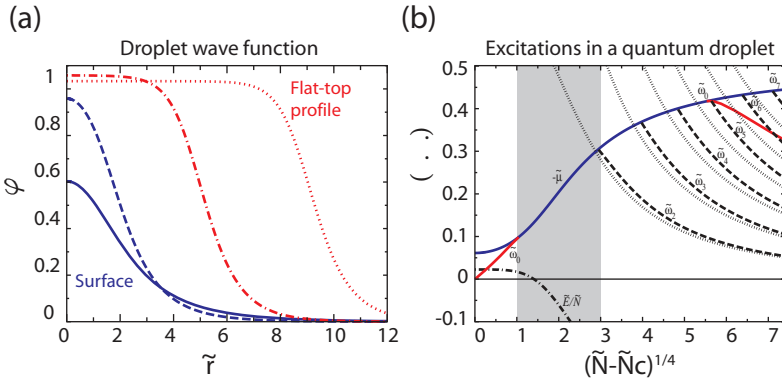

Figure 3.1: Figures taken from [65] which were reproduced from ref. [28]. (a) For large atom number a flat-top density profile, an inherent property of a liquid, is expected to occur. For low atom number, if the saturation density is not reached, the density profile is mainly dominated by surface effects. (b) The excitation spectrum of an isotropic droplet. The different modes are sketched. The dashed blue line represents the boundary between discrete modes and the continuum. The gray area represents the region where no excitations exist. The axes are presented in rescaled units, see [28] for details.

In the next section, we study the properties of these quantum droplets using an extended Gross-Pitaevskii equation which we have solved variationally. Since our experiments have been performed with composite mixtures with equal mass, we will focus on this regime.

3.2.3 Extended Gross-Pitaevskii equation with quantum fluctuations

Following ref. [28] and the supplementary material from ref. [30], we can describe a weakly interacting Bose-Bose mixture with balanced repulsive intra-component and attractive inter-component interactions with an extended single particle Gross-Pitaevskii equation (eGPE). This equation includes the effect of quantum fluctuations as an effective repulsive potential and assumes an identical spatial wavefunction ϕ for both components (modulo a normalization factor). Since we will work with equal mass components, from now on we will describe the physics of the interacting system in terms of the intra and inter-component scattering lengths $a_{\uparrow\uparrow}$, $a_{\downarrow\downarrow}$ and $a_{\uparrow\downarrow}$. It is important to remark that the eGPE equation that we will introduce is only valid under the following approximations.

- The weakly interacting approximation $na_{\uparrow\uparrow}^3$, $na_{\downarrow\downarrow}^3$, $n|a_{\uparrow\downarrow}|^3 \ll 1$.

- The balanced regime where $\sqrt{a_{\uparrow\uparrow}a_{\downarrow\downarrow}} \approx -a_{\uparrow\downarrow}$ and $a_{\uparrow\uparrow} \approx a_{\downarrow\downarrow} \approx -a_{\uparrow\downarrow}$.

- The density ratio condition $n_\uparrow/n_\downarrow \approx \sqrt{a_{\downarrow\downarrow}/a_{\uparrow\uparrow}}$.

Here, we assume identical spatial modes for the two components $\left(\Psi_\uparrow = \sqrt{n_\uparrow}\phi\right.$ and $\left.\Psi_\downarrow = \sqrt{n_\downarrow}\phi\right)$, and the density ratio $n_\uparrow/n_\downarrow = \sqrt{a_{\downarrow\downarrow}/a_{\uparrow\uparrow}}$ which minimizes the energy of the hard branch [28, 123]. For this reason, the problem is simplified into a single-particle eGPE and thus spin excitations cannot be described with this model.

The energy density functional of the system reads

$$
\begin{aligned}
\mathcal{E} &= \mathcal{E}_\mathrm{P} + \mathcal{E}_\mathrm{K} + \mathcal{E}_\mathrm{MF} + \mathcal{E}_\mathrm{LHY} \\
&= V_\mathrm{ext}n_0|\phi|^2 + \frac{\hbar^2}{2m}n_0|\nabla\phi|^2 + \frac{4\pi\hbar^2\delta a}{m}\frac{\sqrt{a_{\downarrow\downarrow}/a_{\uparrow\uparrow}}}{(1+\sqrt{a_{\downarrow\downarrow}/a_{\uparrow\uparrow}})^2}n_0^2|\phi|^4 \\
&+ \frac{256\sqrt{\pi}\hbar^2}{15m}\left(\frac{n_0\sqrt{a_{\uparrow\uparrow}a_{\downarrow\downarrow}}}{1+\sqrt{a_{\downarrow\downarrow}/a_{\uparrow\uparrow}}}\right)^{5/2}f\left(1,\frac{a_{\uparrow\downarrow}^2}{a_{\uparrow\uparrow}a_{\downarrow\downarrow}},\sqrt{\frac{a_{\downarrow\downarrow}}{a_{\uparrow\uparrow}}}\right)|\phi|^5
\end{aligned}
\tag{3.2.1}
$$

where $n_0 = n_\uparrow + n_\downarrow$ and $\mathcal{E}_\mathrm{P}$, $\mathcal{E}_\mathrm{K}$, $\mathcal{E}_\mathrm{MF}$ and $\mathcal{E}_\mathrm{LHY}$ denote the potential, kinetic, mean-field and quantum fluctuation (Lee-Huang-Yang) contributions to

the energy density of the mixture, respectively. Here the equal mass factor is $f(1, x, y) = \sum_{\pm} \left[1 + y \pm \sqrt{(1-y)^2 + 4xy)} \right]^{5/2} / 4\sqrt{2}$. This energy functional results in an extended Gross-Pitaevskii equation given by

$$i\hbar\dot{\phi} = \left[-\frac{\hbar^2}{2m}\nabla^2 + V_{\text{ext}} + \alpha n_0 |\phi|^2 + \gamma n_0^{3/2} |\phi|^3 \right] \phi, \qquad (3.2.2)$$

where α and γ of the two last terms are defined as

$$
\begin{aligned}
\alpha &= \frac{8\pi\hbar^2 \delta a}{m} \frac{\sqrt{a_{\downarrow\downarrow}/a_{\uparrow\uparrow}}}{(1 + \sqrt{a_{\downarrow\downarrow}/a_{\uparrow\uparrow}})^2}, \\
\gamma &= \frac{128\sqrt{\pi}\hbar^2}{3m} \left(\frac{\sqrt{a_{\downarrow\downarrow}a_{\uparrow\uparrow}}}{1 + \sqrt{a_{\downarrow\downarrow}/a_{\uparrow\uparrow}}} \right)^{5/2} f\left(1, \frac{a_{\uparrow\downarrow}^2}{a_{\uparrow\uparrow}a_{\downarrow\downarrow}}, \sqrt{\frac{a_{\downarrow\downarrow}}{a_{\uparrow\uparrow}}}\right).
\end{aligned}
\qquad (3.2.3)
$$

In the following section we describe the variational approach that we used to solve the eGPE including quantum fluctuations.

Variational Gaussian ansatz

The variational calculations developed in this section were performed by P. Cheiney, C. R. Cabrera and L. Tarruell.

To obtain the ground state phase diagram given by Eq. (3.2.1) we use a variational technique. As we will show in section 3.5 the droplets that we have been able to observe experimentally are not in the high atom number regime, and neither the kinetic nor the potential energies can be neglected. Therefore, the droplets that we have observed do not show a flat-top profile and are well described by a gaussian ansatz:

$$\psi(x, y, z) = \sqrt{n_0}\phi(x, y, z) = \sqrt{n_0} \exp\left(-\frac{x^2}{2\sigma_x^2} - \frac{y^2}{2\sigma_y^2} - \frac{z^2}{2\sigma_z^2} \right) \qquad (3.2.4)$$

where n_0 is the peak density of the system normalized through the condition $n_0 = N/\pi^{3/2}\sigma_x\sigma_y\sigma_z$.

Thus, the functional for the total energy $E = \int \mathcal{E}d^3r$ per particle that we

obtain is:

$$
\begin{aligned}
\frac{E(\sigma_x, \sigma_y, \sigma_z)}{N\hbar\omega_z} &= \frac{1}{N\hbar\omega_z}\left(E_{\mathrm{P}} + E_{\mathrm{K}} + E_{\mathrm{MF}} + E_{\mathrm{LHY}}\right) \\
&= \frac{1}{4}\left(\frac{\lambda_x^2\sigma_x^2}{a_{\mathrm{ho},z}^2} + \frac{\lambda_y^2\sigma_y^2}{a_{\mathrm{ho},z}^2} + \frac{\sigma_z^2}{a_{\mathrm{ho},z}^2}\right) + \frac{1}{4}\left(\frac{a_{\mathrm{ho},z}^2}{\sigma_x^2} + \frac{a_{\mathrm{ho},z}^2}{\sigma_y^2} + \frac{a_{\mathrm{ho},z}^2}{\sigma_z^2}\right) \\
&\quad + \frac{1}{\sqrt{2\pi}}\frac{Na_{\mathrm{ho},z}^3}{\sigma_x\sigma_y\sigma_z}\left(\frac{2\sqrt{a_{\downarrow\downarrow}/a_{\uparrow\uparrow}}\,\delta a}{\left(1 + \sqrt{a_{\downarrow\downarrow}/a_{\uparrow\uparrow}}\right)^2 a_{\mathrm{ho},z}}\right) \\
&\quad + \sqrt{\frac{2}{5}}\frac{512}{75\pi^{7/4}}\frac{N^{3/2}a_{\mathrm{ho},z}^{9/2}}{(\sigma_x\sigma_y\sigma_z)^{3/2}}\left(\frac{\sqrt{a_{\uparrow\uparrow}a_{\downarrow\downarrow}}}{a_{\mathrm{ho},z}(1 + \sqrt{a_{\downarrow\downarrow}/a_{\uparrow\uparrow}})}\right)^{5/2} \\
&\quad\quad f\left(1, \frac{a_{\uparrow\downarrow}^2}{a_{\uparrow\uparrow}a_{\downarrow\downarrow}}, \sqrt{\frac{a_{\downarrow\downarrow}}{a_{\uparrow\uparrow}}}\right),
\end{aligned}
$$

(3.2.5)

where $\lambda_x = \omega_x/\omega_z$, $\lambda_y = \omega_y/\omega_z$ and we have normalized the total energy by the harmonic oscillator $a_{\mathrm{ho},z} = \sqrt{\hbar/m\omega_z}$ without loss of generality. To obtain the ground state of the droplets for particular interaction strengths and atom numbers, we should minimize the energy E vs. σ_x, σ_y and σ_z.

Ground state phase diagram

To show the liquid character of quantum droplets we will compute the ground state phase diagram in the absence of a trap. In such situation the system is isotropic and therefore $\sigma_x = \sigma_y = \sigma_z = \sigma$. With this assumption we minimize numerically Eq. (3.2.5) using the relevant interaction parameters in the mixture of ^{39}K as an example (see section 3.5 for details). In Fig. 3.2, we show the energy of the mixture as a function of σ (green line). For a total atom number $N = N_\uparrow + N_\downarrow$ and interaction strength $\delta a < 0$ the cloud does not collapse, as expected from mean-field theory, but instead minimizes the energy forming a system with finite size. This self-bound phase in the absence of trapping potential is what we identify as quantum liquid droplet.

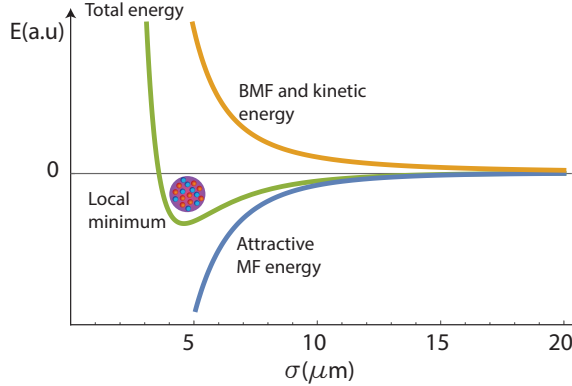Without the presence of the BMF contribution (yellow line), the energy is

Figure 3.2: Figures taken from [65]. The green line represents the total energy of the system for $N = 5 \cdot 10^5$ and $\delta a = -2.88\, a_0$ as a function of the size σ. We observe that a local minimum appears for a given width. The stabilization of a self-bound state in the absence of a trap is what we call quantum droplet.

minimized for zero size and thus the mixture would collapse. Due to the competition of the kinetic and beyond mean field repulsion (yellow line) and mean field attraction (blue line), a stable minimum appears.

In Fig. 3.3 (a) we depict the droplet energy as a function of the total atom number. We find that the droplet becomes metastable $E_{\mathrm{droplet}} > 0$ (shaded area) by decreasing the atom number. For a critical value N_c the minimum in energy disappears. In Fig. 3.3 (b) we show the minima in energy for a stable droplet (green) and metastable droplet (red). Below N_c, the minimum in energy disappears and there is a liquid-to-gas phase transition.

Following refs. [28, 33, 49, 124], we attribute this liquid-to-gas phase transition to the effect of quantum pressure, which acts as a repulsive force. As the atom number decreases, the relative weight between kinetic ($\mathcal{E}_{\mathrm{K}}$) and interaction energies ($\mathcal{E}_{\mathrm{MF}}$, $\mathcal{E}_{\mathrm{LHY}}$) changes. Each energy term scales differently with N: $\mathcal{E}_{\mathrm{K}} \propto N$, $\mathcal{E}_{\mathrm{MF}} \propto N^2$ and $\mathcal{E}_{\mathrm{LHY}} \propto N^{5/2}$. Below a critical atom number, kinetic effects become sufficiently strong to drive this transition. For a fixed atom number, if we reduce the attraction strength the kinetic energy also drives a liquid to gas transition. The larger the attraction the more stable droplets are, and thus the critical atom number is reduced for increasing attraction. These effects can
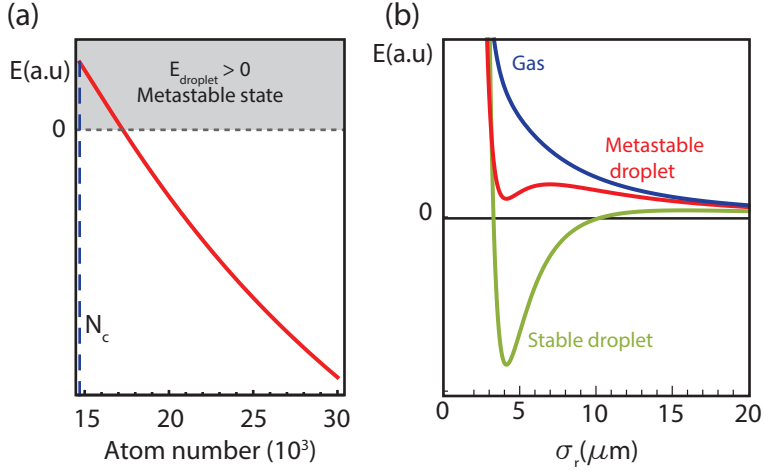
Figure 3.3: Figures taken from [65]. (a) Droplet energy as a function of atom number. We observe that for low atom number the droplet becomes metastable ($E_{\mathrm{droplet}} > 0$) and then unstable for a critical atom number N_c. (b) Droplet minima for three different values of N. For large atom number ($N > N_c$) the droplet is stable (green line). Close to the critical atom number $N \sim N_c$ the droplet becomes metastable (red line). Finally for low atom number ($N < N_c$) the droplet dissociates into a gas.

be seen from the density landscape that we plot in Fig. 3.4 (a) as a function of the total atom number N and residual attraction δa. In Fig. 3.4 (b) we show the evolution of the droplet width as a function of atom number for two different interaction strengths δa. For a critical atom number N_c (depicted as a shaded area) the width of the droplet diverges.

For smaller atom numbers the stable phase is a gas which is interesting on its own. Although the LHY repulsion is not able to stabilize the system into a droplet the mean field attraction is not able to make the gas collapse. Instead a single component attractive BEC would collapse in the absence of a trap. Therefore the absence of collapse of the gas is a signature of the effect of the beyond mean field stabilization.
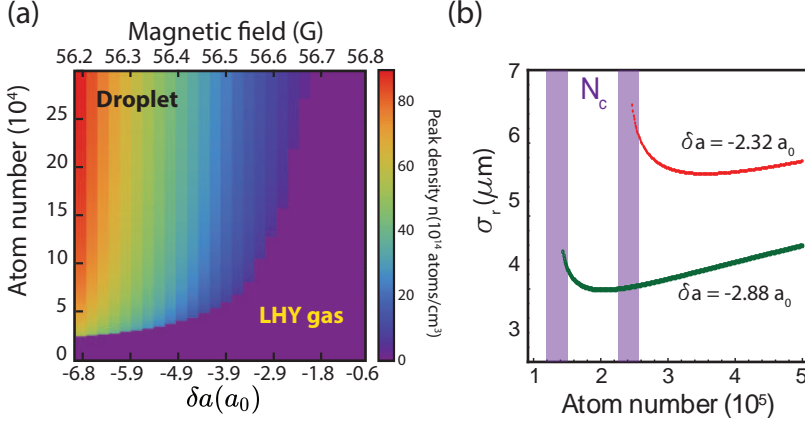
Figure 3.4: Figures modified from ref. [65](a) Phase diagram of a ^{39}K Bose-Bose mixture for $\delta a < 0$. Depending of the critical atom number and interaction strength the system could form a quantum liquid droplet or remain in the LHY gas phase. Notice that the $\delta a(a_0)$ axis is not in a linear scale. For comparison we show the corresponding magnetic field in the top axis (see also Fig. 3.5(a)). (b) For a critical atom number N_c the system dissociates into a gas. This is depicted in the shaded area where the width of the droplet diverges.

3.3 State of the art on dipolar droplets

The first observation of dipolar droplets was performed with ^{164}Dy atoms in a regime where a mechanical instability should occur and a collapse of the condensate was expected. Instead, the "crystallization" of a dipolar condensate into structured dipolar drops was reported [32]. This self-organized structure was made of several long-lived dipolar droplets that repelled each other, in analogy to classical ferrofluids [125]. Indeed, the observation of dipolar droplets at the time was unexpected, and the origin of the stabilization mechanism was not clear.

Different stabilization mechanisms had been proposed so far for the stabilization of ultradilute liquid droplets, including a repulsion stemming from three-body correlations [126] and quantum fluctuations [28]. The observation of a single stable dipolar droplet was reported [127] in a study where they measured the density scaling of the droplets as a function of the interaction strength to distinguish between the two stabilization mechanisms. The experiments showed

that the stabilization of dipolar droplets could not be explained by considering a three-body repulsion and that the repulsion stemming from quantum fluctuations were compatible with the experimental observations.

This dilute liquid phase has been characterized thoroughly in terms of the total atom number, interaction strength and trap geometry. Depending on the aspect ratio of the trap $\lambda = \omega_z/\omega_\rho$ (where dipoles are oriented along z), the Bose-Einstein condesate can adiabatically connect into a single self-bound droplet for λ above a critical value λ_c [49, 50] as shown in [128, 129] with ^{164}Dy and with ^{166}Er [34]. Below λ_c a modulation instability can lead to the formation of a structured array of dipolar droplets as previously observed in [32]. An experimental study analyzing the phase diagram for the different interaction strengths and trapping geometries regimes was reported in reference [130].

The stability of dipolar quantum droplets also depends on the atom number. Below a critical atom number, quantum pressure can dissociate the liquid droplets into a gas. In reference [33] the liquid-to-gas phase diagram for $\lambda > \lambda_c$ was explored with droplets formed by ~ 1000 atoms. Although the results agreed qualitatively with the extended Gross-Pitaevskii description including the LHY correction, the quantitative fit to the experiment revealed a background scattering length $a_{bg} = 62.5a_0$ which was not compatible with previous measurements ($a_{bg} = 122(10)a_0$) [131].

The peculiar excitation spectrum of ultra-cold quantum droplets is one of the properties which are objects of attention [28]. However, it has been shown theoretically that dipolar droplets do not exhibit the no-excitation regime proposed originally for composite droplets [50, 132]. Nevertheless, the collective modes of an ^{166}Er droplet have been measured to confirm the importance of the LHY repulsion as a key stabilization mechanism [34]. Experiments performed with ^{164}Dy have also explored the collective modes of the droplet. Here they focused in particular in the scissor mode [133]. By measuring the frequency of the scissor mode they extracted the background scattering length of ^{164}Dy to be $a_{bg} = 69(4)a_0$.

Currently, the study of dipolar droplets has been focusing on the search for a supersolid phase. This phase is characterized by the spontaneous symmetry breaking of phase and translational invariance, meaning that a periodic array of dipolar superfluid droplets sharing a common global phase could be formed.

The existence of such phase involves a very subtle balance of the softening of the roton mode. Although the initial observations of a "crystalline" droplet phase were pointing at the presence of a supersolid, the experimental evidence showed no phase coherence between the different drops [32]. However, later on, L. Tanzi *et al.* showed in reference [134] with ^{162}Dy that a metastable striped dipolar system with a global phase coherence can be formed by tuning the interactions in a narrow range near the roton instability. Since then, several works have been published on the study of the supersolid phase with dipolar droplets. This includes the observation of the *in situ* density modulation together with the measurement of global phase coherence [119] and the measurement of its excitation spectrum [135, 136].

Although the stabilization mechanism of dipolar and composite quantum droplets has the same origin, the anisotropy of dipolar interactions has strong implications on the physics of dipolar droplets. Complementary, our work represents the study of isotropic quantum droplets which are only stabilized by contact *s*-wave interactions.

3.4 Experimental challenges

In order to observe composite quantum liquid droplets, there are several challenges which must be overcome. First of all, we need to find the appropriate atomic species where $g_{\uparrow\uparrow} > 0$, $g_{\downarrow\downarrow} > 0$, $g_{\uparrow\downarrow} < 0$ and $\delta g < 0$. There are several mixtures which satisfy this condition, including heteronuclear mixtures: ^{41}K-^{87}Rb [137, 138],^{39}K-^{87}Rb [139], ^{39}K-^{23}Na [140]; and homonuclear mixtures of ^{39}K and ^{41}K [75]. In our experiment, we initially observed a hint of quantum droplets in ^{41}K but decided to perform the experiments with a spin mixture of ^{39}K in the $m_F = 0$ and $m_F = -1$ states of the $F = 1$ manifold since the magnetic field range where $\delta g < 0$ is broader as pointed out in ref. [65].

Another challenge to observe quantum droplets is that their size is on the order of 1 μm. Therefore we need to use a high resolution imaging system to observe them, and we need to levitate them to keep them within the depth of focus of the objective.

The high resolution imaging system which we have used to characterize the

composite quantum droplets has been described in section 1.4. Moreover, we have developed a technique to image both spin states at high field, as described in chapter 2. This technique is crucial since in our steel science chamber we cannot switch off the magnetic fields to image at zero field fast enough so that the atomic losses and the modification of the droplets size do not smear out the features of the system.

To levitate the mixture we cannot use a magnetic field gradient due to the difference in the magnetic dipole moment between both spins. For homonuclear mixtures we do not have a differential gravitational sag, and it is enough to levitate the cloud with a single optical potential. In our case, we load the atoms on a single plane of a blue detuned optical lattice [29, 77]. This optical potential not only levitates the atoms against gravity but also provides a small anticonfinement in the transverse plane.

The last important challenge to observe the self-bound quantum droplets is to distinguish them from other types of self-bound states, such as bright solitons. In the presence of a trap, bright solitons can be stabilized due to the interplay between the repulsive quantum pressure and the residual mean field attraction. In this experiment, the anticonfinement produced by the blue detuned optical potential does not allow us to stabilize bright solitons [48, 141]. Therefore, the observation of a self-bound state in this trapping potential is a clear signature of the existence of a beyond mean field stabilization mechanism. In other trapping geometries, like in quasi-1D, both bright solitons and quantum droplets can be stabilized. In chapter 4 we show a detailed experimental study on the interplay between these two self-bound states.

In the following section we show our results on the experimental realization of composite quantum liquid droplets in a quasi-2D geometry.
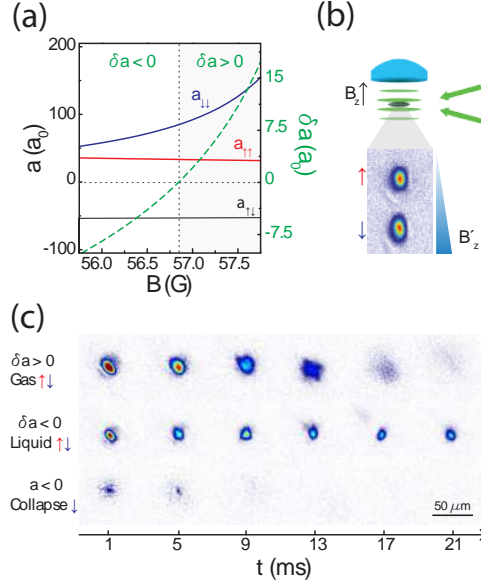
Figure 3.5: Observation of quantum droplets. Figures taken from [29]. (a) Scattering lengths a (solid lines) and parameter $\delta a = a_{\uparrow\downarrow} + \sqrt{a_{\uparrow\uparrow} a_{\downarrow\downarrow}}$ (dashed line) vs. magnetic field B for a ^{39}K mixture in states $|\uparrow\rangle \equiv |F = 1, m_F = -1\rangle$ and $|\downarrow\rangle \equiv |F = 1, m_F = 0\rangle$. The condition $\delta a = 0$ (dashed vertical line) separates the repulsive ($\delta a > 0$, grey area) and attractive ($\delta a < 0$, white area) regimes. (b) Schematic view of the experiment. Atoms are prepared in a plane of a blue-detuned optical lattice created by two beams intersecting at a small angle, and imaged *in situ* with a high numerical aperture objective ($\leq 0.97(4)$ μm measured resolution, 1/e Gaussian width). The spin composition of the system is verified independently *via* Stern-Gerlach separation by a magnetic field gradient during time-of-flight expansion. (c) Typical *in situ* images taken at time t after removal of the radial confinement but in the presence of the lattice potential. Top row: expansion of a gaseous mixture ($B = 56.935(9)$G and $\delta a = 1.2(1) a_0 > 0$). Central row: formation of a self-bound mixture droplet ($B = 56.574(9)$ G and $\delta a = -3.2(1) a_0 < 0$). Bottom row: collapse of a single-component $|\downarrow\rangle$ attractive condensate ($B = 42.281(9)$G and $a = -2.06(2) a_0 < 0$). In our geometry, quantum pressure cannot stabilize bright solitons. Therefore, the existence of self-bound liquid droplets is a direct manifestation of beyond mean-field effects.

3.5 Experimental realization of quantum liquid droplets in quasi-2D

In this work, we have observed for the first time ultracold atomic droplets in a mixture of two Bose-Einstein condensates with competing contact interactions. We demonstrated the self-bound character of mixture droplets and directly measured their ultra-low densities and micrometer-scaled sizes. Moreover, by comparison to a single-component condensate with only contact interactions, we confirmed that their stability stems from quantum fluctuations. Similarly to the dipolar case [33], we observed that for small atom numbers kinetic energy (which scales with density as $\mathcal{E}_K \propto n$) dissociates the droplets and drives a liquid-to-gas transition. We mapped out the corresponding phase transition line as a function of interaction strength and compared it to the theoretical model described in section 3.2. Our measurements have demonstrated that dipolar and mixture droplets share fundamental features despite the different nature of the underlying interactions. Given the simpler microscopic description of mixture droplets, which includes only well-known contact interactions, they constitute ideal systems to benchmark the validity of complex quantum many-body theories beyond the mean-field approximation.

3.5.1 Methods

We perform experiments with two ^{39}K Bose-Einstein condensates in internal states $|\uparrow\rangle \equiv |m_F = -1\rangle$ and $|\downarrow\rangle \equiv |m_F = 0\rangle$ of the $F = 1$ hyperfine manifold. An external magnetic field allows us to control the interactions parameterized by the intra- and inter-state scattering lengths $a_{\uparrow\uparrow}$, $a_{\downarrow\downarrow}$ and $a_{\uparrow\downarrow}$ (see Fig. 3.5 (a)). These have been computed by A. Simoni according to the model of ref. [142]. The residual mean-field interaction is proportional to $\delta a = a_{\uparrow\downarrow} + \sqrt{a_{\uparrow\uparrow}a_{\downarrow\downarrow}}$. The condition $\delta a = 0$ separates the repulsive ($\delta a > 0$) and attractive ($\delta a < 0$) regimes.

The experiment starts with a pure condensate of $8.0(8) \times 10^4$ atoms in state $|\uparrow\rangle$ which we produced with the sequence described in chapter 1. Subsequently, we load the atoms into a single plane of a vertical blue-detuned optical lattice of

10.7μm spacing (see inset of Fig. 3.5 (b)). It is created by the interference of two 532 nm laser beams crossing at 1.43°. The fraction of atoms loaded into other planes remains below 10%, as verified using a matter-wave focusing technique [96]. The lattice yields a trapping frequency $\omega_z/2\pi = 635(5)$ Hz along the vertical direction and a weak anti-confinement in the horizontal plane (estimated to be ~ 1 Hz in the most anti-confined direction). The vertical confinement is such that the atoms are levitated against gravity. The vertical harmonic oscillator length $a_{\mathrm{ho}} = 0.639(3)$ μm is smaller than the typical droplet sizes along the z direction and the density healing length. Thus, the system is in quasi-2D with respect to the density degrees of freedom. However, the vertical harmonic oscillator length exceeds the characteristic length of the spin Bogoliubov excitation branch ξ_s by typically a factor of 3 and we can consider the LHY correction in the 3D regime. The horizontal anti-confinement is used to avoid the stabilization of bright solitons in this trapping geometry. During the droplet preparation sequence the atoms are radially confined by a red-detuned 1064 nm optical dipole trap. The value of the radial trapping frequency is adjusted for each magnetic field in order to avoid exciting collective modes of the droplets.

In order to prepare a balanced mixture of the two states, we apply a radio-frequency pulse at $B \approx 57.3$ G, which lies in the miscible regime ($\delta a \approx 7\,a_0$, where a_0 denotes the Bohr radius) [54]. For all measurements, we verify independently the spin composition of the mixture *via* Stern-Gerlach separation during time-of-flight expansion (see Fig. 3.5 (b)). The same pulse is used to calibrate the magnetic field with an uncertainty of 9 mG, given by the linewidth of the rf transition. The result is corrected for the mean-field interaction shift by comparison to a thermal gas. Subsequently, we perform an 8 ms linear ramp to $B \approx 56.9$ G, corresponding to $\delta a \approx 0.8\,a_0$. Finally, we ramp down the magnetic field at a constant rate of 59 G/s and enter the attractive regime $\delta a < 0$. We then switch-off the vertical red-detuned optical dipole trap while keeping the lattice confinement, allowing the atoms to evolve freely in the horizontal plane. The integrated atomic density is imaged *in situ* at different evolution times. We use the high numerical aperture objective ($< 1\,\mu$m resolution, $1/e$ Gaussian width[1])

---

[1]Notice that this resolution does not correspond to the Rayleigh criterion. However, all the sizes described on the chapter correspond to the 1/e Gaussian width. For this reason, we have fitted the point spread function with a Gaussian to define a resolution which can be directly

presented in chapter 1 along the vertical direction and a phase-contrast polar-
ization scheme [102] which detects both states with almost equal sensitivity. We
image the cloud at high field with a 3 μs pulse at a detuning such that the Fara-
day coefficients for both components are very similar $c_{F\uparrow} = -1.1 \cdot 10^{-15} \text{rad} \cdot \text{m}^2$
and $c_{F\downarrow} = -1.4 \cdot 10^{-15} \text{rad} \cdot \text{m}^2$ (for more details see chapter 2). In this way, we
avoid any expansion and atomic losses of the cloud due to a switch off sequence
of the magnetic field. Moreover, the imaging pulses are so short that the atomic
blurring due to photon scattering is negligible.

3.5.2 Proof of principle observation: Beyond mean field stabilization of quantum droplets

Typical images of the mixture time evolution in the repulsive and attractive
regimes are displayed in Fig. 3.5 (c). For $\delta a = 1.2(1) a_0 > 0$ (top row) [2],
the cloud expands progressively in the plane, as expected for a repulsive Bose
gas in the absence of radial confinement. In contrast, in the attractive regime
$\delta a = -3.2(1) a_0 < 0$ (central row), the dynamics of the system are remarkably
different and the atoms reorganize in an isotropic self-bound liquid droplet. Its
typical size remains constant for evolution times up to 25 ms. We perform an
analogous experiment with a single-component attractive condensate. For the
single-component experiments, we instead transfer all the atoms to $|\downarrow\rangle$ using a
Landau-Zener sweep centered around $B \approx 46.85$ G. The magnetic field is sub-
sequently ramped down in 10 ms to its final value. Below $B = 44.19$ G, the
scattering length $a_{\downarrow\downarrow}$ becomes negative and gives access to a weakly attractive
single-component Bose gas. At a scattering length $a = -2.06(2) a_0 < 0$ the
system collapses (bottom row).

In our experimental geometry, quantum pressure can never stabilize bright
solitons due to the presence of weak anti-confinement in the horizontal plane.
At the mean-field level, the two-component attractive case has a description
equivalent to the single-component one, provided that the scattering length a is

---

compared to the results of this chapter. The relation between both gives a factor of 2.9.

[2]Here and in the following, error bars for the scattering lengths correspond to the 9 mG
experimental uncertainty of the magnetic field and do not take into account the systematic
uncertainties of the scattering length model.

replaced by $\sim \delta a/2$ and the density ratio between the two components is fixed to $n_\uparrow/n_\downarrow = \sqrt{a_{\downarrow\downarrow}/a_{\uparrow\uparrow}}$. However, the role of the first beyond mean-field correction is very different in the two systems, explaining their very different behavior. In the single-component case, the Lee-Huang-Yang energy depends on a and in the weakly interacting regime constitutes a negligible correction to the mean-field term. Therefore, its contribution is most easily revealed in strongly interacting systems [143]. In contrast, in the mixture the mean-field and Lee-Huang-Yang energy densities scale as $\mathcal{E}_{\mathrm{MF}} \propto \delta a \, n^2$ and $\mathcal{E}_{\mathrm{LHY}} \propto (\sqrt{a_{\uparrow\uparrow}a_{\downarrow\downarrow}} \, n)^{5/2}$, respectively as introduced in section 3.2. Since $\sqrt{a_{\uparrow\uparrow}a_{\downarrow\downarrow}} \gg |\delta a|$, for typical experimental parameters they balance at accessible atomic densities and stabilize liquid droplets [28]. Therefore, the existence of liquid droplets is a striking manifestation of beyond mean-field effects in the weakly interacting regime.

To further characterize the mixture, we perform a quantitative analysis of the images fitting the integrated atomic density profiles with a two-dimensional Gaussian. We extract the atomic density profiles from the raw images taking into account the intensity of the probe beam and the transfer function of the polarizer as explained in chapter 2. In order to obtain the atom number N and radial size σ_r of the system[3], we fit the images with a two-dimensional Gaussian $N\mathrm{e}^{-x^2/\sigma_x^2-y^2/\sigma_y^2}/(\pi\sigma_x\sigma_y)$. We find $\sigma_x/\sigma_y \approx 1$ for all our measurements and therefore we define $\sigma_r = \sqrt{\sigma_x\sigma_y}$. As depicted in Fig. 3.6, this fitting function is chosen to simplify the comparison to the theoretical model. Since we do not observe the size along the vertical direction σ_z, we assume it to be identical to the corresponding harmonic oscillator length $a_{\mathrm{ho}} = \sqrt{\hbar/(m\omega_z)}$. This assumption is supported by our theoretical model.

3.5.3 Liquid to gas phase transition and phase diagram

In Fig. 3.7 (a) (top and central panel) we show the time evolution of N and σ_r measured for the interaction parameters of Fig. 3.7 (c). For $\delta a > 0$ (red circles) the gas quickly expands while its atom number does not vary. Instead, for $\delta a < 0$ (blue circles) the system is in the liquid regime and the radial size of the droplet remains constant at $\sigma_r \approx 6\,\mu\mathrm{m}$. Initially its atom number is $N = 24.5(7) \times 10^3$,

---

[3]We have verified that the zeroth and second moments of raw images give compatible results for the atom number and radial size, respectively.
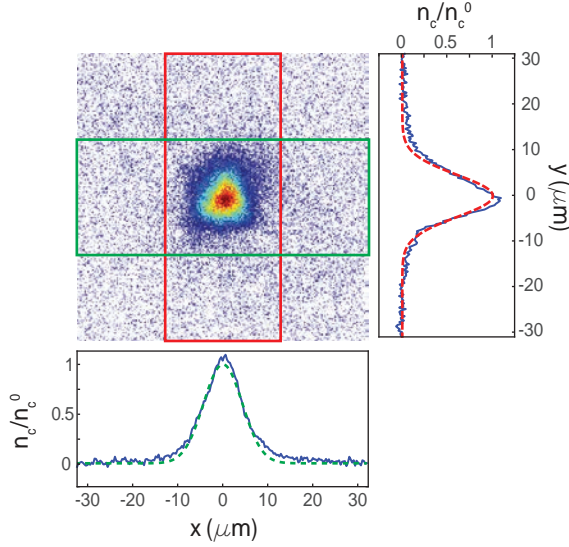
Figure 3.6: Figures taken from [29]. Experimental density profiles. *In situ* column density profile of a quantum droplet integrated along the imaging direction z, for $N = 1.7(4) \times 10^4$ and $B = 56.574(9)$ G ($\delta a = -3.2(1) \, a_0$). The right and bottom panels depict the corresponding doubly-integrated density profiles $\bar{n}$ (solid lines), together with the two-dimensional Gaussian fit used to analyze the data (dashed lines). Both are normalized to the peak value $\bar{n}_0$.

corresponding to a peak density of $n_0 = 1.97(8) \times 10^{14}$ atoms/cm^3. We attribute the subsequent decay of the droplet atom number shown in the top panel of Fig. 3.7 (a) to three-body recombination. The observed timescale is compatible with the measured density and effective three-body loss rate $K_3^{\mathrm{eff}} = 7.5 \times 10^{-28}$cm^6/s (for more details see ref. [65]). By directly measuring the density of our droplets we confirm that they are more than 8 orders of magnitude more dilute than liquid helium and remain very weakly interacting. Indeed, the interaction parameters of each component are extremely small ($n_\uparrow a_{\uparrow\uparrow}^3$, $n_\downarrow a_{\downarrow\downarrow}^3$, $\sqrt{n_\uparrow n_\downarrow} a_{\uparrow\downarrow}^3 \sim 10^{-5}$).

A closer view of the droplet size is displayed in the bottom panel of Fig. 3.7 (a). At $t \sim 25$ ms, σ_r starts to increase and the system behaves like the $\delta a > 0$ gas. Following refs. [28, 33, 49, 124], we attribute the dissociation of the droplet to the effect of quantum pressure, which acts as a repulsive force.
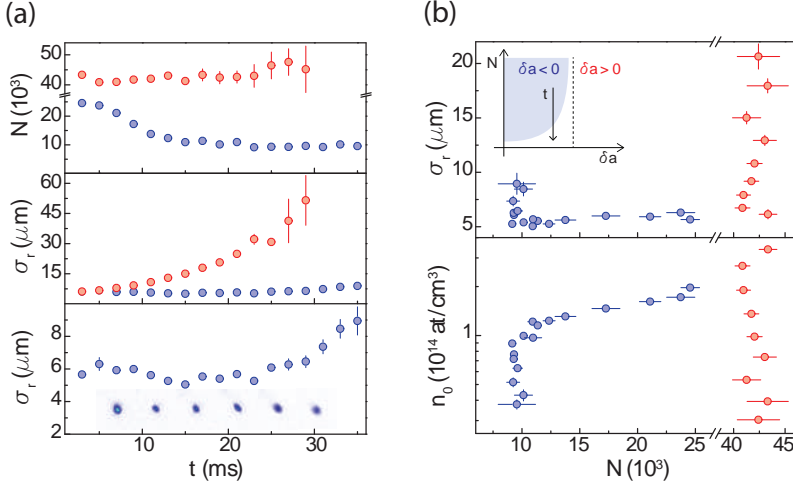
Figure 3.7: Liquid-to-gas transition. Figures taken from [29]. (a) Atom number N and radial size σ_r of the mixture for different evolution times t. The measurements are taken in the repulsive ($\delta a = 1.2(1)\,a_0 > 0$, red circles) and attractive ($\delta a = -3.2(1)\,a_0$, blue circles) regimes. Top panel: while for $\delta a > 0$ the atom number in the gas remains constant, for $\delta a < 0$ it decreases on a timescale compatible with three-body recombination. Central panel: the radial size of the droplet remains constant at $\sigma_r \approx 6\,\mu$m, demonstrating its self-bound nature. In contrast, the size of the gas increases continuously with time. Bottom panel: closer view of σ_r for $\delta a < 0$. For $t > 25$ ms the droplet dissociates and a liquid-to-gas transition takes place. The inset displays images corresponding to $t = 25 - 35$ ms. (b) Radial size σ_r (top panel) and peak density n_0 (bottom panel) vs. N. For $\delta a < 0$ and large atom number both remain approximately constant, as expected for a liquid. For a critical atom number we observe that σ_r diverges and n_0 drops suddenly, signalling the liquid-to-gas transition. In the gas phase, the $\delta a < 0$ system behaves as the $\delta a > 0$ one. Inset (top panel): sketch of the phase diagram. In the liquid phase (blue region), observing the mixture at variable evolution times gives access to different values of N (black arrow). Error bars represent the standard deviation of 10 independent measurements. If not displayed, error bars are smaller than the size of the symbol. Additionally, N has a calibration uncertainty of 25% .

As the atom number decreases, the relative weight between kinetic ($\mathcal{E}_K$) and interaction energies ($\mathcal{E}_{MF}$, $\mathcal{E}_{LHY}$) changes, for each energy term scales differently with N: $\mathcal{E}_K \propto N$, $\mathcal{E}_{MF} \propto N^2$ and $\mathcal{E}_{LHY} \propto N^{5/2}$. Below a critical atom number, kinetic effects become sufficiently strong to drive a liquid-to-gas transition. To support this scenario, Fig. 3.7 (a) depicts the radial size and atomic density as a function of atom number. For $\delta a < 0$ (blue circles) we observe that both size (top panel) and density (bottom panel) remain constant at large N. For decreasing atom number, we observe a point where the size diverges and the density drops abruptly. This indicates a liquid-to-gas transition, which takes place at the critical atom number N_c. Below this value, the attractive gas is still stabilized by quantum fluctuations but expands due to kinetic effects, similarly to the repulsive mixture ($\delta a > 0$, red circles).

The liquid-to-gas transition is also expected to depend on δa, as sketched in the inset of Fig. 3.7 (b) (top panel). We explore the phase diagram by tuning the interaction strengths with magnetic field (see Fig. 3.5 (a)). Fig. 3.8(a) displays the measured size as a function of the atom number for magnetic fields corresponding to δa between $-5.5(1)\, a_0$ and $-2.4(1)\, a_0$. The critical number N_c shows a strong dependence on the magnetic field. The top panel of Fig. 3.8 (b) presents our experimental determination of the phase transition line. We observe that N_c increases when the attraction decreases, confirming that weakly bound droplets are more susceptible to kinetic effects and require a larger atom number to remain self-bound. Fig. 3.8 (a) also shows the droplet size as a function of atom number and magnetic field. In the bottom panel of Fig. 3.8 (b) we display the measurements obtained at a fixed atom number $N = 1.5(1) \times 10^4$, always larger than N_c for our interaction regime. As expected, the droplet size decreases as the attraction increases.

We theoretically describe the system using the zero-temperature model presented in equation (3.2.1) of section 3.2. It is based on an extended Gross-Pitaevskii equation which includes both the vertical harmonic confinement and an additional repulsive Lee-Huang-Yang term. The latter is obtained assuming the Bogoliubov spectrum of a three-dimensional homogeneous mixture. At the mean-field level equation (3.2.1) is equivalent to a single-component Gross-
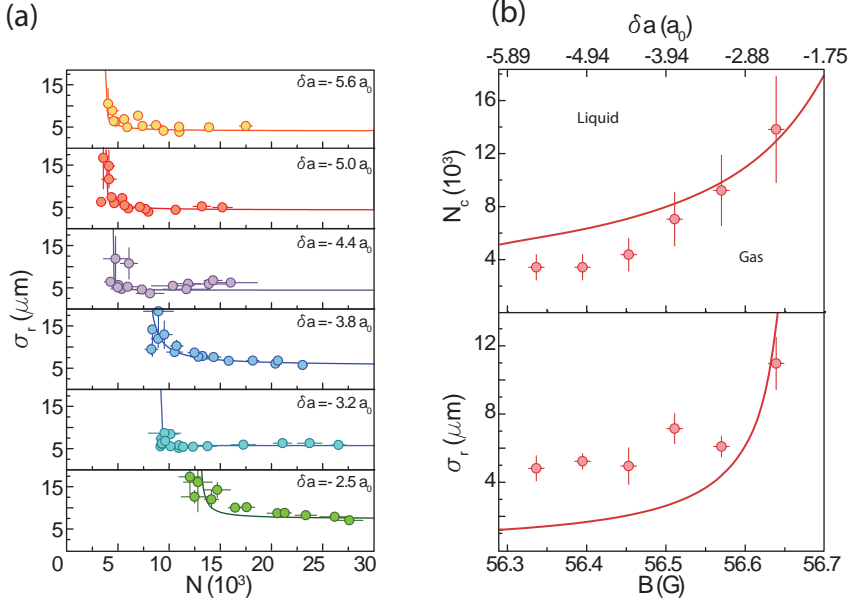
Figure 3.8: Liquid-to-gas phase diagram. Figures taken from [29]. (a) Radial size of the mixture σ_r as a function of atom number N for different magnetic fields B, from strong to weak attraction (top to bottom). The critical atom number N_c increases as attraction decreases. Solid lines display the phenomenological fit $\sigma_r(N) = \sigma_0 + A/(N - N_c)$ used to locate the liquid-to-gas phase transition. We have verified that using a different fitting function leads to changes in N_c well below the atom number calibration error. Therefore, the error bars in Fig. 3B correspond to the uncertainty of N (25%). (b) N_c (top panel) and σ_r for fixed $N = 1.5(1) \times 10^4$ (bottom panel) as a function of B. The upper horizontal axis shows the corresponding values of δa. Solid lines are the predictions of an extended Gross-Pitaevskii model without fitting parameters. Error bars for σ_r correspond to the standard deviation of 10 independent measurements. If not displayed, error bars are smaller than the size of the symbol. Error bars for B and N show the systematic uncertainty of the corresponding calibrations.

Pitaevskii equation provided one makes the replacement:

$$\delta a \to a(1 + \sqrt{a_{\uparrow\uparrow}a_{\downarrow\downarrow}})^2/2\sqrt{a_{\uparrow\uparrow}a_{\downarrow\downarrow}} \qquad (3.5.1)$$

Additionally, it includes the beyond mean-field term – negligible for a single-component condensate – which stabilizes the mixture against collapse and is responsible for the formation of quantum droplets.

We compute the ground state of the system by solving equation (3.2.1) numerically using the three-dimensional MATLAB toolbox of ref. [144]. These calculations were performed by B. Naylor. In this case we only consider the vertical confinement[4] $m\omega_z^2 z^2/2$. Even for the densest droplets realized in the experiment, we find that their density profile is well approximated by a Gaussian. Indeed, for the atom numbers and magnetic fields considered in the experiment, the bulk density of the liquid is not reached and the droplet size is comparable to the surface thickness [28]. We compare the numerical results to the variational minimization presented in section 3.2, where we use a Gaussian ansatz for the spatial mode of the two components determined by the parameters $\sigma_r = \sigma_x = \sigma_y$ and σ_z. As depicted in Fig. 3.9, we find excellent agreement between the two approaches, with deviations that remain well below the experimental error bars for the complete parameter range explored in the measurements. We use the variational results to compare the experimental data with the theory for simplicity.

In Fig. 3.8 (b) we compare the experimental results to the predicted critical atom number and droplet size (solid lines). We find qualitative agreement for the complete magnetic field range with no adjustable parameters. In the weakly attractive regime the agreement is even quantitative, similarly to the dipolar Erbium experiments of ref. [34]. In contrast, when increasing the effective attraction, the droplets are more dilute than expected. In particular, their size exceeds the theoretical predictions by up to a factor of three. This is almost one order of magnitude larger than our imaging resolution, excluding finite-resolution effects. Furthermore, the critical atom number is a factor of two smaller than the theoretical value. Interestingly, a similar discrepancy was reported for dipo-

---

[4]We have verified that including the residual anti-confinement of the optical lattice does not modify appreciably the theoretical predictions.
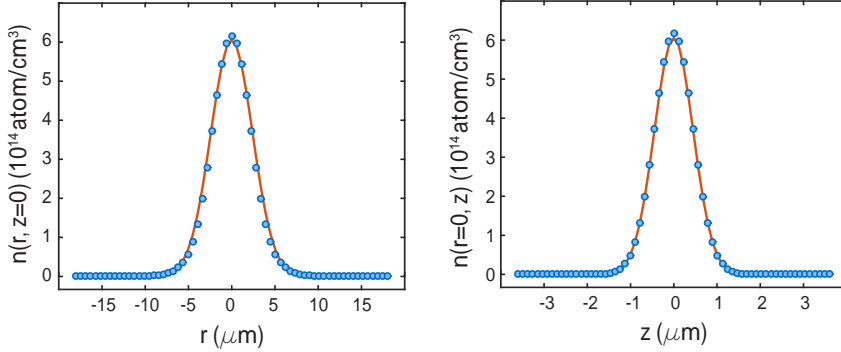
Figure 3.9: Theoretical density profiles. Figures taken from [29]. Density profiles predicted by the extended Gross-Pitaevskii model along the radial (left panel) and vertical (right panel) directions, for $N = 25000$ and $B = 56.57$ G ($\delta a = -3.20 \, a_0$). Blue circles: full numerical solution. Red lines: variational calculation with a Gaussian ansatz. The excellent agreement between both, even for the densest droplets realized in the experiment, justifies the Gaussian fitting function used to analyze the measured density profiles.

lar Dysprosium droplets, with a critical atom number one order of magnitude smaller than expected [33]. In this case, the deviation was attributed to an insufficient knowledge of the background scattering length. This explanation seems unlikely in the case of potassium, where excellent interaction potentials are available [72, 142, 145].

3.6   Conclusions

Other physical mechanisms might be responsible for the diluteness of the observed droplets. Although our system is three-dimensional, the confinement along the vertical direction might affect the Lee-Huang-Yang energy, modifying its density and interaction dependence or introducing finite-size effects. A description of quantum fluctuations in the dimensional crossover between two and three dimensions is challenging, and goes beyond the scope of this experimental work. Interestingly, the almost perfect cancellation of the mean-field energy could reveal other corrections besides the Lee-Huang-Yang term. Higher-order many-

body terms might play a role, as proposed in ref. [126] for single-component systems. Taking them into account analytically requires a good knowledge of the three-body interaction parameters of the mixture, which are non-universal and difficult to estimate in our interaction regime. Alternatively, our results could be compared to *ab initio* quantum Monte Carlo simulations, as recently performed in references [117, 118, 146]. Given the ultra-dilute character and simple microscopic description of our system, a direct comparison to different theoretical approaches could give new insights on yet unmeasured many-body effects.

3.7 Discussion on recent related work

During the completion of our work, we learned that similar experiments were performed by the LENS group [31]. These experiments where carried out by optically levitating the mixture with a linear optical gradient. The optical gradient was produced by modulating the position of an elliptical gaussian beam fast enough so that the atoms only saw an averaged potential. With this method, they were able to levitate the atoms with residual trapping frequencies $(\omega_x, \omega_y, \omega_z) \leqq 2\pi \times (2.2, 7, 16)$ Hz. Thus, their experiment was very close to that of free space droplets. Hence it became really interesting to corroborate the existence of quantum droplets in atomic mixtures in a regime where the system is in 3D both for the density and spin degrees of freedom.

Their results were obtained with the same ^{39}K mixture that we used. The preparation of quantum droplets was performed by starting with the BEC in state $|\uparrow\rangle$ at a magnetic field corresponding to $\delta a < 0$. Then they applied an rf pulse to produce a balanced mixture and observe the formation of droplets. Although this results in a quench of the interactions, by adjusting the trapping frequencies during the preparation sequence they were able to produce droplets with a residual breathing. Afterwards, they observed the droplets being self-bound for a few milliseconds in free space while losing atoms and the subsequent evaporation into a gas after reaching a critical atom number. The critical atom number, size and population ratio was measured and the experiments showed an agreement with the D. S. Petrov predictions [28].

In summary, both experiments represent a smoking gun of the liquid-to-gas

phase transition in Bose-Bose mixtures in two different scenarios. However, our experimental results do not show the same agreement with the theory presented in [28]. Several possibilities have been proposed for explaining the mismatch between the theory and our experiment.

3.7.1 Assessing the mismatch

Two main differences exist between our experiments. The trapping geometry and the slow/fast preparation of the droplet state. Concerning the trapping geometry, the trapping frequencies are such that the harmonic oscillator length is smaller than the density healing length, and we are in the quasi-2D regime with respect to the density degrees of freedom. Instead, the shortest interaction length scale, corresponding to the spin branch, is just 3 times the spin healing length, and thus we include the theoretical prediction of the LHY correction in 3D. However, the system might be close to the quasi-2D limit with respect to the spin degrees of freedom. In this hypothetical case, the beyond mean field correction needs to be properly computed. The calculation of this correction was out of the scope of our theoretical capabilities and we started discussing with L. Santos and D. Petrov to ask for advice. After the publication of our work, they performed a theoretical study of the dimensional crossover for the beyond mean field correction in Bose gases [147]. The calculations in the quasi-2D regime are only developed for a slab and preliminary estimations from our group indicate that this does not explain the mismatch between theory and experiment.

Another possibility could be that the validity of the local density approximation would be different for the trapping geometries of the different levitation schemes from references [29, 31]. In the very low atom number limit, the eGPE is not expected to be valid and finite size effects might come into play. To address this question full Monte Carlo simulations of our system are required. We got in contact with the UPC group led by J. Boronat, since they are experts on this topic. Their work led to the publication of related papers on liquid Bose-Bose mixtures [118, 146] studying the limits of the theory presented in ref. [28]. In these works they show that for high enough number of particles (on the order of 800 particles) and a negligible effective range (R) of the interaction potentials ($nR^3 \sim 10^{-5}$) the energy per particle vs. the gas parameter converges to the

theory presented in ref. [28]. Therefore our discrepancies cannot be explained by the presence of finite size effects. For the sake of completeness, and although we are very far from the high atom number regime, references [118, 146] show that for strong residual attraction $\delta a \ll 0$ the equilibrium density obtained from the numerical simulation of the full Hamiltonian deviates from the zero-temperature theory described in ref. [28].

Up to now we have only considered that the interactions between the particles in the BEC are well described by s-wave contact interactions [75]. Thus the only parameters that we use in the theory described in ref. [28] are the intra and inter-component scattering lengths. In this sense, the quantum liquid droplets would be universal. However, as pointed out initially in ref. [117], the equilibrium densities of quantum droplets differ for strong attraction depending on the effective range potential. In particular, the effective ranges in our mixture at B = 56.5 G are predicted to be $R_{\uparrow\uparrow} = 603a_0$, $R_{\downarrow\downarrow} = -1148a_0$ and $R_{\uparrow\downarrow} = 1024a_0$ by our model from ref. [75]. Thus, $nR^3 \sim 10^{-2}$ and the effective range could play an important role. To extend the validity of the model presented in ref. [28] beyond the universal regime, the energy per particle vs. gas parameter was computed for various intra and inter-state scattering length and effective ranges. From those results, an energy functional describing the Bose-Bose mixture in terms of scattering lengths and effective range was obtained in ref. [146]. Preliminary results from the J. Boronat group point at a reduction of the critical atom number for strong attraction which is enhanced by the vertical confinement [148]. This could explain the mismatch that we observe between theory and experiments. Indeed, very recent results comparing ^{162}Dy and ^{164}Dy dipolar droplets [119] were published to contrast the discrepancies observed between the scattering length measurements and the retrieved scattering lengths assuming that quantum droplets can be described by a zero-temperature model including quantum fluctuations. In the dipolar case the modeling of the interaction potentials is much more challenging and it is very complicated to predict the correct scattering lengths. A complete analysis of the problem is developed in reference [35], where they show that the zero-temperature model is not able to describe completely the physics of dipolar droplets.

Although the modification of the theoretical predictions due to the inclusion

of the effective range might explain the observation of our critical atom numbers, the measured sizes at $N = 15000$ cannot be accounted for with this effect. Preliminary estimations from the J. Boronat group point at a deviation of the density imbalance between the two components. Indeed, during the slow magnetic ramp to reach the droplet field we have three-body losses from the $|\downarrow\rangle$ state. Although a departure from the optimum density ratio would lead into evaporation of one of the components [117], this is a dynamical process (for more details see chapter 4). Therefore it could be that the observed droplets are not in the ground state.

In summary, the discrepancies observed in our experiment are still under investigation. The hypothesis of reduced dimensionality and finite size effects do not seem to match our results. Instead, the hypothesis of an enhanced effect of the finite interaction range for strong attraction under the presence of confinement, and the density ratio imbalance seem to be plausible. The study of this hypothesis remains as future work.

3.8   Outlook

Future research directions include the exploration of low-dimensional systems, where the enhanced quantum fluctuations make droplets ubiquitous [123]. In this direction, a study in the dimensional crossover [147] could connect the results from our group [29] and the LENS group [31] to the study of low dimensional systems. Preliminary preparation of the experimental setup to study lower dimensional systems is being carried out by A. Frölian, and will be described in her Ph.D. thesis . Moreover, a proper study of the droplet vs. spin composition could be performed by combining either scalar or polarization phase contrast imaging to measure the total atom number non-destructively and absorption imaging of one state to be able to extract the density ratio difference. A very interesting perspective concerns the study of the spectrum of collective modes of the droplets [28]. Its unconventional nature not only provides a sensitive testbed for quantum many-body theories, but should also give access to zero-temperature quantum objects [28] which are not present in the dipolar case [132]. However, for these studies longer-lived droplets would be required. This could be realized in our system by selecting different spin states, or in low dimensions (where the droplet

densities are predicted to be lower).

Chapter 4

Bright solitons and quantum droplets in a mixture of Bose-Einstein condensates

Abstract

Attractive Bose-Einstein condensates can host two types of macroscopic self-bound states: bright solitons and quantum droplets. Here, we investigate the connection between them with a Bose-Bose mixture confined in an optical waveguide. We show theoretically that, depending on atom number and interaction strength, solitons and droplets can be smoothly connected or remain distinct states coexisting only in a bi-stable region. We measure their spin composition, extract their density for a broad range of parameters and map out the boundary of the region separating solitons from droplets.

The work described in this chapter was explained in the thesis of my predecessor C. R. Cabrera [65] and was published in [30]. For this reason, in the following chapter of the thesis I will reproduce the main results without major modifications.

4.1 Introduction

Self-bound states are ubiquitous in nature, and appear in contexts as diverse as solitary waves in channels, optical solitons in non-linear media and liquid He droplets [44, 45, 114]. Their binding results from a balance between attractive forces, which tend to make the system collapse, and repulsive ones, which stabilize it to a finite size.

Bose-Einstein condensates (BECs) with attractive mean-field interactions constitute ideal model systems to explore in the same setting self-bound states stabilized by repulsive forces of different classes. In the previous chapter we introduced the physics of quantum droplets, self-bound states which are stabilized due to the balance between a residual mean field attraction and a repulsion stemming from quantum fluctuations. However, another type of self-bound states, bright solitons, were previously observed with attractively interacting single component BECs in a quasi-1D geometry with ^{7}Li [36–38], ^{85}Rb [39–41], ^{39}K atoms [42] and ^{133}Cs [43, 149]. They are stabilized due to the balance between attractive interactions and the repulsive quantum pressure. That is, by the dispersion along the unconfined direction. Whereas the stabilization of quantum droplets stems from a quantum many-body origin [28], the stabilization of bright solitons stems from a quantum pressure, which is a single particle effect.

Bright solitons and quantum droplets are *a priori* distinct states which exist in very different regimes. Solitons require the gas to remain effectively one-dimensional, which limits their maximal atom number [46–48]. In contrast, droplets are three-dimensional solutions that exist even in free space and require a minimum atom number to be stable [28, 29, 33, 34, 49, 50]. Until our work was published, quantum droplet experiments focused exclusively on systems where solitons were absent, enabling an unambiguous identification of the droplet state. Therefore, they could not provide any insights on their connections to solitons.

Using composite mixture with intra-component repulsion and inter-component attraction in the regime where $\delta a < 0$ we have an ideal setting to explore the similarities and differences between both self-bound states. In section 4.2.1 we will introduce the stabilization of single-component and composite bright solitons in the mean field approximation using a variational approach. Then, in section

4.2.2, we will explore the effects of the LHY correction on the phase diagram of attractive Bose-Bose mixtures in quasi-1D, putting emphasis on the similarities and differences between droplets and bright solitons. Afterwards in section 4.3 we will present our experimental study with spin mixtures of ^{39}K. Then, in section 4.4 we will conclude by summarizing the main experimental observations. In section 4.5, we discuss the recent results on droplet collisions [150] and heteronuclear self-bound states [151]. Finally, in section 4.6, we present future possible experiments.

4.2 Theoretical framework

To understand the interplay between the bright soliton and quantum droplet phases in a composite mixture in the following section we will start by introducing the physics of the stabilization of bright solitons in single component attractive BECs in the mean field regime. The same stabilization principle applies for a mixture of BECs with residual mean field attraction $\delta a < 0$ at the mean field level and composite bright solitons can be formed. Afterwards, in section 4.2.2, we take into account the LHY correction and describe the interplay between composite quantum droplets and bright solitons.

4.2.1 Bright solitons in the mean field regime

Solitons are localized self-bound solutions which can propagate through a nonlinear media without modifying their shape [44]. In Bose-Einstein condensates there exist mainly two types of solitons in quasi-1D: dark solitons and bright solitons. Whereas dark solitons exist in repulsive BECs and are characterized by a density dip and a sharp phase change [152, 153], bright solitons exist in attractive BECs and are characterized by a density maximum [37]. The stabilization of single component attractive BECs into bright solitons at the mean field level depends on the dimensionality of the problem. In 3D, as already explained, attractive condensates collapse. However in the quasi-1D regime, bright soliton solutions exist. A bright soliton is stabilized due to the balance between the attractive non-linearity and repulsive kinetic dispersion, also known as quantum
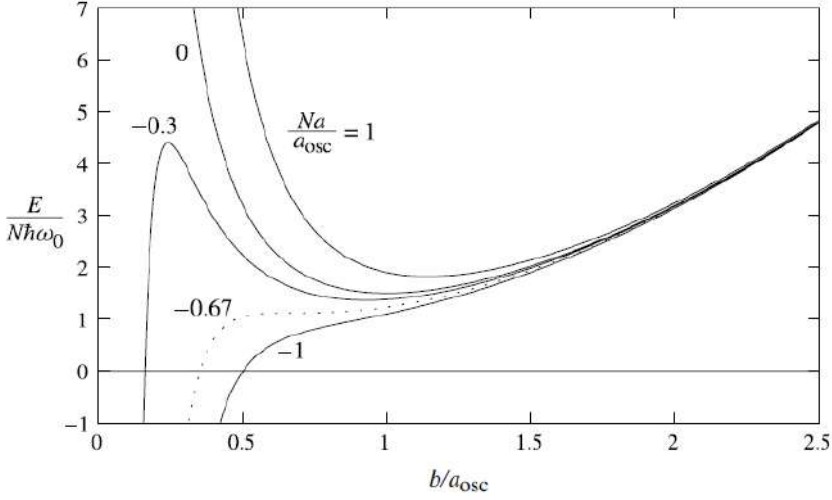
Figure 4.1: Image taken from reference [88]. Energy of a single component BEC in a trap vs. size computed using a gaussian variational ansatz for different Na/a_{ho}. Here b corresponds to the radial size r and a_{osc} corresponds to the harmonic oscillator a_{ho}. For positive and small Na/a_{ho} there is a stable minimum with a size very similar to the harmonic oscillator length. For very negative Na/a_{ho} the energy is minimized for zero size and thus the BEC would collapse. For small negative Na/a_{ho} there is a metastable minimum showing the existence of a bright soliton solution. The dashed line shows the extremal case where $Na/a_{\mathrm{ho}} = -0.67$ and the soliton solution disappears.

pressure. To be in the quasi-1D regime the chemical potential of the BEC in an optical waveguide needs to be smaller than the trapping frequency energy. This condition can be expressed in terms of length scales, so that if $N|a|/a_{\mathrm{ho}} < \eta_{\mathrm{c}}$ a bright soliton can be stabilized, where η_{c} is a numerical value of order 1.

We have solved the GPE for a single component BEC with attractive interactions using the Gaussian variational principle presented in section 3.2, considering $\sigma_x = \sigma_y = \sigma_z = \sigma_r$ as it was done in reference [88]. In figure 4.1 we plot the energy as a function of σ_r for different $N|a|/a_{\mathrm{ho}}$. As it can be observed, for attractive interactions, there exists a metastable minimum with the size of the harmonic oscillator length for small enough $N|a|/a_{\mathrm{ho}}$. For attractive interactions and $N|a|/a_{\mathrm{ho}} > 0.67$ the metastable minimum disappears and the BEC

collapses as it has been shown in references [120, 121, 154–156]. Similar results were obtained in references [157, 158] by solving the GPE numerically, obtaining $\eta_c = 0.57$.

The stabilization for a composite BEC with residual mean field attraction $\delta a < 0$ is essentially equivalent to the single component case. As introduced in section 3.2 the GPE equation for the two component BEC, excluding the LHY correction, can be simplified into an effective single component equation with the difference that we substitute

$$a \to \frac{2\delta a \sqrt{a_{\downarrow\downarrow}/a_{\uparrow\uparrow}}}{\left(1 + \sqrt{a_{\downarrow\downarrow}/a_{\uparrow\uparrow}}\right)^2}. \tag{4.2.1}$$

We have solved the effective single component GPE numerically in the two component case and have obtained the quasi-1D condition:

$$N \frac{2|\delta a| \sqrt{a_{\downarrow\downarrow}/a_{\uparrow\uparrow}}}{a_{\mathrm{ho}} \left(1 + \sqrt{a_{\downarrow\downarrow}/a_{\uparrow\uparrow}}\right)^2} < 0.6268. \tag{4.2.2}$$

The implication of this result is that for a certain δa, bright solitons cannot be stabilized above a critical atom number at the mean field level. However, this is not the case if we consider the LHY correction.

4.2.2 Bright solitons and quantum droplets

As already explained in the previous chapters, quantum droplets can be stabilized due to the interplay between the attractive mean field energy $\mathcal{E}_{\mathrm{MF}}$ and the repulsion induced by the LHY correction $\mathcal{E}_{\mathrm{LHY}}$. For very high atom numbers and/or very strong attraction the kinetic and potential energy terms can be neglected and droplets can be stabilized. On the other hand, for small enough atom numbers and/or very small attraction the LHY correction is very small and the attractive mean field energy $\mathcal{E}_{\mathrm{MF}}$ can be stabilized by the kinetic energy $\mathcal{E}_{\mathrm{K}}$ in a quasi-1D geometry, and composite bright solitons can be formed. But what happens in a quasi-1D geometry in the regime where all energy scales are relevant? And how do the different regimes connect between each other?

To address this questions we have numerically solved the eGPE equation (3.2.5) presented in section 3.2 for different atom numbers and interaction strengths below $\delta a < 0$. We have considered a cigar shaped trapping geometry with the trapping frequencies from the experiment and the scattering lengths corresponding to the ^{39}K spin mixture (for more details see section 4.3). In this situation the system is in 3D with respect to the spin degrees of freedom (as described in chapter 3) and in quasi-1D with respect to the density degrees of freedom. Note that although equation (3.2.2) bears strong similarities with the cubic-quintic non-linear Schrödinger equation employed in optics to describe high-order material non-linearities in the optical soliton community [45], the repulsive term has an unusual quartic dependence. This is the scaling corresponding to quantum fluctuations in three-dimensional condensates [122], which is the regime explored experimentally.

Ground state Phase diagram

To compute the ground state of the system we find numerically the stationary solutions of eq. (3.2.2) as in the previous chapter [144]. These calculations were performed by P. Cheiney and B. Naylor. For each δa we first solve the eGPE for $N = 1000$, using as initial guess for ϕ a three-dimensional Gaussian of size a_{ho}. We subsequently compute the solution for increasing values of N, choosing as initial guess the function ϕ determined in the previous step.

Fig. 4.2 depicts the peak density of the ground state n_0 as a function of the total atom number $N = N_\uparrow + N_\downarrow$ and δa (corresponding to a particular magnetic field B)[1]. For large attraction we find two distinct behaviors: a high-density solution ($n_0 \sim 10^{16}$ atoms/cm^3) for large N, and a low-density one ($n_0 \sim 10^{13}$ atoms/cm^3) for small N. In between, the gray region corresponds to a bi-stable regime where both solutions are possible. Its boundaries are signaled by a discontinuity of the density. This behavior disappears above a critical $\delta a < 0$ (which corresponds to the magnetic field $B_c \sim 55.85$ G for our experimental confinement). For smaller attraction, the system supports a single solution whose density increases progressively with N.

---

[1]For all parameters considered in 4.2, we find that the density profile of the system is well approximated by a Gaussian.
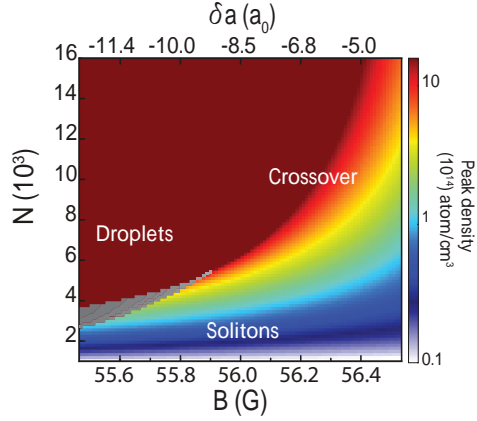
Figure 4.2: Figure taken from ref.[30]. Soliton-to-droplet density diagram. Ground state peak density as a function of atom number N and magnetic field B computed numerically from the effective single-component eGPE. Solitons and droplets are distinct solutions, which coexist in a bi-stable region (shaded area) and become smoothly connected in the crossover above $B_c \sim 55.8$ G.

In summary, for strong attraction the situation is analogous to a quantum ($T = 0$) first order liquid-to-gas phase transition: the bi-stable regime contains metastable regions surrounding a transition line, and for small attraction, above a critical δa a crossover region appears.

Energy landscape

To gain further insight on the phase diagram, we perform a variational analysis [159] in analogy to what we presented in section 3.2. These calculations were performed by P. Cheiney, C. R. Cabrera and L. Tarruell. In this case we have considered that the atoms are in a cigar shaped trap with a trapping frequency $\omega_y = \omega_z = \omega_r$ and we have neglected the trapping frequency along the axial direction. Hence, we use a gaussian ansatz with the parameters σ_x and $\sigma_y = \sigma_z = \sigma_r$. We have solved the problem for different atom numbers and interaction strengths below $\delta a < 0$ using the parameters corresponding to our experiments with a ^{39}K spin mixture (for more details see section 4.3).

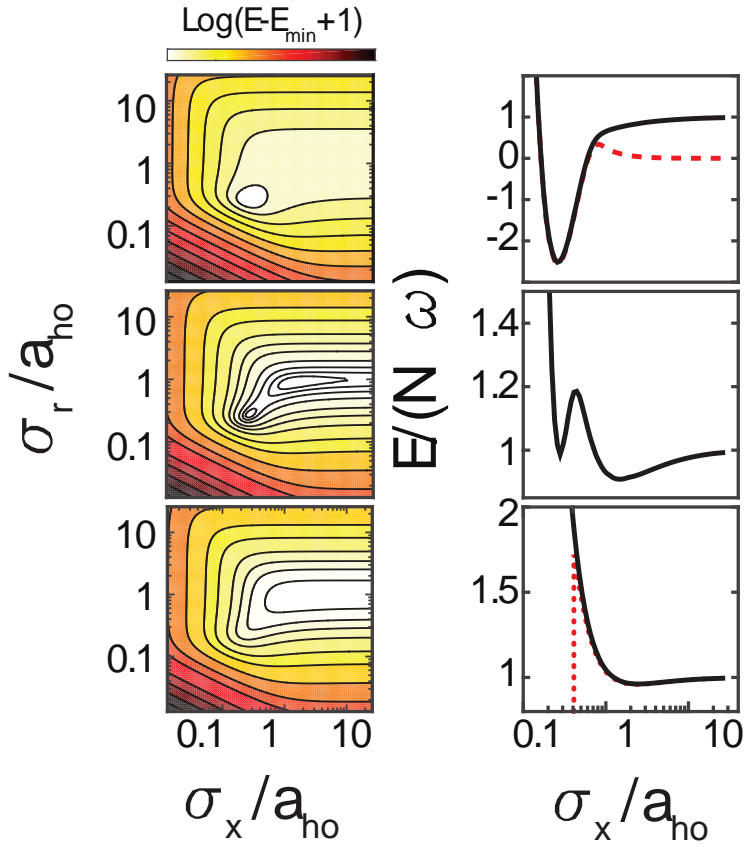Fig. 4.3 displays the energy landscapes obtained at a fixed δa below the

Figure 4.3: Figure taken from ref.[30]. Energy E of the Gaussian ansatz as a function of the radial σ_r and longitudinal σ_z sizes, for $B = 55.6$ G and $N = 9000$ (top, droplet), $N = 4000$ (center, bi-stable region) and $N = 2500$ (bottom, soliton). Right panel: one-dimensional cuts along σ_x, for σ_r minimizing E. All panels, solid lines: complete model; top panel, dashed line: no optical waveguide; bottom panel, dotted line: no quantum fluctuations.

critical point (corresponding to the magnetic field $B = 55.6$ G). For small values of N (bottom row), the energy has a single minimum corresponding to a dilute and elongated cloud: a composite bright soliton. Its size corresponds to the harmonic oscillator length a_{ho} and its energy per particle E are similar to those obtained in a mean-field treatment without quantum fluctuations (bottom right panel, red dotted line). In this case $E/N = \hbar\omega$ because of the two trapped degrees of freedom. For large values of N (top row) the minimum corresponds to a dense and isotropic solution with $\sigma_r \ll a_{\mathrm{ho}}$: a quantum liquid droplet. Its properties are not affected by the trapping potential, and it exists in its absence (top right panel, red dashed line). As it can be observed, the energy per particle vs. σ_x is only different by $\hbar\omega$ for large sizes between the trapped and free cases. Moreover, its stable solution has a negative energy, which confirms that it corresponds to a liquid-like solution[2]. In the bi-stable region (central row) both composite bright solitons and liquid droplets exist simultaneously. In this situation we can have either metastable droplets or solitons depending on the atom number.

Above the critical interaction strength a crossover takes place, and the energy landscape has a single minimum which evolves from soliton-like to droplet-like upon increasing the atom number. A related behavior, involving a bi-stable region and a crossover regime, has been studied in harmonically trapped dipolar gases [49, 50]. In this case, the low- and high-density solutions correspond to a BEC and a quantum droplet.

4.3   Experimental results

In our experiment we have explored a system that can host both bright solitons and quantum droplets: a mixture of two BECs in an optical waveguide. We observe that, as soon as the mean-field interactions become effectively attractive, self-bound states of well-defined spin composition appear. As we have shown theoretically, their nature evolves from soliton-like to droplet-like upon increase of the atom number. Depending on the interaction strength, both regimes can be smoothly connected, or remain distinct states that coexist only in a bi-stable region. We determine experimentally their density for a broad range of atom

---

[2]The zero of energy corresponds to an infinitely large cloud in the absence of a trap.

numbers and interaction strengths, and map out the boundary of the bi-stable region that separates bright solitons from quantum droplets.

4.3.1   Methods

We perform experiments with a mixture of ^{39}K BECs in Zeeman states $|\uparrow\rangle \equiv |m_F = -1\rangle$ and $|\downarrow\rangle \equiv |m_F = 0\rangle$ of the $F = 1$ hyperfine manifold in an optical waveguide. The optical waveguide is created by a red-detuned optical dipole trap of radial trapping frequency $\omega/2\pi = 109(1)$ Hz, see inset of Fig. 4.5(a). The system is imaged *in situ* with a spatial resolution of the order of the harmonic oscillator length $a_{\mathrm{ho}} = \sqrt{\hbar/m\omega} \simeq 1.5\,\mu$m, with $\hbar$ the reduced Planck constant and m the mass of ^{39}K. We exploit the phase-contrast polarization scheme to image both states with the same sensitivity as presented in chapters 1 and 3. The interactions are tuned *via* magnetic Feshbach resonances and parameterized by the intra- and inter-component scattering lengths $a_{\uparrow\uparrow}, a_{\downarrow\downarrow} > 0$ and $a_{\uparrow\downarrow} < 0$ [142]. Assuming that both components occupy the same spatial mode, the overall mean-field interaction is proportional to $\delta a = a_{\uparrow\downarrow} + \sqrt{a_{\uparrow\uparrow}a_{\downarrow\downarrow}}$, which is attractive for $B < 56.84$ G. Fig. 4.4 summarizes the values of $a_{\uparrow\downarrow}$, $a_{\uparrow\uparrow}$, $a_{\downarrow\downarrow}$ and δa predicted by the ^{39}K model interaction potentials of refs. [72, 142, 160]. We have verified that the model potentials of ref. [145] yield equivalent results [161].

The experiment starts with a pure BEC in state $|\uparrow\rangle$ confined in a crossed optical dipole trap of frequencies $\omega_{x,y,z}/2\pi = [49(1), 109(1), 119(1)]$ Hz. A radio-frequency (rf) pulse is used to prepare a controlled mixture of the two components[3]. The pulse is performed at $B \sim 57.2$ G, where $\delta a > 0$ and the system is in the miscible regime [54]. Subsequently the magnetic field is ramped down at a constant rate of 11.8 G/s while reducing the longitudinal confinement. The latter is removed in 5 ms at the final magnetic field, leaving the system unconfined along the x direction[4]. Finally, *in situ* images of the mixture are taken. The vast majority of the measurements performed in the $\delta a < 0$ regime correspond to self-bound states smaller or on the order of the imaging resolution.

---

[3]The system decoheres rapidly after the rf pulse, forming a two-component mixture.

[4]Although the waveguide beam also creates a longitudinal confinement of frequency $\omega_x/2\pi \lesssim$ 1 Hz along its propagation direction, it is insufficient to trap the atoms due to a residual tilt with respect to the horizontal axis.
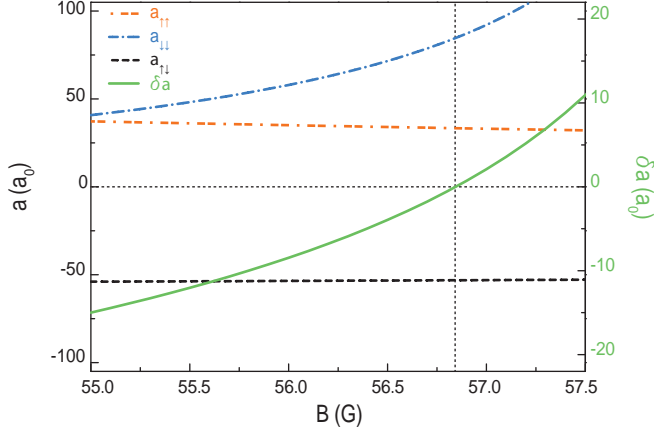
Figure 4.4: Figure taken from ref. [30]. Scattering lengths $a_{\uparrow\uparrow}$, $a_{\downarrow\downarrow}$, $a_{\uparrow\downarrow}$, and parameter $\delta a = a_{\uparrow\downarrow} + \sqrt{a_{\uparrow\uparrow}a_{\downarrow\downarrow}}$ (expressed in units of the Bohr radius a_0) as a function of magnetic field B for a ^{39}K mixture in states $|\uparrow\rangle \equiv |F = 1, m_F = -1\rangle$ and $|\downarrow\rangle \equiv |F = 1, m_F = 0\rangle$.

4.3.2   Observation of composite self-bound states

In Fig. 4.5 we fit the experimental density profiles with a two-dimensional Gaussian in order to extract their $1/e$ width σ_x, which could be strongly affected by lens aberrations. Thus, we do not use this quantity to characterize the system size quantitatively but only to indicate its self-bound character.

Fig. 4.5(b) shows typical *in situ* images of the time evolution of the mixture after release in the optical waveguide. Fig. 4.5(a) displays its longitudinal size σ_x as a function of magnetic field, for three different evolution times. In the repulsive regime ($\delta a > 0$) σ_x increases with δa, reflecting the increase of the released energy of the gas. In contrast, in the attractive regime ($\delta a < 0$) the absence of expansion indicates the existence of self-bound states. Experimentally, we only observe this behavior below $\delta a \sim -2a_0$, where a_0 denotes the Bohr radius. As in ref. [42], we attribute this effect to the initial confinement energy of the system.
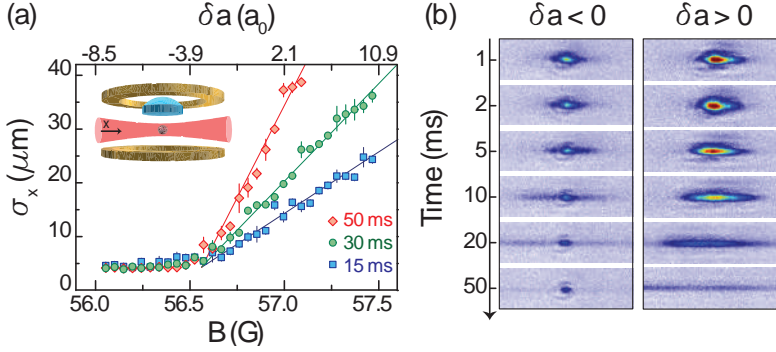
Figure 4.5: Figure taken from ref. [30]. Self-bound states. (a) Gaussian $1/e$ width σ_x of the mixture as a function of the magnetic field B (corresponding to different values of δa), for various evolution times after release in the optical waveguide (inset). For $B < 56.6$ G the system becomes self-bound and σ_x saturates to the imaging resolution (in this case the imaging was not properly aligned and the imaging resolution was worse than what is shown in chapters 1 and 3). Solid lines are linear fits to the data in the expanding regime and error bars denote the standard deviation of 10 independent measurements. (b) Typical *in situ* images for increasing evolution times, corresponding to a self-bound state (expanding gas) in the attractive (repulsive) regime with $\delta a < 0$ ($\delta a > 0$) and initial atom number $N \sim 7000$ ($N \sim 30000$).

4.3.3   Self-bound state composition

The observed self-bound states are intrinsically composite objects, involving both $|\uparrow\rangle$ and $|\downarrow\rangle$ atoms. To probe this aspect, we prepare mixtures of different compositions by varying the rf pulse time τ. Large population imbalances between the two states result in bi-modal density profiles in the *in situ* images, see left panel of Fig. 4.6(a). They consist of a self-bound state surrounded by a wider and expanding cloud of atoms of the excess component. We extract the fraction of self-bound atoms from bi-modal Gaussian fits to the density profiles. We find that the fraction of self-bound atoms is maximized for an optimal pulse time, see central panel.

To determine its spin composition we perform a complementary set of measurements, modifying the detection sequence. We dissociate the self-bound state by increasing the magnetic field to the repulsive regime ($B \sim 57.3$ G) in 1 ms,

similarly to ref. [32]. We then measure the atom number per spin component $N_\uparrow$ and $N_\downarrow$ *via* Stern-Gerlach separation during time-of-flight expansion, see right panel of Fig. 4.6.

We extract the optimal composition as a function of B by combining the *in situ* and time-of-flight measurements, see Fig. 4.6(b). The optimal pulse time τ_{op} is extracted from a lorentzian fit to the N_{SB}/N curve. Its error $\Delta\tau$ corresponds to the standard error of the mean extracted from the fit. To extract the optimal spin ratio from Fig. 4.6(b), after determining $N_\uparrow/N_\downarrow$ from time-of-flight images, we fit it in the vicinity of τ_{op} with a second order polynomial that we evaluate at τ_{op}. To extract the error of the ratio we evaluate the prediction bounds of the fit at $\tau_{\mathrm{op}} \pm \Delta\tau$ considering a confidence interval of σ.

As explained in the previous chapters the interaction energy of the system is minimized by maximizing the spatial overlap of the two components [28, 123]. The theoretical prediction assuming that both occupy the same spatial mode yields $N_\uparrow/N_\downarrow = \sqrt{a_{\downarrow\downarrow}/a_{\uparrow\uparrow}}$ (solid line), which is in fair agreement with the data.
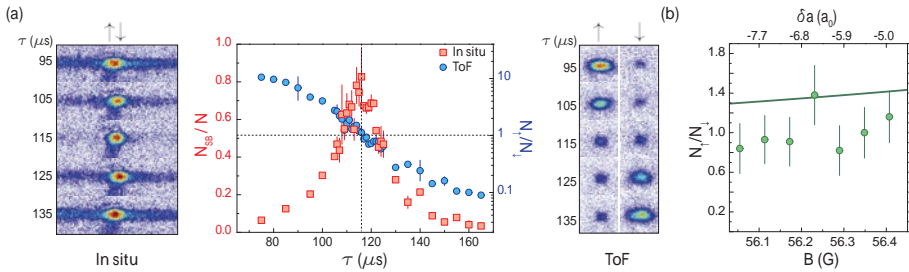

Figure 4.6: Spin composition. Figure taken from ref. [30]. (a) Left panel: *in situ* images of the mixture for various rf pulse times τ and $B = 56.35(1)$ G. Away from an optimal value the density profile is bi-modal, with a self-bound state surrounded by atoms of the excess component. Central panel: fraction of self-bound atoms N_{SB}/N (red squares) and spin composition $N_\uparrow/N_\downarrow$ (blue circles) as a function of τ. Error bars denote the standard deviation of 4 measurements. Right panel: corresponding time-of-flight (ToF) Stern-Gerlach analysis of the spin composition. (b) Optimal ratio $N_\uparrow/N_\downarrow$ as a function of magnetic field B. Error bars correspond to the confidence interval of the fit. The solid line depicts the theoretical prediction $N_\uparrow/N_\downarrow = \sqrt{a_{\downarrow\downarrow}/a_{\uparrow\uparrow}}$.
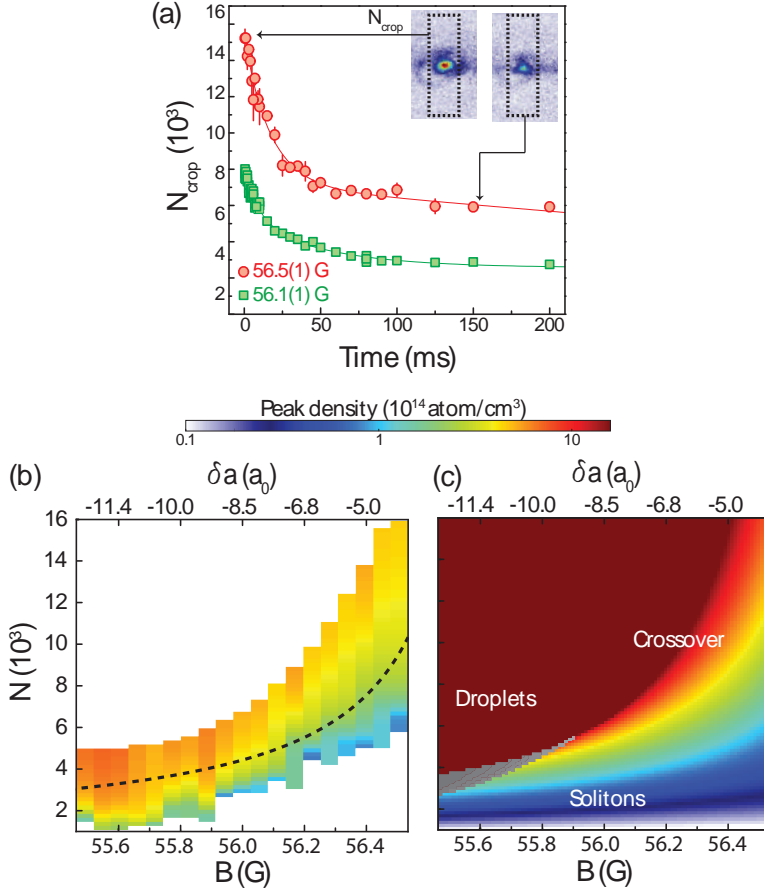
Figure 4.7: Soliton-to-droplet diagram. Figure taken from ref. [30]. (a) Evolution of the self-bound atom number N_{crop}, determined from the zeroth moment of the cropped region (insets), as a function of time t. Solid lines: empirical fit for extracting the decay rate. Error bars: standard deviation of 4 measurements. (c) Left panel: peak density extracted from the decay of the self-bound atom number, see (a). Self-bound states are stabilized by beyond mean-field effects well above the mean-field collapse threshold for composite bright solitons (dashed line). Right panel: ground state peak density vs. atom number N and magnetic field B computed numerically from the eGPE. Solitons and droplets are distinct solutions, which coexist in a bi-stable region (gray area) and become smoothly connected in the crossover above $B_c \sim 55.85$ G.

4.3.4 Experimental phase diagram in quasi-1D

To clarify the nature of the self-bound states and their relation to the well-known bright soliton and quantum droplet limits, we explore experimentally the phase diagram of the system preparing self-bound states at different interaction strengths, starting with high atom number. We record the atom number in the self-bound region as seen in the inset from Fig. 4.7(c). We determine quantitatively the atom number of the self-bound states from the *in situ* images by evaluating the zeroth moment of the images $N = M_{00} = \sum_{x,z} n_c(x,z)$, which is independent of optical aberrations [102]. In order to count only the self-bound atoms we crop the images around the maximal column density and extract N from this observation region. We have verified that increasing the crop size in the direction perpendicular to the waveguide does not modify the results. The longitudinal crop size needs to be adjusted more carefully to avoid counting excess atoms that are expanding in the waveguide. We fix its value by comparing the atom number extracted from *in situ* images with no excess component with time-of-flight measurements. We find that for all the data, possible errors in N associated to incorrect choices of the longitudinal crop size remain $< 10\%$, below the systematic error of the N calibration (25%).

We observe that the atom number decreases in time due to inelastic processes, see Fig. 4.7(c). For our experimental parameters these are completely dominated by three-body recombination in the $\downarrow\downarrow\downarrow$ channel. Similarly to recent experiments on dipolar ^{166}Er droplets [34], we extract the density of the self-bound state by measuring the decay of its atom number. The latter allows us to map out the density as a function of N from a single decay curve, overcoming the limits set by the imaging resolution[5].

Describing the decay of the self-bound states requires taking into account simultaneously two effects: (i) real loss of $|\downarrow\rangle$ atoms, since $K_{\downarrow\downarrow\downarrow}$ is much larger than the three other rates; (ii) expulsion (and subsequent expansion along the waveguide) of $|\uparrow\rangle$ atoms, in order to maintain the optimal spin composition of the self-bound state as expected from ref. [28, 117]. Modelling accurately the dynamics of these combined loss, expulsion and expansion processes goes beyond

---

[5]For all the measurements, the droplet and soliton sizes remain below (or are comparable to) the spatial resolution of the imaging system.

the scope of this work. Note that under these conditions it is not clear that the eGPE model (derived neglecting explicitly spin excitations [28]) or simple extensions of it remain valid. We instead simplify considerably the problem by assuming that $|\downarrow\rangle$ losses are instantaneously accompanied by the disappearance of $|\uparrow\rangle$ atoms required to maintain $N_\uparrow/N_\downarrow$ fixed in the self-bound state. The decay of the self-bound atom number is then given by the rate equation

$$\frac{\dot{N}}{N} = -K_3^{\mathrm{eff}} \langle n^2 \rangle,$$

where $\langle n^2 \rangle = \frac{1}{N} \int \mathrm{d}\mathbf{r}\, n^3$ and the effective three-body loss coefficient is $K_3^{\mathrm{eff}} = K_{\downarrow\downarrow\downarrow} \Big/ \left(1 + \sqrt{\frac{a_{\downarrow\downarrow}}{a_{\uparrow\uparrow}}}\right)^2$. In summary, the effective coefficient that we have considered in the model for the decay of the BEC is $K_3^{\mathrm{eff}} = 7.5 \times 10^{-28} \mathrm{cm}^6/\mathrm{s}$. More details on the measurement of this coefficient can be found in the thesis from C. R. Cabrera [65].

To extract $\dot{N}/N$ from the decay curves, we fit them with the empirical function

$$N(t) = N_\infty + p N_0 \mathrm{e}^{-(t-T_0)/T_1} + (1-p) N_0 \mathrm{e}^{-(t-T_0)/T_2},$$

where N_0, N_∞, T_0, T_1, T_2 and p are free parameters. We finally determine the peak density of the system from

$$n_0 = 3^{3/4} \sqrt{\langle n^2 \rangle} = 3^{3/4} \sqrt{\frac{1}{K_3^{\mathrm{eff}}} \left| \frac{\dot{N}}{N} \right|}.$$

Here, we have assumed a Gaussian density profile to relate the peak and average densities to facilitate the comparison to the theoretical model.

We have verified that the results obtained using a different experimental fitting function are well below the uncertainties introduced by the $K_{\downarrow\downarrow\downarrow}$ systematic error. In any case, we expect our determination of the density to be dominated by the simplifications of the decay model. Considering only the effect of $|\downarrow\rangle$ losses would reduce the determined densities by a factor of 2.

The right panel of Fig. 4.7(a) displays the determined peak densities as a function of atom number and magnetic field. Interestingly, a large fraction of

the measurements lies well above the mean-field bright soliton collapse threshold. At the theoretical optimum for $N_\uparrow/N_\downarrow$ it corresponds to the condition $N_c = 0.6268\, a_{\mathrm{ho}} \left(1 + \sqrt{a_{\downarrow\downarrow}/a_{\uparrow\uparrow}}\right)^2 / \left(2|\delta a|\sqrt{a_{\downarrow\downarrow}/a_{\uparrow\uparrow}}\right)$ (dashed line) as seen from equation (4.2.1). The absence of collapse in our measurements shows the existence of a stabilizing beyond mean-field mechanism.

In the deeply bound regime the measured peak densities agree only qualitatively with the eGPE predictions, see left and right panels of Fig. 4.7(a). The discrepancies might stem from two sources. First, we have considered that the spin composition of the system adjusts to $N_\uparrow/N_\downarrow = \sqrt{a_{\downarrow\downarrow}/a_{\uparrow\uparrow}}$ while we have seen experimentally that population imbalances are possible. Second, our decay model is very simplified and assumes that the $|\downarrow\rangle$ losses are immediately accompanied by the disappearance of $|\uparrow\rangle$ atoms when, in reality, these require a finite time to exit the observation region.

4.3.5 Soliton to droplet transition

In a last series of experiments we explore the phase diagram by approaching the bi-stability region from the soliton regime, see left inset of Fig. 4.8(a). We prepare the system in the crossover region at $B \sim 56.3$ G and hold it in the crossed optical dipole trap for a variable time (1 to 120 ms). Owing to three-body recombination, this results in atom numbers $N = 3000$ to 7000. We then remove the vertical trapping beam, rapidly decrease B to its final value at a rate of 93.8 G/s, and take an *in situ* image 3.5 ms after the end of the ramp. At the boundaries of the bi-stable region, the density of the system becomes discontinuous. Experimentally, we observe that the self-bound state cannot adjust to this abrupt change and fragments, see right panel.

To locate the fragmentation point, we record the atom number in the initially self-bound region and observe an abrupt drop at a critical magnetic field, see right panel from Fig. 4.8(a). We also determine quantitatively the atom number of the self-bound states by evaluating the zeroth moment of the images as done to explore the phase diagram. As shown in the left panel of Fig. 4.8(a) for two exemplary initial atom numbers N_i, the critical magnetic field depends on N_i. To extract the critical magnetic field for fragmentation B_c corresponding to the
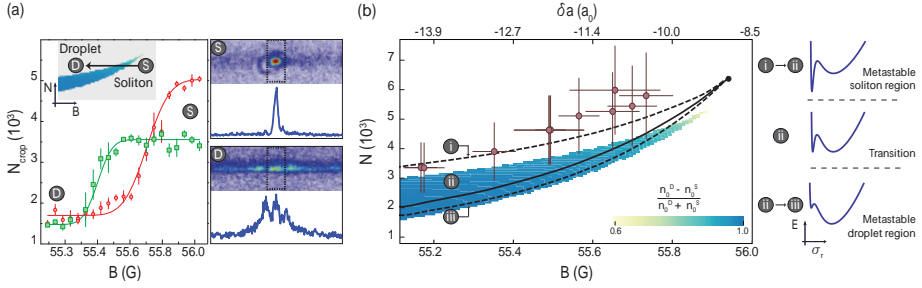
Figure 4.8: Figure taken from ref. [30]. Soliton-to-droplet transition. (a) Left panel: Atom number in the self-bound region N_{crop} as a function of magnetic field B when approaching the bi-stable region from the soliton regime, see inset. Top right panel: initial soliton image (S) and corresponding doubly-integrated density profile. Bottom right panel: fragmentation observed when entering the droplet regime (D). (b) Measured fragmentation point vs. N and B. Error bars: systematic error in N and magnetic field width of the fragmentation curve. Colored area: bi-stable region computed numerically from the eGPE. Lines: variational model, indicating the boundaries of the bi-stable region (dashed) and the transition line where solitons and droplets have identical energies E (solid). Insets: sketch of E vs. σ_z for the metastable soliton and droplet regions and the transition line.

initial atom number N_i we fit the experimental data shown in Fig. 4.8(a) with an error function

$$N_{\text{crop}} = \left(\frac{N_i - N_f}{2} \right) \text{erf} \left(-\frac{B - B_c}{\sqrt{2}\sigma} \right) + N_f,$$

where N_i, N_f, and B_c are free parameters. The horizontal error bars of the fragmentation points correspond to σ, and the vertical ones to the 25% systematic error on the atom number calibration. We summarize the position of the fragmentation point in the $N - B$ plane in Fig. 4.8(b).

We exploit the variational model to interpret our observations. According to it, although in the bi-stable region both solitons and droplets exist, their energies coincide only along a transition line (solid line). Above (below) it, solitons (droplets) become metastable, and only disappear at the upper (lower) boundary (dashed lines). The three situations are depicted in the right panel of Fig. 4.8(b). Experimentally, we prepare the mixture in a regime where only solitons

exist. Therefore, when entering the bi-stable region we expect it to follow preferentially the metastable soliton solution, with which it connects smoothly. At the upper boundary the metastable soliton disappears and only dense droplets are possible. Hence, the system is expected to fragment and form an excited state with identical total energy (a similar behavior is observed in trapped dipolar gases [32, 49, 124, 162]). Our experimental results support this hypothesis: within error bars, the fragmentation point agrees with the upper boundary of the bi-stable region predicted by the variational (solid line) and numerical eGPE (colored area) calculations without any fitting parameters. Moreover, since the atom number in each of the fragments is typically below the atom number required to form a droplet we expect that, after some relaxation dynamics, the system will evolve into a soliton train. Thus, although the fragmentation point corresponds to the onset of a modulation instability in the system and allows to map out the boundary of the bi-stable region, the final state is the result of complex non-linear dynamics and is not directly related to the ground state droplet solution.

4.4 Conclusions

In conclusion we have shown that an attractive mixture of BECs confined in an optical waveguide always hosts self-bound states, which correspond to composite bright solitons, quantum liquid droplets, or interpolate smoothly between both limits depending on the values of the atom number, interaction strength and confinement. We have characterized their spin composition and density, and mapped out the upper boundary of the bi-stable region separating solitons and droplets.

4.5 Discussion on related work

A way to distinguish between quantum droplets and bright solitons would be to produce two self-bound states and make them collide. This experiments have been performed using single-component bright solitons [43, 163], and they either cross each other or bounce depending on their relative phase. Using dipolar quantum droplets, collision experiments have been performed in a setting where

the collision axis is perpendicular to the dipole moment [128]. In this case the repulsive character of magnetic dipoles makes them bounce. Instead, theoretical studies of the collision between two composite quantum droplets in 1D [164], 2D [165] and 3D [166, 167] show that droplets might merge depending on the interactions, atom number and velocity.

In the LENS group, collisions between composite quantum droplets have been experimentally observed [150]. They prepare two independent BECs separated by a potential barrier to produce two independent droplets which can collide with different velocities after removing the barrier. For velocities below a critical value v_c, the quantum droplets merge, as expected also for classical liquid drops. Instead, if the kinetic energy is very high the surface tension cannot hold the two droplets together and they split. By performing experiments with different atom numbers and collision velocities they map out the merging and separation regimes. The experimental observations show that the critical velocity increases for small atom numbers and decreases for high atom numbers. Their experimental results are contrasted with a simple theoretical model in which critical velocity is defined by comparing the excess kinetic energy of the colliding droplets to the energy of the merged droplet using the liquid-drop model [168]. This model predicts that for high atom numbers, when the liquid-droplets become incompressible, the critical velocity should decrease. Therefore, their study shows a transition between the compressible and incompressible flat-top droplet regime. In this experiments, the phase between the colliding droplets is not equal in each run. Further experiments where the phase between droplets is controlled could show interesting insights on the differences with bright solitons.

Very recently, composite self-bound states in a quasi-1D geometry have been observed using heteronuclear mixtures of ^{41}K and ^{87}Rb for a critical $\delta g < 0$ [151]. Interestingly, the three body losses in this mixture are reduced due to their larger intra-species interaction strengths ($n_{\text{eq}} \sim \delta g^2/g^5$). Moreover, they are able to measure the ratio of atom numbers between both atomic species, finding excellent agreement with the theoretical $(g_{\text{Rb}}/g_{\text{K}})^{1/2}$. However, as we previously noticed in the experiments from chapter 3 [29] and explained in this chapter [30], kinetic energy plays an important role in the stabilization of attractive self-bound mixtures together with the LHY repulsion. For this reason, the

observation of a self-bound state in a quasi-1D geometry in an attractive mixture is not a "smoking-gun" of the existence of quantum droplets. Indeed, quantum droplets and bright solitons can either be smoothly connected by a crossover or be distinct states separated by a transition depending on their interaction strength and atom number. Therefore, in my opinion, further experimental evidence is needed to distinguish whether the observed heteronuclear self-bound states are bright solitons, quantum droplets or they are in a crossover between both.

4.6   Outlook

Future experimental directions include the study of metastability and hysteresis when crossing the soliton-to-droplet transition from different directions. This is experimentally challenging because of two reasons. First, because it is hard to prepare droplets with high density above the metastability region. And second, because the size of the metastability region for small attraction is on the order of our atom number uncertainty.

Other possible directions are the study of spin imbalanced systems offer the possibility to explore finite temperature effects [169] in a well controlled setting, exploiting the excess component as a thermal bath. Finally, a coherent coupling between the two components [170] is expected to yield effective three-body interactions [171] and provide control over the density dependence of the Lee-Huang-Yang term [172] in the weak coupling regime. However, it is experimentally challenging to achieve a magnetic field stability which allows us to observe beyond mean field effects in 3D in such setting. For this reason, in the following chapter, we study the modification of the interactions and the existence of bright solitons in a quasi-1D geometry with two coherently coupled BECs in the strong coupling limit.

Chapter 5

Coherently coupled interacting Bose-Einstein condensates

Abstract

In this chapter, we demonstrate fast control of the interatomic interactions in a Bose-Einstein condensate by coherently coupling two atomic states with intra- and inter-state scattering lengths of opposite signs. We measure the elastic and inelastic scattering properties of the system and find good agreement with a theoretical model describing the interactions between dressed states. In the attractive regime, we observe the formation of bright solitons formed by dressed-state atoms. Finally, we study the response of the system to an interaction quench from repulsive to attractive values, and observe how the resulting modulational instability develops into a bright soliton train.

Since the work explained in this chapter was detailed in reference [173], in the following chapter I will reproduce large fractions of the article without major modifications.

5.1 Introduction

The ability to control the interactions in a many-body system opens the door to study a wide range of phenomena. Primary examples are the study of the BEC to BCS crossover in Fermi gases [17], the study of the Fermi [174] and Bose polarons [19] and the observation of quantum droplets in a two-component incoherent mixture (see chapters 3 and 4). A key phenomena in the ultracold atom community is the existence of Feshbach resonances [16], which allow to tune the interactions from the weakly to the strongly interacting regime and from attractive to repulsive interactions.

A Feshbach resonance occurs when there is a coupling between the scattering continuum and a weakly bound molecular state [16]. The energy difference between both states can be tuned magnetically or optically (see reference [16] and references therein). So far, this has allowed the observation of magnetic [175] and optical Feshbach resonances [176, 177]. For magnetic Feshbach resonances the temporal control is limited technically by the inductance of the coils. Instead, for optical resonances, the main limitation comes from light-induced inelastic collisions. To overcome this limitations, magnetic Feshbach resonances can be shifted optically [178–182]. A periodical modulation of interactions was used to observe the stimulated emission of matter-wave jets in a Bose-Einstein condensate [183–185] and has been proposed as a tool to study Floquet driven systems [186, 187]. Moreover, while magnetic fields can modify the interactions globally, spatial control of interactions has been demonstrated with optical shifts of Feshbach resonances [177, 180, 182].

Another alternative to control the interactions is to use coherently coupled states. The phase diagram of an incoherent two-component BEC depends on the bare state intra and inter-component scattering of the mixture (see references [65, 88] and chapters 3 and 4). By coherently coupling both components we can modify the interaction strength between the dressed states and modify the phase diagram of the system. The resulting interaction strength of the dressed states is a linear combination of the bare state interaction strengths which depends on the parameters of the coupling field [51, 52]. Hence, by controlling the frequency and power of the coupling field, the interactions between the coherently coupled

states can be modified.

The experimental study of coherently coupled states in a Bose-Einstein condensate was pioneered by the Cornell group using [87]Rb [54, 170]. These studies were motivated by the analogy of such system with the Josephson effect in superconductors [188] and Helium [189, 190]. Later on, the Oberthaler group exploited the coherent coupling between two internal states of a [87]Rb Bose-Einstein condensate to explore the different dynamics and transition between the Rabi and Josephson regimes, where the coupling and interaction energies dominate respectively [53]. Further experiments focused on the study of the phase separation dynamics of a coherently coupled BEC (which were initially observed in a noncoherent mixture in reference [54]) due to the modification of the interactions in the presence of coherent coupling [55–57] and spin orbit coupling [58–60].

All the experiments performed so far with coherently coupled Bose-Einstein condensates have been performed with two components with repulsive and almost equal intra and inter-component scattering lengths. In this case, the interaction strength of the coherently coupled states are not strongly modified. Therefore, using [39]K mixtures with unequal interactions under the presence of coherent coupling offers a wide tunability of the interactions, going from the repulsive to the attractive regime. As introduced in previous chapters, during the last decade, attractive Bose-Einstein condensates have enabled the observation of single component bright solitons [36, 37], the study of bright soliton collisions [163], the realization of quantum droplets in incoherent mixtures [29, 31] and its interplay with bright solitons [30], the observation of quantum droplet collisions [150], and the characterization of the modulational instability that leads to the formation of bright soliton trains [191, 192].

In this chapter, we present the first direct measurements of the effective elastic and inelastic scattering lengths using BECs with unequal interactions in the strong coupling limit. This system allows us to explore the attractive regime and observe the existence of bright solitons formed by dressed atomic states. This technique presents an advantage to modify the dressed state interactions with coherent coupling in a time dependent manner. It is only limited by the speed needed to perform reversible Landau-Zener sweeps between internal states to remain in a single dressed state and does not introduce any additional loss

mechanism as compared to the optical Feshbach resonances. To proof its potential we have studied the mechanical instability which occurs when the effective interactions of the dressed states are quenched into the attractive regime. After a sudden interaction change, fluctuations of the density of the condensate are exponentially enhanced due to the attractive non-linear interactions, causing the formation of a bright soliton train formed by dressed states.

The experiments presented in this chapter have been performed together with A. Frölian, C. S. Chisholm and C. R. Cabrera.

This chapter is organized as follows. In section 5.2, we introduce the theoretical framework of coherently coupled interacting Bose-Einstein condensates. In section 5.2.1, we start by presenting the single particle dressed state picture. In section 5.2.2, we solve the scattering problem for two particles in coherently coupled dressed states. Then, in section 5.2.3, we show how the elastic and inelastic interactions are modified in a Bose-Einstein condensate in the strong coupling limit. Afterwards, in section 5.3.2, we present the experimental measurements on the modification of the elastic and inelastic scattering lengths . In section 5.3.3, we present the observation of dressed bright solitons using an adiabatic preparation and the formation of soliton trains after performing a quench of the interactions. Finally, in section 5.4 we draw the conclusions extracted from our experimental study and present future perspectives.

5.2   Theoretical framework: Coherently coupled interacting Bose Einstein Condensates

In this chapter we will explore the study of two Bose Einstein condensates with coherent coupling. The Hamiltonian $H = H_0 + H_{\text{int}}$ describing the physics of cold gases under the presence of coherent coupling can be split between a single particle contribution H_0 and a many body contribution stemming from two-body contact s-wave interactions H_{int}. The single particle contribution H_0 in second quantization reads:

$$H_0 = \sum_p \left[\left(\frac{p^2}{2m} + V_{\text{ext}} + \frac{\hbar\delta}{2} \right) a_{\uparrow p}^\dagger a_{\uparrow p} + \left(\frac{p^2}{2m} + V_{\text{ext}} - \frac{\hbar\delta}{2} \right) a_{\downarrow p}^\dagger a_{\downarrow p} \right] +$$
$$+ \sum_p \frac{\hbar\Omega}{2} (a_{\uparrow p}^\dagger a_{\downarrow p} + a_{\downarrow p}^\dagger a_{\uparrow p}), \tag{5.2.1}$$

where in addition to the kinetic $p^2/2m$ and potential term V_{ext}, we have included a coupling field with frequency ω between two states. We have labeled them for convenience as $|\uparrow\rangle$ and $|\downarrow\rangle$. The coupling field has a Rabi frequency Ω which is detuned from the $|\downarrow\rangle \to |\uparrow\rangle$ transition by $\delta = \omega - \omega_0$, where ω_0 corresponds to the bare frequency of the $|\downarrow\rangle \to |\uparrow\rangle$ transition, see Fig. 5.1(a). The creation $a_{sp_i}^\dagger$ and annihilation a_{sp_i} operators create and destroy particles in state $|s, p_i\rangle \equiv |s\rangle \otimes |p_i\rangle$, where $|s\rangle$ corresponds to the spin state in the $\{\uparrow, \downarrow\}$ basis[1]. These operators satisfy the common commutation relations $[a_{sp_i}^\dagger, a_{rp_j}] = \delta_{s,r}\delta_{i,j}$, $[a_{sp_i}, a_{rp_j}] = 0$ and $[a_{sp_i}^\dagger, a_{rp_j}^\dagger] = 0$.

The interaction Hamiltonian H_{int} in second quantization reads:

$$H_{\text{int}} = \frac{1}{2V} \sum_{p_i + p_j = p_k + p_l} \left[g_{\uparrow\uparrow} a_{\uparrow p_i}^\dagger a_{\uparrow p_j}^\dagger a_{\uparrow p_k} a_{\uparrow p_l} + g_{\downarrow\downarrow} a_{\downarrow p_i}^\dagger a_{\downarrow p_j}^\dagger a_{\downarrow p_k} a_{\downarrow p_l} + \right.$$
$$\left. + 2g_{\uparrow\downarrow} a_{\uparrow p_i}^\dagger a_{\downarrow p_j}^\dagger a_{\uparrow p_k} a_{\downarrow p_l} \right] \tag{5.2.2}$$

where the intra and inter-component interaction strengths correspond to $g_{\uparrow\uparrow} = 4\pi\hbar^2 a_{\uparrow\uparrow}/m$, $g_{\downarrow\downarrow} = 4\pi\hbar^2 a_{\downarrow\downarrow}/m$ and $g_{\uparrow\downarrow} = 4\pi\hbar^2 a_{\uparrow\downarrow}/m$ respectively.

To describe the physics of the coherently coupled Bose-Einstein condensates in the mean field approximation, we consider that all the atoms are in the zero momentum state. In consequence, we can substitute the creation and annihilation operators by complex numbers such that $a_{s,p=0} \to z_s = \sqrt{N_s}e^{i\theta_s}$ and we obtain the Gross-Pitaevskii Hamiltonian H_{GP}:

---

[1] Although we will work with multi-level atoms the detuning to other states will be large enough to neglect all the other transitions. Thus we often would refer to the pseudo-spin 1/2 states as spins for the sake of simplicity.
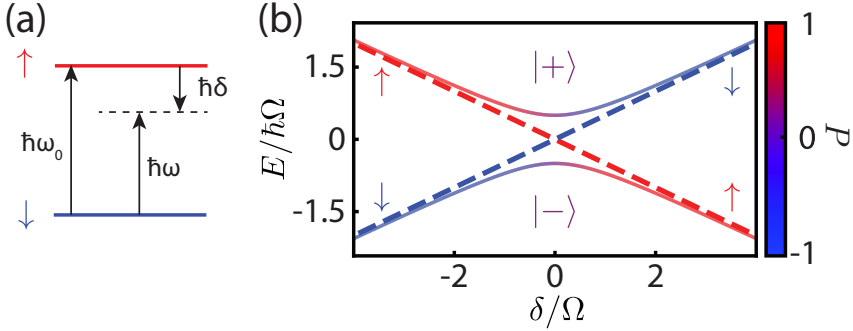
Figure 5.1: (a) Two-level atom with bare frequency ω_0 coupled by a field with frequency ω. The detuning is $\delta = \omega - \omega_0$. (b) Solid lines: Energy E of dressed states $|-\rangle$ and $|+\rangle$ vs. detuning δ, normalized to the Rabi frequency Ω. Dashed lines: Energy E of the bare states $|\uparrow\rangle$ (in red) and $|\downarrow\rangle$ (in blue) vs. detuning δ, normalized to the Rabi frequency Ω. Colorscale: state composition in terms of $P = \delta/\tilde{\Omega}$. Here $\uparrow$ and $\downarrow$ are the bare atomic states, and $\hbar\tilde{\Omega}$ the energy splitting of the dressed states.

$$
\begin{aligned}
H_{\mathrm{GP}} = & \left[-\tfrac{\hbar^2}{2m}\nabla^2 + V_{\mathrm{ext}} \right](N_\uparrow + N_\downarrow) + \\
& + \tfrac{\hbar\delta}{2}(N_\uparrow - N_\downarrow) + \hbar\Omega\sqrt{N_\uparrow N_\downarrow}\cos(\theta_\uparrow - \theta_\downarrow) + \\
& + \tfrac{1}{2V}\left[g_{\uparrow\uparrow}N_\uparrow^2 + g_{\downarrow\downarrow}N_\downarrow^2 + 2g_{\uparrow\downarrow}N_\uparrow N_\downarrow \right].
\end{aligned}
\tag{5.2.3}
$$

To understand the physics of the system, in section 5.2.1 we will start by describing the dressed state picture of a single two-level atom with coherent coupling. Then, in section 5.2.2, we will follow with the resolution of the scattering problem in the presence of coherent coupling to extract the elastic and inelastic scattering lengths of the dressed atoms. Finally, in section 5.2.3 we will study the zero-temperature many-body problem in the strong coupling limit by transforming the Gross-Pitaevskii Hamiltonian in the dressed state basis. We put particular emphasis on the modified elastic and inelastic interactions due the presence of the coupling field.

5.2.1   Coherently coupled dressed states

Let us consider the case where two states $|\uparrow\rangle \doteq [0\ 1]^T$ and $|\downarrow\rangle \doteq [1\ 0]^T$ are coherently coupled, see Fig. 5.1a. The Hamiltonian describing the system is:

$$H = \frac{\hbar}{2} \begin{bmatrix} \delta & \Omega \\ \Omega & -\delta \end{bmatrix}. \tag{5.2.4}$$

The eigenstates and eigenenergies of the Hamiltonian which satisfy $H\,|\pm\rangle = E_\pm\,|\pm\rangle$ are:

$$\begin{aligned} |+\rangle &= \cos\theta\,|\downarrow\rangle + \sin\theta\,|\uparrow\rangle \\ |-\rangle &= \sin\theta\,|\downarrow\rangle - \cos\theta\,|\uparrow\rangle, \end{aligned}$$

and:

$$E_\pm = \pm\frac{\hbar}{2}\tilde{\Omega} = \pm\frac{\hbar}{2}\sqrt{\delta^2 + \Omega^2} \tag{5.2.5}$$

respectively. Here the mixing angle θ is such that $\cos\theta = (1+P)^{1/2}/\sqrt{2}$ where $P = \delta/\tilde{\Omega}$ is the polarization and $\tilde{\Omega} = \sqrt{\Omega^2 + \delta^2}$ is the generalized Rabi frequency. We will call the states $|+\rangle$ and $|-\rangle$ as higher and lower dressed states respectively.

As it can be seen from the energy spectrum in Fig. 5.1b, an avoided crossing between the dressed states appears as a result of the coupling between the bare states. The energy gap at resonance corresponds to the Rabi frequency energy $\hbar\Omega$. The color code in Fig. 5.1b shows the composition of the dressed states. For $\delta \gg \Omega$, the lower (higher) dressed state corresponds to the $\uparrow$ ($\downarrow$) bare state as seen from the energy and composition of the states. Similarly for $\delta \ll -\Omega$, the lower (higher) dressed state corresponds to the $\downarrow$ ($\uparrow$) bare state.

5.2.2   Scattering of coherently coupled dressed states

The scattering of two particles in the ultra-cold atomic limit can be described by a single parameter, the scattering length. In our mixtures, as seen in Fig. 5.2a, the intra and inter-component scattering lengths correspond to $a_{\uparrow\uparrow}$, $a_{\downarrow\downarrow}$ and $a_{\uparrow\downarrow}$. But what happens when two coherently coupled particles collide? What is the scattering length corresponding to the collision of two dressed states? To address

this question we will solve the scattering problem including the driving from an external field.

Before solving this problem, we will make a brief reminder of the scattering theory in the ultracold limit. The scattering between two particles has been widely studied and a complete description of the problem can be found in reference [193].

Basic scattering theory in the ultracold limit

To describe the collisional properties between two particles (1 and 2) with mass m, we have to solve the time-independent Schrödinger equation of the relative motion between the two particles:

$$\left[\frac{\vec{p}^2}{2m_r} + V(r)\right]\psi_q = E_q\psi_q, \tag{5.2.6}$$

where $\vec{p} = (\vec{p_1} - \vec{p_2})/2$ is the relative momentum between the particles, $m_r = m/2$ is the reduced mass, $V(r)$ is a central interaction potential between the particles $(r = |\vec{r_1} - \vec{r_2}|)$, $E_q = \hbar^2 q^2/2m_r$ and ψ_q is the stationary scattering state. Here, we have assumed that the interaction potential has a range of action r_0, and that it tends to 0 when $r \rightarrow \infty$. In the ultracold limit the de Broglie wavelength λ_T associated to the particles is much larger than r_0. In this limit, the asymptotic limit of the stationary scattering states resulting from equation (5.2.6) can be described as the sum of an incoming plane wave, and an outgoing spherical wave such that:

$$\lim_{r \rightarrow \infty} \psi_q = e^{iqz} + f(q)\frac{e^{iqr}}{r} \tag{5.2.7}$$

where $f(q) = -a/(1 + iqa)$ is the s-wave scattering amplitude, a is the s-wave scattering length and we have chosen the relative momentum of the incident wave to be arbitrarily, and without loss of generality, in the z direction.

Let us now solve the scattering problem in the presence of coherent coupling.
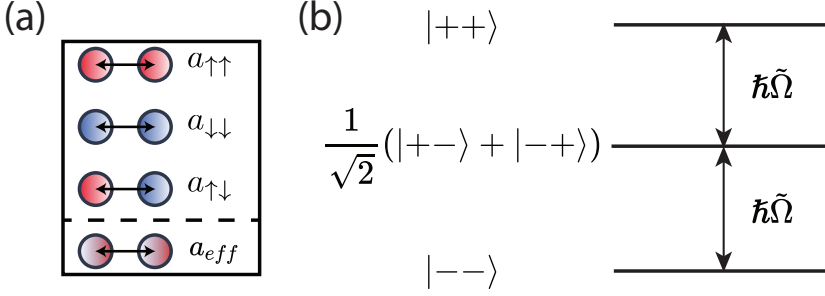
Figure 5.2: (a) Schematic representation of the intra- and inter-component bare scattering lengths $a_{\uparrow\uparrow}$, $a_{\downarrow\downarrow}$ and $a_{\uparrow\downarrow}$ vs. the effective scattering length a_{eff} of a dressed state. (b) Two particle dressed state energy levels separated by $\hbar\tilde{\Omega}$.

The scattering problem for coherently coupled dressed states

To solve the scattering problem in the presence of coherent coupling we will consider the two particle dressed states $|++\rangle$, $|--\rangle$ and $(|+-\rangle+|-+\rangle)/\sqrt{2}$. Since we will consider the collision between bosons, the two particle dressed states need to be symmetrical under exchange of two particles. Hence, we do not consider the $(|+-\rangle - |-+\rangle)/\sqrt{2}$ state. The two particle states are split by an energy $\hbar\tilde{\Omega}$ as shown in Fig. 5.2. Using the definitions from section 5.2.1, we can rewrite the two particle dressed states in terms of the two particle bare states:

$$
\begin{aligned}
|++\rangle &= \cos^2\theta \, |\downarrow\downarrow\rangle + \frac{\sin 2\theta}{\sqrt{2}}\left[\frac{1}{\sqrt{2}}\left(|\uparrow\downarrow\rangle + |\downarrow\uparrow\rangle\right)\right] + \sin^2\theta \, |\uparrow\uparrow\rangle \\
\frac{1}{\sqrt{2}}\left(|+-\rangle+|-+\rangle\right) &= \frac{\sin 2\theta}{\sqrt{2}} \, |\downarrow\downarrow\rangle - \cos 2\theta\left[\frac{1}{\sqrt{2}}\left(|\uparrow\downarrow\rangle + |\downarrow\uparrow\rangle\right)\right] - \frac{\sin 2\theta}{\sqrt{2}} \, |\uparrow\uparrow\rangle \\
|--\rangle &= \sin^2\theta \, |\downarrow\downarrow\rangle - \frac{\sin 2\theta}{\sqrt{2}}\left[\frac{1}{\sqrt{2}}\left(|\uparrow\downarrow\rangle + |\downarrow\uparrow\rangle\right)\right] + \cos^2\theta \, |\uparrow\uparrow\rangle \, .
\end{aligned}
$$
(5.2.8)

In the following, we introduce the calculation of the scattering problem with the dressed two particle channels. This calculation follows from discussions with D. S. Petrov, and is analogous to the calculations developed in references [51, 171]. After that we can obtain the elastic and inelastic scattering lengths for all

channels.

We shall remark that in the following calculation we have done an abuse of the notation of the out-going scattering amplitudes denoted as C and the normalization factors denoted as D. Although the notation has been repeated for each channel, they must be considered as independent for each scattering channel.

Scattering of the $|--\rangle$ channel: Let us consider the scattering of two particles in state $|-\rangle$. Since the collision are in the ultracold limit, the only open channel corresponds to the two particle state $|--\rangle$. In this case, the two particle states $|++\rangle$ and $(|+-\rangle + |-+\rangle)/\sqrt{2}$ are closed channels. We can describe the wavefunction of the two body scattered state in the relative coordinate system as outgoing spherical waves. The contribution of all these waves into the different channels plus the non-scattered wavefunction makes the stationary scattering wavefunction read:

$$\left|\psi^{sc}_{--}\right\rangle \approx (1 + f_{--}\frac{e^{iqr}}{r})\left|--\right\rangle + C_{+-}\frac{e^{ik_{+-}r}}{r}\left[\frac{1}{\sqrt{2}}(\left|+-\right\rangle + \left|-+\right\rangle)\right] + C_{++}\frac{e^{ik_{++}r}}{r}\left|++\right\rangle,$$
$$(5.2.9)$$

where f_{--} is the scattering amplitude of the lower dressed state $|-\rangle$, and C_{+-} and C_{++} is correspond to the scattering amplitude into the closed channels. Here q is the relative momentum between the particles and $k_{+-} = \sqrt{q^2 - m\tilde{\Omega}/\hbar}$ and $k_{++} = \sqrt{q^2 - 2m\tilde{\Omega}/\hbar}$ the relative momentum of particles scattered into the $\frac{1}{\sqrt{2}}(|+-\rangle + |-+\rangle)$ and $|++\rangle$ channels. Since the relative momentum of the particles q is much smaller than the gap to the $\frac{1}{\sqrt{2}}(|+-\rangle + |-+\rangle)$ and $|++\rangle$ states, $k_{+-} = i\kappa_{+-}$ and $k_{++} = i\kappa_{++}$ are purely imaginary. It is for this reason that they are called closed channels. From now on we will denote the wavefunction of scattered atoms into open channels as e^{ikr}/r and into closed channels as $e^{-\kappa r}/r$, such that:

$$\left|\psi^{sc}_{--}\right\rangle \approx (1 + f_{--}\frac{e^{iqr}}{r})\left|--\right\rangle \quad + \quad C_{+-}\frac{e^{-\kappa_{+-}r}}{r}\left[\frac{1}{\sqrt{2}}(\left|+-\right\rangle + \left|-+\right\rangle)\right]$$

$$+ \quad C_{++}\frac{e^{-\kappa_{++}r}}{r}\left|++\right\rangle . \tag{5.2.10}$$

By applying the zero-range Bethe-Peierls boundary conditions [194] we get that:

$$\lim_{r\to 0}\left\langle \sigma\sigma'\left|\psi^{sc}_{--}\right.\right\rangle \propto 1 - a_{\sigma\sigma'}/r, \tag{5.2.11}$$

where $\left|\sigma\sigma'\right\rangle$ is a state from the two-body bare state basis $\{\left|\uparrow\uparrow\right\rangle, \frac{1}{\sqrt{2}}(\left|\uparrow\downarrow\right\rangle+\left|\downarrow\uparrow\right\rangle)), \left|\downarrow\downarrow\right\rangle\}$. As a result we get three equations by projecting on $\left|\uparrow\uparrow\right\rangle$:

$$\cos^2\theta\left(1 + f_{--}\left(\frac{1}{r}+iq\right)\right) - \frac{C_{+-}\sin 2\theta}{\sqrt{2}}\left(\frac{1}{r}-\kappa_{+-}\right) +$$

$$+ \quad C_{++}\sin^2\theta\left(\frac{1}{r}-\kappa_{++}\right) = D_{\uparrow\uparrow}\left(1-\frac{a_{\uparrow\uparrow}}{r}\right), \tag{5.2.12}$$

by projecting on $\left|\downarrow\downarrow\right\rangle$:

$$\sin^2\theta\left(1 + f_{--}\left(\frac{1}{r}+iq\right)\right) + \frac{C_{+-}\sin 2\theta}{\sqrt{2}}\left(\frac{1}{r}-\kappa_{+-}\right) +$$

$$+ \quad C_{++}\cos^2\theta\left(\frac{1}{r}-\kappa_{++}\right) = D_{\downarrow\downarrow}\left(1-\frac{a_{\downarrow\downarrow}}{r}\right), \tag{5.2.13}$$

and by projecting on $\frac{1}{\sqrt{2}}(\left|\uparrow\downarrow\right\rangle + \left|\downarrow\uparrow\right\rangle)$:

$$-\frac{\sin 2\theta}{\sqrt{2}}\left(1 + f_{--}\left(\frac{1}{r}+iq\right)\right) - C_{+-}\cos 2\theta\left(\frac{1}{r}-\kappa_{+-}\right) +$$

$$+ \quad \frac{C_{++}\sin 2\theta}{\sqrt{2}}\left(\frac{1}{r}-\kappa_{++}\right) = D_{\uparrow\downarrow}\left(1-\frac{a_{\uparrow\downarrow}}{r}\right). \tag{5.2.14}$$

A system of 6 equations and 6 unknowns $\{f_{--}, C_{+-}, C_{++}, D_{\uparrow\uparrow}, D_{\downarrow\downarrow}, D_{\uparrow\downarrow}\}$ is obtained by gathering the terms which are proportional to $1/r$ and the terms which are not.

Scattering of the $|++\rangle$ channel: Let us consider the scattering of two particles in state $|++\rangle$ in the ultracold limit. In this case all the channels are open and the stationary scattering state reads:

$$\left|\psi_{++}^{sc}\right\rangle \approx (1+f_{++}\frac{e^{iqr}}{r})\,|--\rangle+C_{+-}\frac{e^{ik_{+-}r}}{r}\left[\frac{1}{\sqrt{2}}(|+-\rangle+|-+\rangle)\right]+C_{--}\frac{e^{ik_{--}r}}{r}\,|--\rangle\,,$$
$$(5.2.15)$$

where f_{++} is the scattering amplitude of the higher dressed states $|+\rangle$, and C_{+-} and C_{--} correspond to the scattering amplitude into the $\frac{1}{\sqrt{2}}(|+-\rangle+|-+\rangle)$ and $|--\rangle$ channels. Here $k_{+-}=\sqrt{q^2+m\tilde{\Omega}/\hbar}$ and $k_{--}=\sqrt{q^2+2m\tilde{\Omega}/\hbar}$ correspond to the momentum of particles scattered into the $\frac{1}{\sqrt{2}}(|+-\rangle+|-+\rangle)$ and $|--\rangle$ channels.

Similarly, applying the zero-range boundary conditions to the $\left|\psi_{++}^{sc}\right\rangle$ state, we project on the $|\uparrow\uparrow\rangle$, $|\downarrow\downarrow\rangle$ and $(|\uparrow\downarrow\rangle+|\downarrow\uparrow\rangle)/\sqrt{2}$ states respectively:

$$\sin^2\theta\left(1+f_{++}\left(\frac{1}{r}+iq\right)\right)-\frac{C_{+-}\sin 2\theta}{\sqrt{2}}\left(\frac{1}{r}+ik_{+-}\right)+$$
$$+\quad C_{--}\cos^2\theta\left(\frac{1}{r}+ik_{--}\right)=D_{\uparrow\uparrow}\left(1-\frac{a_{\uparrow\uparrow}}{r}\right),\qquad\qquad(5.2.16)$$

$$\cos^2\theta\left(1+f_{++}\left(\frac{1}{r}+iq\right)\right)+\frac{C_{+-}\sin 2\theta}{\sqrt{2}}\left(\frac{1}{r}+ik_{+-}\right)+$$
$$+\quad C_{--}\sin^2\theta\left(\frac{1}{r}+ik_{--}\right)=D_{\downarrow\downarrow}\left(1-\frac{a_{\downarrow\downarrow}}{r}\right),\qquad\qquad(5.2.17)$$

$$\frac{\sin 2\theta}{\sqrt{2}}\left(1+f_{++}\left(\frac{1}{r}+iq\right)\right)-C_{+-}\cos 2\theta\left(\frac{1}{r}+ik_{+-}\right)-$$
$$-\quad\frac{C_{--}\sin 2\theta}{\sqrt{2}}\left(\frac{1}{r}+ik_{--}\right)=D_{\uparrow\downarrow}\left(1-\frac{a_{\uparrow\downarrow}}{r}\right),\qquad\qquad(5.2.18)$$

A system of 6 equations and 6 unknowns $\{f_{++},C_{+-},C_{--},D_{\uparrow\uparrow},D_{\downarrow\downarrow},D_{\uparrow\downarrow}\}$ is obtained by gathering the terms which are proportional to $1/r$ and the terms which are not.

Scattering of the $\frac{1}{\sqrt{2}}(|+-\rangle + |-+\rangle)$ channel: Finally we consider the scattering of two particles in state $\frac{1}{\sqrt{2}}(|+-\rangle + |-+\rangle)$ in the ultracold limit. In this case the $|--\rangle$ is an open channel and the $|++\rangle$ channel is closed. Hence, the stationary scattering wavefunction reads:

$$|\psi_{+-}^{sc}\rangle \approx (1 + f_{+-}\frac{e^{iqr}}{r})\left[\frac{1}{\sqrt{2}}(|+-\rangle + |-+\rangle)\right] + C_{++}\frac{e^{-\kappa_{++}r}}{r}|++\rangle +$$
$$+ \quad C_{--}\frac{e^{ik_{--}r}}{r}|--\rangle, \tag{5.2.19}$$

where f_{+-} is the scattering amplitude between the states $|+\rangle$ and $|-\rangle$, and C_{++} and C_{--} correspond to the scattering amplitude into the $|++\rangle$ and $|--\rangle$ channels. Here $\kappa_{++} = \sqrt{m\tilde{\Omega}/\hbar - q^2}$ and $k_{--} = \sqrt{m\tilde{\Omega}/\hbar + q^2}$ correspond to the momentum of particles scattered into the $|++\rangle$ and $|--\rangle$ channels.

Applying the zero-range boundary conditions to the $|\psi_{+-}^{sc}\rangle$ state, we project on the $|\uparrow\uparrow\rangle$, $|\downarrow\downarrow\rangle$ and $\frac{1}{\sqrt{2}}(|\uparrow\downarrow\rangle + |\downarrow\uparrow\rangle)$ states respectively:

$$- \quad \frac{\sin 2\theta}{\sqrt{2}}\left(1 + f_{+-}\left(\frac{1}{r} + iq\right)\right) + C_{++}\sin^2\theta\left(\frac{1}{r} - \kappa_{++}\right) +$$
$$+ \quad C_{--}\cos^2\theta\left(\frac{1}{r} + ik_{--}\right) = D_{\uparrow\uparrow}\left(1 - \frac{a_{\uparrow\uparrow}}{r}\right), \tag{5.2.20}$$

$$\frac{\sin 2\theta}{\sqrt{2}}\left(1 + f_{+-}\left(\frac{1}{r} + iq\right)\right) + C_{++}\cos^2\theta\left(\frac{1}{r} - \kappa_{++}\right) +$$
$$+ \quad C_{--}\sin^2\theta\left(\frac{1}{r} + ik_{--}\right) = D_{\downarrow\downarrow}\left(1 - \frac{a_{\downarrow\downarrow}}{r}\right), \tag{5.2.21}$$

$$- \quad \cos 2\theta\left(1 + f_{+-}\left(\frac{1}{r} + iq\right)\right) + \frac{C_{++}\sin 2\theta}{\sqrt{2}}\left(\frac{1}{r} - \kappa_{++}\right) -$$
$$- \quad \frac{C_{--}\sin 2\theta}{\sqrt{2}}\left(\frac{1}{r} + ik_{--}\right) = D_{\uparrow\downarrow}\left(1 - \frac{a_{\uparrow\downarrow}}{r}\right), \tag{5.2.22}$$

A system of 6 equations and 6 unknowns $\{f_{+-}, C_{++}, C_{--}, D_{\uparrow\uparrow}, D_{\downarrow\downarrow}, D_{\uparrow\downarrow}\}$ is obtained by gathering the terms which are proportional to $1/r$ and the terms

which are not.

From all these equations, we can obtain the elastic scattering in each channel and the inelastic scattering between different channels. We will start with the description of the elastic scattering.
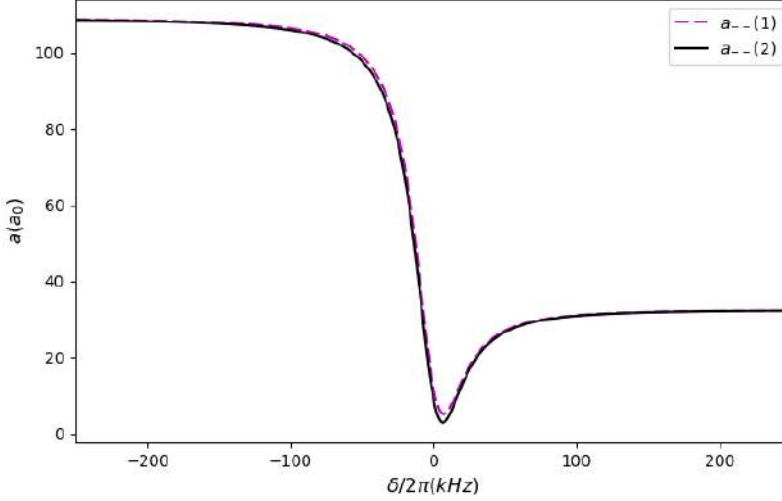

Figure 5.3: Elastic scattering properties. Exemplary scattering lengths a_{--} computed with (1) equation (5.2.23) (magenta dashed lines) and (2) equation (5.2.24) (black solid line) describing the interaction on the $|--\rangle$ channels vs. δ considering $a_{\uparrow\uparrow} = 32.5a_0$, $a_{\downarrow\downarrow} = 109a_0$ and $a_{\uparrow\downarrow} = -52.9a_0$ and $\Omega/2\pi = 20$kHz. Here a_0 corresponds to the Bohr radius.

Elastic scattering

By solving the systems of equations {(5.2.12),(5.2.13),(5.2.14)}, {(5.2.16),(5.2.17), (5.2.18)} and {(5.2.20), (5.2.21),(5.2.22)} we can obtain the scattering amplitudes of the dressed state scattering channels f_{--}, f_{++} and f_{+-} respectively. In this section we focus on the elastic scattering, which corresponds to the negative real part of the scattering amplitude. In the limit where $q \to 0$, we have that the elastic scattering length $a = -\operatorname{Re}\{f\}$. In particular, we focus on the

scattering between particles on the ground dressed state $|-\rangle$. From equations $\{(5.2.12),(5.2.13),(5.2.14)\}$ we obtain:

$$a_{--} = a_{\downarrow\downarrow} \sin^4 \theta + a_{\uparrow\uparrow} \cos^4 \theta + \frac{1}{2} a_{\uparrow\downarrow} \sin^2 2\theta + O(\kappa), \qquad (5.2.23)$$

where $\kappa = (\hbar\tilde{\Omega}/m)^{1/2}$. Indeed, as we will show in section 5.2.3, a similar result was obtained in reference [52] by transforming the interaction Hamiltonian from equation 5.2.2 into the dressed state basis:

$$a_{--} = a_{\downarrow\downarrow} \sin^4 \theta + a_{\uparrow\uparrow} \cos^4 \theta + \frac{1}{2} a_{\uparrow\downarrow} \sin^2 2\theta. \qquad (5.2.24)$$

The correction in κ is due to the admixture of the closed channels and it converges to the results obtained in reference [52] for $\tilde{\Omega} \to 0$. In particular, in reference [171] the scattering amplitude of the $|--\rangle$ channel, was computed in the case where $a_{\uparrow\uparrow} = a_{\downarrow\downarrow} = a$ and $\theta = \pi/4$ ($\delta = 0$), obtaining:

$$f(q) = -\left(\frac{2 - (a + a_{\uparrow\downarrow})\kappa}{a + a_{\uparrow\downarrow} - 2a_{\uparrow\downarrow}a\kappa} + iq \right)^{-1}. \qquad (5.2.25)$$

In this case, it is easy to observe that for $q \to 0$ and $\kappa \to 0$, the scattering length $a_{--} = -\operatorname{Re}\{f(q)\}$ from equation (5.2.25) converges to the result from equation (5.2.24) for $a_{\uparrow\uparrow} = a_{\downarrow\downarrow} = a$. In Fig. 5.3 we plot both results for typical experimental parameters. As it can be observed, the correction is very small.

Inelastic scattering

We will focus on the description of the inelastic decay from colliding particles in the excited dressed state $|+\rangle$. In this case, particles can decay into the open channels $\frac{1}{\sqrt{2}}(|+-\rangle + |-+\rangle)$ and $|--\rangle$ with a momentum k_{+-} and k_{--}. The scattering amplitudes C_{+-} and C_{--} obtained from equations $\{(5.2.16),(5.2.17),(5.2.18)\}$ give the probability to decay into the $\frac{1}{\sqrt{2}}(|+-\rangle + |-+\rangle)$ and $|--\rangle$ channels. We can characterize them by an inelastic scattering length $a^{\mathrm{in}} = -\operatorname{Re}\{C\}$ In Fig. 5.4 we plot the scattering length associated to the decay of $|++\rangle$ into other channels. The corresponding inelastic cross-section for identical bosons is then given by $\sigma^{\mathrm{in}} = 8\pi a^{\mathrm{in}^2}$
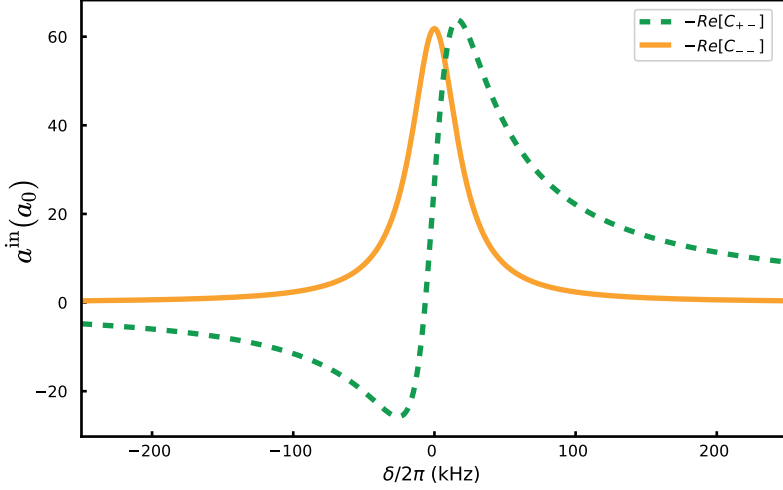
Figure 5.4: Inelastic scattering properties. Exemplary elastic scattering length associated to the decay on the $|++\rangle \rightarrow |--\rangle$ ($-\operatorname{Re}\{C_{--}\}$) and $|++\rangle \rightarrow \frac{1}{\sqrt{2}}(|+-\rangle + |-+\rangle)$ channels ($-\operatorname{Re}\{C_{+-}\}$) vs. δ considering $a_{\uparrow\uparrow} = 32.5a_0$, $a_{\downarrow\downarrow} = 109a_0$ and $a_{\uparrow\downarrow} = -52.9a_0$ and $\Omega/2\pi = 20$kHz.

Up to now we have studied the modification of the two-body scattering between particles in the presence of coherent coupling. Let us now, solve the many-body problem. In particular, we will focus on the modification of the interactions in a two-component Bose-Einstein condensate in the presence of a strong coherent coupling.

5.2.3 The strong coupling limit in composite Bose Einstein condensates

In this section, we will introduce how the effective interactions are modified due to the presence of the coupling in a two-component BEC. This problem was studied in detail in reference [52] in the strong coupling limit $\hbar\Omega \gg \frac{p^2}{2m}, g_{\uparrow\uparrow}n, g_{\downarrow\downarrow}n, g_{\uparrow\downarrow}n$. In this limit, we can approximate the eigenstates of the Hamiltonian to be N particles in the dressed states $|+\rangle$ and $|-\rangle$ with modified interactions. Hence, we can conveniently rewrite the interaction hamiltonian H_{int} from equation (5.2.2)

in the dressed state basis:

$$H_{\text{int}} = \frac{1}{2V} \sum_{p_i + p_j = p_k + p_l} g_1 a^\dagger_{+p_i} a^\dagger_{+p_j} a_{+p_k} a_{+p_l} +$$
$$+ g_2 a^\dagger_{-p_i} a^\dagger_{-p_j} a_{-p_k} a_{-p_l} + g_3 a^\dagger_{+p_i} a^\dagger_{-p_j} a_{+p_k} a_{-p_l} +$$
$$+ g_4 (a^\dagger_{+p_i} a^\dagger_{+p_j} a_{-p_k} a_{-p_l} + a^\dagger_{-p_i} a^\dagger_{-p_j} a_{+p_k} a_{+p_l}) +$$
$$+ g_5 (a^\dagger_{+p_i} a^\dagger_{+p_j} a_{+p_k} a_{-p_l} + a^\dagger_{-p_i} a^\dagger_{+p_j} a_{+p_k} a_{+p_l}) +$$
$$+ g_6 (a^\dagger_{+p_i} a^\dagger_{-p_j} a_{-p_k} a_{-p_l} + a^\dagger_{-p_i} a^\dagger_{-p_j} a_{-p_k} a_{+p_l}),$$

$$(5.2.26)$$

where the first three-terms preserving the two-particle dressed state of the colliding atoms correspond to the elastic scattering between $|-\rangle \leftrightarrow |-\rangle$, $|+\rangle \leftrightarrow |+\rangle$ and $|+\rangle \leftrightarrow |-\rangle$ atoms respectively. Instead, the last three terms modify the two-particle dressed state of the colliding atoms. They correspond to inelastic dressed state changing collisions between the $|++\rangle \leftrightarrow |--\rangle$, $|++\rangle \leftrightarrow \frac{1}{\sqrt{2}}(|+-\rangle + |-+\rangle)$ and $|--\rangle \leftrightarrow \frac{1}{\sqrt{2}}(|+-\rangle + |-+\rangle)$ channels respectively. By doing the proper algebra, the g_{1-6} coefficients can be rewritten in terms of the bare state interaction strengths $g_{\uparrow\uparrow}$, $g_{\downarrow\downarrow}$ and $g_{\uparrow\downarrow}$:

$$g_1 = g_{\downarrow\downarrow} \cos^4 \theta + g_{\uparrow\uparrow} \sin^4 \theta + \frac{1}{2} g_{\uparrow\downarrow} \sin^2 2\theta \qquad (5.2.27)$$

$$g_2 = g_{\downarrow\downarrow} \sin^4 \theta + g_{\uparrow\uparrow} \cos^4 \theta + \frac{1}{2} g_{\uparrow\downarrow} \sin^2 2\theta \qquad (5.2.28)$$

$$g_3 = (g_{\downarrow\downarrow} + g_{\uparrow\uparrow}) \sin^2 2\theta + 2 g_{\uparrow\downarrow} \cos^2 2\theta \qquad (5.2.29)$$

$$g_4 = \frac{1}{4} (g_{\downarrow\downarrow} + g_{\uparrow\uparrow} - 2 g_{\uparrow\downarrow}) \sin^2 2\theta \qquad (5.2.30)$$

$$g_5 = \sin 2\theta \left(g_{\uparrow\uparrow} \sin^2 \theta - g_{\downarrow\downarrow} \cos^2 \theta + g_{\uparrow\downarrow} \cos 2\theta \right) \qquad (5.2.31)$$

$$g_6 = \sin 2\theta \left(g_{\uparrow\uparrow} \cos^2 \theta - g_{\downarrow\downarrow} \sin^2 \theta - g_{\uparrow\downarrow} \cos 2\theta \right) \qquad (5.2.32)$$

If $g_{\uparrow\uparrow} = g_{\downarrow\downarrow} = g_{\uparrow\downarrow} = g$ then $g_1 = g_2 = g$, $g_3 = 2g$ and $g_4 = g_5 = g_6 = 0$. Thus, the elastic terms are not modified by the presence of the coherent coupling and the dressed state changing collisions are suppressed by the symmetry of the interactions. Instead, if the bare state interaction strengths are different both

elastic and inelastic collisions might be relevant and modified by the presence of the coupling. For a BEC in state $|-\rangle$, inelastic collisions are energetically forbidden and only elastic processes remain. In contrast, for a BEC in state $|+\rangle$ both elastic and inelastic processes are relevant. As seen from equations (5.2.27) - (5.2.32) the interaction properties depend on the interaction strengths of the bare states and on the composition of the system.

Elastic scattering

The elastic g_{1-3} coefficients are related with the dressed state interaction strengths as seen from the symmetric case. Thus the dressed state elastic scattering lengths are:

$$a_{++} = a_{\downarrow\downarrow}\cos^4\theta + a_{\uparrow\uparrow}\sin^4\theta + \frac{1}{2}a_{\uparrow\downarrow}\sin^2 2\theta \qquad (5.2.33)$$

$$a_{--} = a_{\downarrow\downarrow}\sin^4\theta + a_{\uparrow\uparrow}\cos^4\theta + \frac{1}{2}a_{\uparrow\downarrow}\sin^2 2\theta \qquad (5.2.34)$$

$$a_{+-} = \frac{1}{2}(a_{\downarrow\downarrow} + a_{\uparrow\uparrow})\sin^2 2\theta + a_{\uparrow\downarrow}\cos^2 2\theta \qquad (5.2.35)$$

As commented before, re-expressing H_{int}^{MF} in the dressed state basis gives the correct scattering lengths modulo corrections of $O(\kappa)$. This result is however only valid for small values of a, whereas the scattering result presented before is more general.

In our experiment we will explore a system where all the bare state scattering lengths are different, the intra-state scattering lengths $a_{\uparrow\uparrow}, a_{\downarrow\downarrow} > 0$ and the inter-state scattering length $a_{\uparrow\downarrow} < 0$. In this situation, the scattering lengths for large detunings $|\delta| \gg \Omega$ correspond to the bare state scattering length and get modified for $|\delta| \sim \Omega$, as it can be observed from Fig. 5.5a and Fig. 5.5b.

For instance, if we focus on the interactions between the lower dressed states $|-\rangle$, we can observe that: for $\delta \gg \Omega \rightarrow P = 1$ and $a_{--} \rightarrow a_{\uparrow\uparrow}$, for $\delta \ll -\Omega \rightarrow P = -1$ and $a_{--} \rightarrow a_{\downarrow\downarrow}$, and for $\delta = 0 \rightarrow P = 0$ and $a_{--} = (a_{\downarrow\downarrow} + a_{\uparrow\uparrow} + 2a_{\uparrow\downarrow})/4$. The minimum effective scattering length $a_{--}^{\min}$ corresponds to:
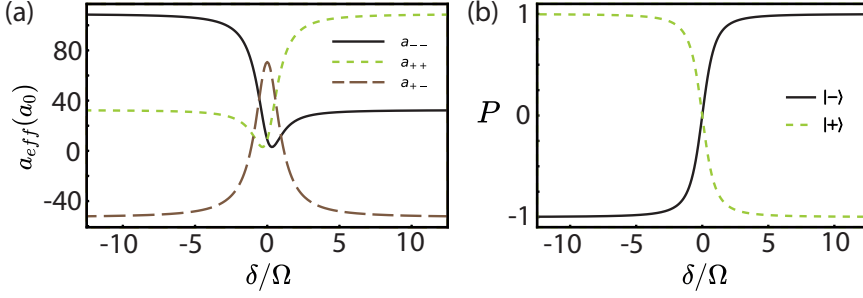
Figure 5.5: Elastic scattering properties. (a) Exemplary effective scattering lengths a_{--} (solid black), a_{++} (dashed green) and a_{+-} (dashed brown) describing the interaction on the $|--\rangle$, $|++\rangle$ and $\frac{1}{\sqrt{2}}\left(|+-\rangle+|-+\rangle\right)$ channels vs. δ/Ω considering $a_{\uparrow\uparrow} = 32.5a_0$, $a_{\downarrow\downarrow} = 109a_0$ and $a_{\uparrow\downarrow} = -52.9a_0$. Here a_0 corresponds to the Bohr radius. (b) Polarization of the $|-\rangle$ (solid black) and $|+\rangle$ (dashed green) vs. δ/Ω.

$$a_{--}^{\min} = \frac{a_{\downarrow\downarrow}a_{\uparrow\uparrow} - a_{\downarrow\uparrow}^2}{a_{\downarrow\downarrow} + a_{\uparrow\uparrow} - 2a_{\downarrow\uparrow}} \tag{5.2.36}$$

which is met at a polarization $P = (a_{\downarrow\downarrow} - a_{\uparrow\uparrow})/(a_{\downarrow\downarrow} + a_{\uparrow\uparrow} - 2a_{\uparrow\downarrow})$. Since we have broad tunability of the scattering lengths, we can make $a_{--}^{\min} < 0$ in order to explore attractively interacting dressed state systems (see section 5.3).

Inelastic scattering

The inelastic g_{4-6} coefficients indicate the strength of the dressed state changing collisions. But are all the dressed state changing collisions allowed? Since $\hbar\Omega \gg \frac{p^2}{2m}, g_{\uparrow\uparrow}n$,
$g_{\downarrow\downarrow}n, g_{\uparrow\downarrow}n$, the following transitions are energetically forbidden:

$$
\begin{aligned}
|--\rangle &\rightarrow \frac{1}{\sqrt{2}}\left(|+-\rangle+|-+\rangle\right) \\
|--\rangle &\rightarrow |++\rangle \\
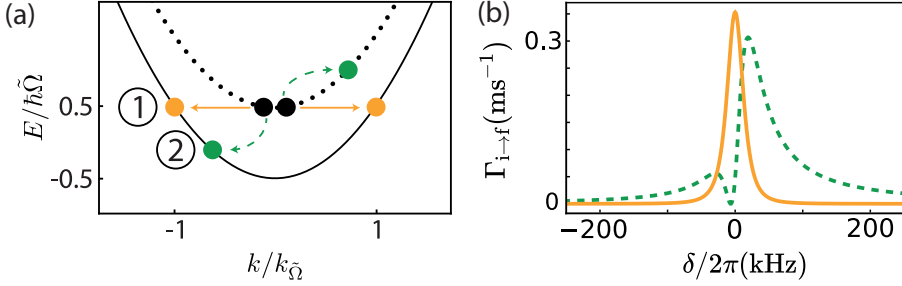\frac{1}{\sqrt{2}}\left(|+-\rangle+|-+\rangle\right) &\rightarrow |++\rangle
\end{aligned}
\tag{5.2.37}
$$

Figure 5.6: Inelastic decay of the higher dressed state. (a) Sketch of possible dressed state changing collisions ①: $|+,+\rangle \to |--\rangle$ (orange, solid arrows) and ②: $|++\rangle \to (|+-\rangle + |-+\rangle)/\sqrt{2}$ (green, dashed arrows). Single particle energy dispersion E and momentum k are expressed in terms of $\tilde{\Omega} = \sqrt{\Omega^2 + \delta^2}$ and $k_{\tilde{\Omega}} = \sqrt{2m\tilde{\Omega}/\hbar}$, respectively. (b) Decay rate $\Gamma_{i\to f}$ vs. δ considering typical experimental Rabi frequency $\Omega/2\pi = 20$ kHz and density of a BEC $n_i = 1.3 \times 10^{20}\mathrm{m}^{-3}$.

Instead all the other transitions are allowed, resulting in a transformation from the coupling energy into kinetic energy. Hence, the kinetic energy is not conserved in this process and the dressed state changing collision processes are inelastic. In particular, we will focus on the inelastic decay from the $|++\rangle \to |--\rangle$ and $|++\rangle \to \frac{1}{\sqrt{2}}(|+-\rangle + |-+\rangle)$ transitions, which are sketched in figure 5.6 as the process ① and ② respectively. To compute the transition rate $\Gamma_{i\to f}$ to lowest order between the initial and final states $|i\rangle$ and $|f\rangle$ we can use the Fermi-golden rule:

$$\Gamma_{i\to f} = \frac{2\pi}{\hbar}|\langle f| H_{\mathrm{int}} |i\rangle|^2 \rho(E_f), \qquad (5.2.38)$$

where $\langle f| H_{\mathrm{int}} |i\rangle$ is the transition matrix element and $\rho(E_f)$ corresponds to the density of states of the final state. Since the collision process is a two-body process the decay is described by the loss rate equation:

$$\dot{n}_i = -2\Gamma_{i\to f}(n_i)n_i, \qquad (5.2.39)$$

where n_i is the atomic density and the 2 takes into account the loss of two atoms.

From the Fermi-golden rule and equation (5.2.39) we obtain that:

$$\dot{n}_i = -g^{(2)} \sigma_f v_f n_i^2, \tag{5.2.40}$$

where $g^{(2)}$ is the two-body correlation function (which is equal to 1 for a BEC and 2 for a thermal gas), σ_f is the inelastic scattering cross section, v_f is the velocity of the final states and we have taken into account the density of atomic pairs $n_i^2/2$. From the results of equation (5.2.30) and (5.2.31) taken from reference [52], or equivalently, from the the scattering amplitude into the open channels computed in section 5.2.2, we obtain an inelastic cross-section:

$$\sigma_1 = \frac{\pi}{2} \left[(a_{\uparrow\uparrow} + a_{\downarrow\downarrow} - 2a_{\uparrow\downarrow}) \sin^2 2\theta \right]^2, \tag{5.2.41}$$

for the $|++\rangle \to |--\rangle$ process and:

$$\sigma_2 = 4\pi \left[\left(a_{\uparrow\uparrow} \sin^2 \theta - a_{\downarrow\downarrow} \cos^2 \theta + a_{\uparrow\downarrow} \cos 2\theta \right) \sin 2\theta \right]^2, \tag{5.2.42}$$

for the $|++\rangle \to \frac{1}{\sqrt{2}} (|+-\rangle + |-+\rangle)$ process, where we have taken into account the symmetrization of identical bosons to compute the scattering cross-section. The final velocities for the two processes are $v_{f1} = \sqrt{2\hbar\tilde{\Omega}/m}$ and $v_{f2} = \sqrt{\hbar\tilde{\Omega}/m}$ respectively.

In figure 5.6(b) we show typical decay rates for a BEC for both processes. We can see that the scattering rates can be strongly modified depending on the detuning. Whereas the ① process is symmetric with respect to the resonance the ② process is not. In section 5.3.2 we will explore the $|++\rangle$ state decay into both $|--\rangle$ and $\frac{1}{\sqrt{2}} (|+-\rangle + |-+\rangle)$ by measuring the final velocities and the fraction of scattered atoms as a function of the detuning.

5.3 Experimental realization

As introduced in the theoretical framework, the coherent coupling of two states with unequal interactions results in an effective modification of the interactions of the dressed states. In our experiment, we use this phenomena as an alternative method for controlling interactions in a fast and flexible manner. In our scheme,

two internal states of a BEC with different scattering lengths are coherently-coupled exploiting a radio-frequency (rf) field, which modifies the scattering properties of the corresponding dressed states. Until now, this effect could only be observed indirectly through the change of miscibility of binary BEC mixtures [55–57]. Here we show that exploiting a system with inter- and intra-state interactions of opposite signs enables large modifications of the elastic and inelastic scattering properties of these dressed states. They can be flexibly controlled by adjusting the parameters of the coupling field, giving also access to the attractive regime. In this case, we demonstrate the stabilization of bright solitons formed by dressed state atoms. Furthermore, we exploit the high temporal bandwidth of this technique to quench the interactions from repulsive to attractive values, and observe how the resulting modulational instability develops into a bright soliton train.
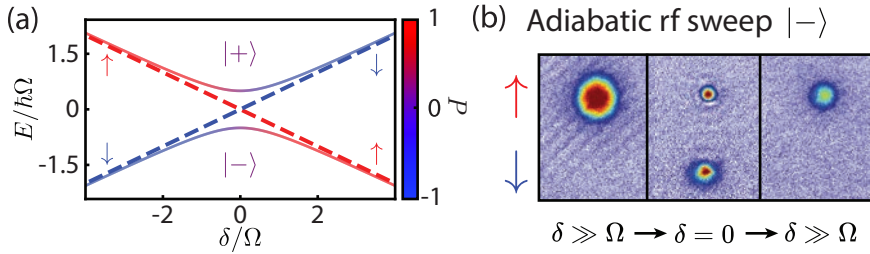

Figure 5.7: Adiabatic preparation of the lower dressed state. (a) Energy E of dressed states $|-\rangle$ and $|+\rangle$ vs. detuning δ, normalized to the Rabi frequency Ω. Colorscale: state composition in terms of $P = \delta/\tilde{\Omega}$. Here $\uparrow$ and $\downarrow$ are the bare atomic states. (b) Sketch of the adiabatic rf sweep used to prepare the $|-\rangle$ state adiabatically. Images of the bare states $|\uparrow\rangle$ and $|\downarrow\rangle$ before starting the rf sweep (left panel), after the first rf sweep to prepare $|-\rangle$ (middle panel) and after a secon rf sweep to recover the $|\uparrow\rangle$ taken with Stern Gerlach separation during time of flight expansion.

5.3.1   Methods

We implement these concepts with a ^{39}K BEC at magnetic fields $B \sim 56 - 57$ G. As atomic states we exploit the $m_F = -1$ and 0 magnetic sublevels of the $F = 1$ hyperfine manifold $|\uparrow\rangle \equiv |F, m_F\rangle = |1, -1\rangle$ and $|\downarrow\rangle \equiv |1, 0\rangle$, for which the intra-

state scattering lenghts are repulsive ($a_{\uparrow\uparrow}, a_{\downarrow\downarrow} > 0$), and the inter-state scattering length is attractive ($a_{\uparrow\downarrow} < 0$) [29, 30]. We coherently-couple the two states with an rf field. For all experiments its Rabi frequency $\Omega/2\pi > 8$ kHz defines the dominant energy scale of the system and the system is conveniently described by the dressed states $|-\rangle = \sin\theta\,|\downarrow\rangle - \cos\theta\,|\uparrow\rangle$ and $|+\rangle = \cos\theta\,|\downarrow\rangle + \sin\theta\,|\uparrow\rangle$.

We prepare single dressed states through Landau-Zener sweeps, starting from state $|\uparrow\rangle$ (unless explicitly stated otherwise). We have crosschecked the reversibility of our Landau-Zener sweeps by ramping the detuning[2] δ at a rate ≤ 1 kHz/μs. In Fig. 5.7 we show that after preparing the $|-\rangle$ state we can invert the Landau-Zener sweep without populating the $|\downarrow\rangle$ state. Moreover we can observe in the middle panel of Fig. 5.7b that the size of the BEC after time of flight is reduced. This is a signature of the modification of the scattering length. Notice that after the Landau-Zener sweep is inverted we have less atoms. This is because the $|\downarrow\rangle$ state has a larger three-body recombination rate as shown in chapters 3 and 4. Nevertheless, since the timescale of three-body losses is longer than $1/\Omega$, these losses do not affect the coherence between the $|\uparrow\rangle$ and $|\downarrow\rangle$ states.

5.3.2   Modified interactions

Elastic scattering

In a first series of experiments we focus on the elastic scattering properties of the lower dressed state $|-\rangle$. They are characterized by the effective scattering length $a_{--} = a_{\uparrow\uparrow}\cos^4\theta + a_{\downarrow\downarrow}\sin^4\theta + \frac{1}{2}a_{\uparrow\downarrow}\sin^2 2\theta$ as seen from equation (5.2.28) [52], and thus depend on the state composition of the system *via* the detuning δ.

We experimentally probe this dependency by performing expansion measurements in an optical waveguide. To this end, we prepare a BEC in state $|-\rangle$ with $\Omega/2\pi = 20.0(6)$ kHz and variable detuning δ using a ramp rate of 0.83 kHz/ms. The magnetic field is set to $B = 57.280(2)$ G, for which $a_{\uparrow\uparrow}/a_0 = 32.5$, $a_{\downarrow\downarrow}/a_0 = 109$, $a_{\uparrow\downarrow}/a_0 = -52.9$, and we always have $a_{--} > 0$. Here a_0 is the Bohr radius. After holding the gas for 5 ms at the final detuning, we switch off the axial confinement abruptly, allowing it to expand for 21 ms along a single-beam

---

[2]The detuning uncertainty is ± 1.5 kHz, limited by short-term magnetic field fluctuations (± 2 mG). This restricts the ramp rates and Rabi frequencies accessible in our setup. The latter are calibrated independently through Rabi oscillations.
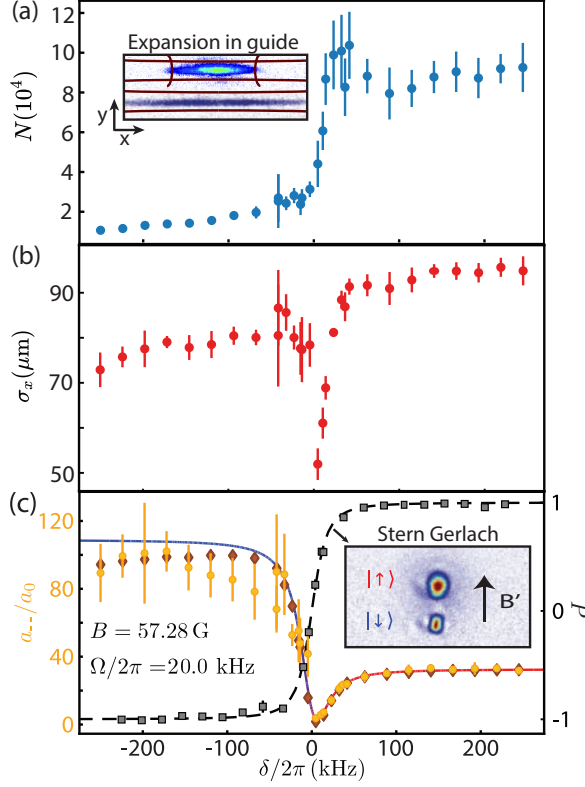
Figure 5.8: Elastic scattering properties of the lower dressed state. (a) Atom number N and (b) axial size σ_x measured after expansion of the BEC in an optical waveguide vs. detuning. (c) Orange circles, left axis: Experimental value of a_{--} obtained by scaling σ_x^5/N to yield $a_{\uparrow\uparrow}$ at large positive δ. Solid line, left axis: Scattering length of the $|-\rangle$ state. Colorscale of the a_{--} curve: value of P as seen from Fig. 5.7. Brown diamonds, left axis: numerical simulation of the expansion. We rescale the predicted σ_x^5/N to yield $a_{\uparrow\uparrow}$ at large positive δ. Gray squares, right axis: Polarization P vs. δ extracted from independent measurements with Stern-Gerlach time of flight imaging (see inset). Black dashed line: theory prediction for the polarization vs. detuning. Error bars: standard deviation from 5 independent measurements.

optical dipole trap (radial frequency $\omega_r/2\pi = 133(1)$ Hz). We finally image the gas *in situ* using the polarization phase contrast scheme presented in chapter 2 in the same configuration as it has been used in chapters 3 and 4. These measurements were performed with the imaging set-up after all the improvements described in chapter 1. We fit the column density images after expansion with an integrated 2D Thomas-Fermi profile $n(x,y) = n_0 \left[1 - (x/\sigma_x)^2 - (y/\sigma_y)^2\right]^{3/2}$ to extract the atom number $N = 2\pi n_0 \sigma_x \sigma_y/5$ and axial size σ_x of the cloud.

Fig. 5.8(a) shows the atom number measured vs. detuning. As it can be observed the atom number is reduced as soon as there is some fraction of atoms in the $|\downarrow\rangle$ state (see Fig. 5.7(a)). This is due to the effect of three-body losses in this state. Fig. 5.8(b) shows the axial size σ_x vs. detuning. We see that the size is greatly reduced close to resonance due to the modification of the interactions. Notice that, although the scattering length on the large negative detuning side is bigger than on the large positive detuning side (solid line Fig. 5.8), the size is not bigger. This is due to the reduction in atom number for negative detunings.

Since the scattering length a_{--} is related with the axial size and atom number of the BEC we can infer a_{--} from the expansion measurements. In the Thomas-Fermi regime $a_{--} \propto \sigma_x^5/N$ [112] (see section 2.3.4). Although this approximation is not strictly valid for all our experimental parameters, we have verified by numerical solution of the time-dependent Gross-Pitaevskii equation (GPE) that estimating a_{--} through this scaling law results in errors below our experimental uncertainties.

Figure 5.8(c) shows our determination of a_{--} for various detunings (circles), corresponding to different values of the polarization parameter P (squares). We determine the latter by Stern-Gerlach separation of the bare states during time-of-flight expansion, from which we extract $P = (N_\uparrow - N_\downarrow)/(N_\uparrow + N_\downarrow)$. In order to correct for systematic errors in the measurement and compare the results to the scattering length a_{--}, we have scaled σ_x^5/N to yield $a_{\uparrow\uparrow}$ at large positive δ. Whereas for large positive (negative) values of δ the effective scattering length should approach $a_{\uparrow\uparrow}$ ($a_{\downarrow\downarrow}$), we expect a minimum at $\delta/2\pi = 6.5$ kHz ($P = 0.31$) due to the attractive character of the inter-state interactions $a_{\uparrow\downarrow} < 0$ as seen from equation (5.2.36). This is in good agreement with the experimental measurements. The data at large negative δ are in fair agreement with the limit

$a_{\downarrow\downarrow}$. At large negative detunings the data suffers from larger uncertainties due to residual breathing excitations induced by the detuning ramp, which is associated to large changes of a_{--}, and the larger three-body recombination rate of state $|\downarrow\rangle$ [30], see Fig. 5.10(a).

An analogous numerical experiment has been performed by solving an effective single component time-dependent GPE for all detunings using the MATLAB toolbox of ref. [144], where we have included the scattering length corresponding to the $|-\rangle$ state. After the BEC has expanded in the waveguide for 21 ms, we integrate the 3D density profile through the line of sight and fit it with the 2D Thomas-Fermi profile as we do with the experimental data. From the atom number and the fitted axial size we extract σ_x^5/N and rescale it to yield $a_{\uparrow\uparrow}$ at large positive δ, see brown diamonds in Fig. 5.8(c). The numerical experiment shows a very good agreement on the positive detuning side. For detunings close to resonance, a_{--} evaluated from σ_x^5/N is underestimated by $\sim 2a_0$ and for large negative detunings it is underestimated by $\sim 15\%$ (diamonds). This discrepancies come from the deviation from the Thomas-Fermi approximation for small scattering lengths and small atom numbers. Nevertheless the observed discrepancies are below our experimental uncertainty. Therefore, for simplicity we decided to scale σ_x^5/N in the plot from Fig. 5.10(c) for the complete range of explored detunings.

In conclusion, this method provides tunability of a_{--} by more than $100\,a_0$ without introducing additional loss mechanisms.

Inelastic scattering

Next, we consider the scattering properties of the higher dressed state $|+\rangle$. There, besides elastic collisions, two-body inelastic collisions leading to a change of the two-particle dressed state are also allowed, see section 5.2.2. For our typical experimental parameters they limit the lifetime of the BEC to ~ 1 ms, see Fig. 5.10(b). Fig. 5.9(a) sketches the two possible inelastic processes: ① $|++\rangle \rightarrow |--\rangle$ and ② $|++\rangle \rightarrow (|+-\rangle + |-+\rangle)/\sqrt{2}$. Both lead to the creation of correlated atom pairs with opposite momenta. They are accompanied by an energy release of either $\hbar\tilde{\Omega}$ or $\hbar\tilde{\Omega}/2$ per atom, corresponding to the energy gap between the two-particle dressed states. Similar processes occur in Raman-coupled BECs [59].
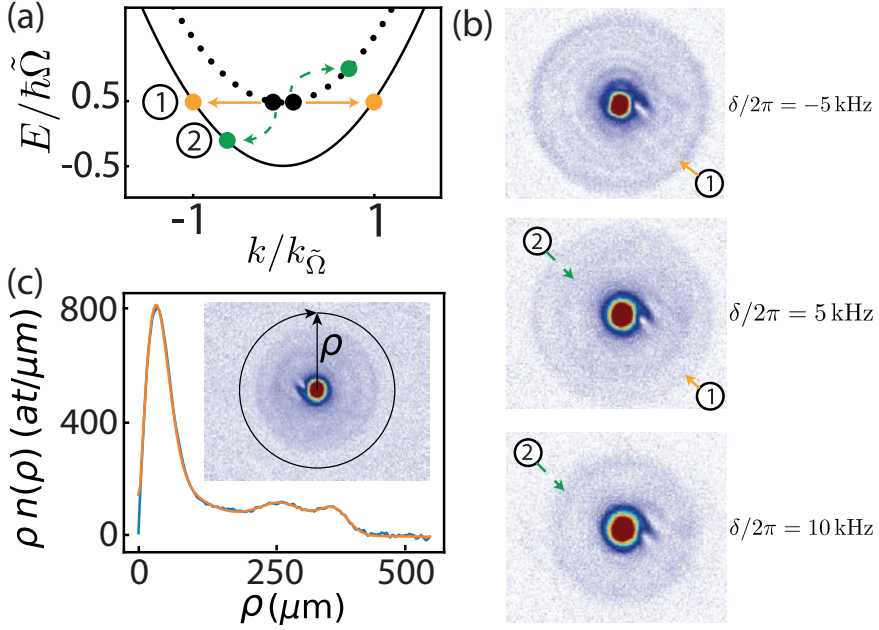
Figure 5.9: Inelastic decay of the higher dressed state. (a) Sketch of possible dressed state changing collisions ① : $|++\rangle \to |--\rangle$ (orange, solid arrows) and ② : $|++\rangle \to (|+-\rangle + |-+\rangle)/\sqrt{2}$ (green, dashed arrows). Energy E and momentum k are expressed in terms of $\tilde{\Omega} = \sqrt{\Omega^2 + \delta^2}$ and $k_{\tilde{\Omega}} = \sqrt{2m\tilde{\Omega}/\hbar}$, respectively. (b) Measured momentum distribution of the collision products showing the non-scattered BEC in the center and scattered atoms in a Halo corresponding to the different ① and ② processes. Images correspond to the average of 10 independent measurements. The likelihood of processes ① and ② depends on δ. (c) We plot the integrated linear density $\rho n_{sc}(\rho)$ on a shell with differential radius $d\rho$ of the Halo images (inset) vs. the radius of the integration shell ρ. Besides the central peak corresponding to the BEC, we can distinguish additional two peaks. From the largest to the smallest shell, they correspond to the decay of the processes ① and ②. We model the halo by a spherical shell with a Gaussian profile centered around the BEC and extract its parameters by fitting the time-of-flight images with its forward Abel transform.

To reveal these dressed-state changing collisions, we prepare rapidly (ramp rate 500 kHz/ms) a pure sample of $|+\rangle$ atoms. We then immediately switch off the trap and let the gas expand for a time $t_{\exp}$. During the first 1 ms the rf-field is kept on. As depicted in Fig. 5.9(b), the time-of-flight images reveal the presence of halos of atoms expanding away from the condensate. Since atoms in a BEC scatter with extremely low relative momenta, the halo radius R_H at time $t_{\exp}$ directly reflects the velocity of the collision products $v_f = R_H/t_{\exp}$. Processes ① and ② can be distinguished because the velocities are given by $\sqrt{2\hbar\tilde{\Omega}/m}$ and $\sqrt{\hbar\tilde{\Omega}/m}$, respectively. Here m is the mass of ^{39}K. Experimentally, we observe that the likelihood of the two processes depends on the dressed state composition, and therefore on δ.

We model the density of the ejected atoms as a spherical shell $n_{\rm sc}(r)$ with a Gaussian profile and centered around the condensate

$$n_{\rm sc}(r) = A \exp\left\{\left[-\frac{(r - R_H)^2}{2\sigma_H^2}\right]\right\},\qquad(5.3.1)$$

where $r = \sqrt{x^2 + y^2 + z^2}$. An absorption image of the atoms yields the integral of the density along the z cartesian axes and, since we have assumed a function with radial symmetry, this is equivalent to an Abel transform [195–198] . Therefore, to extract information from the scattered halos we make two-dimensional fits to absorption images with the forward Abel transform of Eq. (5.3.1) plus a Gaussian function which represents the unscattered atoms. We weight the fits with the radial coordinate $\rho = \sqrt{x^2 + y^2}$ so that the atom number $N = \int \rho n_{\rm sc}(\rho)d\rho$ is measured properly, see Fig. 5.9(c).

Figures 5.10(a), (b) and (c) present a more systematic study of these inelastic processes as a function of the parameters of the coupling field. Figure 5.10(a) depicts the velocity of the atoms in each halo vs. $\tilde{\Omega}$, determined by measuring R_H for different values of $t_{\exp}$. Figure 5.10(b) shows the measured halo radius as a function of δ. In both figures, circles (squares) correspond to process ① (process ②). The measurements are in excellent agreement with the theoretical predictions without any fitting parameters (solid and dashed lines).
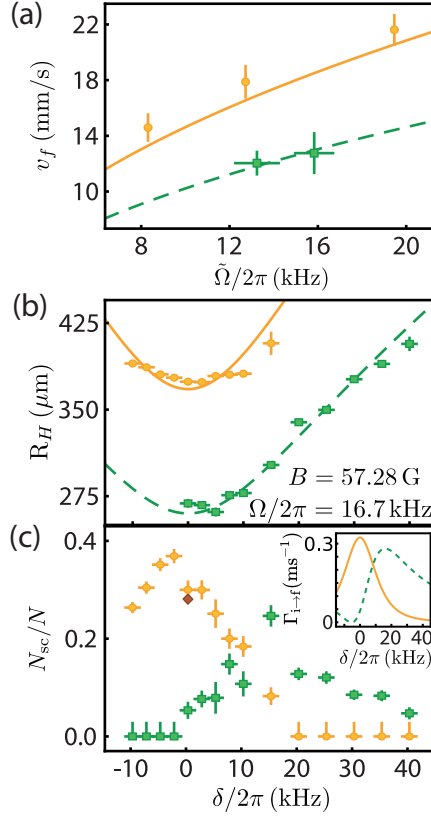
Figure 5.10: Inelastic decay of the higher dressed state. (a) Velocity of the scattered atoms v_f vs. $\tilde{\Omega}$. (b), (c) Radius of the halos R_H for an expansion time $t_{\exp} = 20.1$ ms and fraction of scattered atoms N_{sc}/N vs. δ. Theoretical prediction in brown. Inset: $\Gamma_{i \to f}$ vs. δ considering $n_i = 1.3 \cdot 10^{20} \mathrm{m}^{-3}$. In (a), (b) and (c) and orange circles (green squares) correspond to process ① (②) indicated in Fig. 5.9. Lines: theory predictions. Error bars: fit error (vertical) and uncertainty of δ and Ω (horizontal).

The scattering cross section of the two processes strongly depend on detuning. This can be clearly seen in Fig. 5.10(c), where we plot the fraction of atoms scattered N_{sc}/N in each halo as a function of δ extracted from the same set of images as Fig. 5.10(b). As described in section 5.2.3 the loss rate equation which

describes the scattering processes is given by Eq. (5.2.40). The scattering cross sections corresponding to the decay of the ① and ② process correspond to the Eq. (5.2.41) and (5.2.42) respectively. As seen in Fig. 5.10 (c), the measured N_{sc}/N agrees qualitatively with the line shapes of both $\Gamma_{i \to f_1, f_2}$. To estimate the scattered fraction we should take into account the density reduction during the 1 ms expansion in time of flight. In general, the density decay due to the expansion dynamics and inelastic collisions cannot be decoupled. However, on resonance the expansion and scattering timescales are very different and we can easily estimate the $|++\rangle \to |--\rangle$ scattered fraction neglecting the expansion. We obtain a good agreement with the experimental data, see Fig. 5.10.

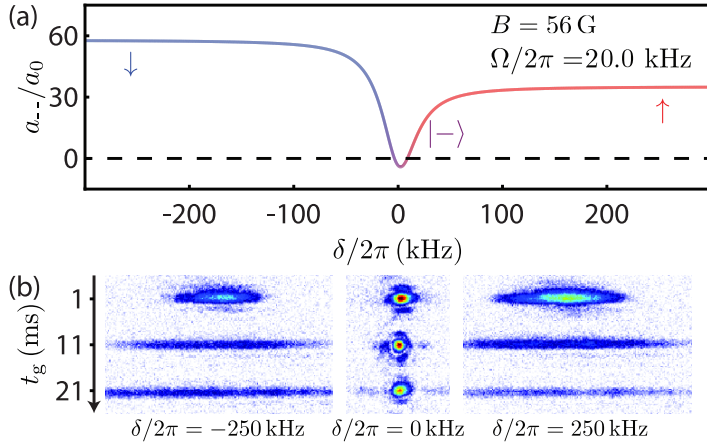### 5.3.3   Dressed-state bright solitons

Adiabatic preparation

Figure 5.11: Formation of a dressed-state bright soliton. (a) a_{--} vs. δ. Near zero detuning $a_{--} < 0$. (b) *In situ* dynamics of the gas after an evolution time t_{g} in the optical waveguide. For $\delta/2\pi = 0$ ($a_{--}/a_0 = -3.5$) we observe the formation of a self-bound bright soliton, whereas for $\delta/2\pi = \pm 250$ kHz interactions are repulsive and the gas expands.

After demonstration of the different collisional couplings present in dressed BECs, we refocus on the lower dressed state $|-\rangle$ and exploit the broad tun-

ability of its effective scattering length to explore attractively interacting systems. In optical waveguides, this situation enables the study of bright solitons: matter-wave packets that propagate without changing their shape because attractive non-linearities balance the effect of dispersion along the unconfined direction. In chapter 4, we have shown that two-component incoherent mixtures with residual mean field attraction can also form bright solitons in quasi-1D. In coherently-coupled systems, these solitons are formed by dressed atoms: we call them dressed-state bright solitons. As usual, they are only stable while the gas is effectively one dimensional, with an interaction energy that remains below $\hbar\omega_r$ [46–48].

To observe this new type of bright soliton, we study the dynamics of a BEC in state $|-\rangle$ after release in an optical waveguide. The magnetic field is set to $B = 56.000(2)$ G, where $a_{\uparrow\uparrow}/a_0 = 35.1$, $a_{\downarrow\downarrow}/a_0 = 57.9$, $a_{\uparrow\downarrow}/a_0 = -53.5$, and a_{--} can take negative values, see Fig. 5.11(a). We adiabatically prepare the system at different detunings (ramp rate 1 kHz/ms). For $a_{--} < 0$ we keep the initial atom number below $N \sim 3000$ to avoid collapse. To prepare such small samples, we start with a BEC in state $|\downarrow\rangle$ and exploit its large three-body recombination rate to reduce the atom number, as it was done in the experiments from chapter 4 [30]. We then remove the axial confinement in 15 ms, allowing for free evolution in a waveguide. Fig. 5.11(b) shows *in situ* images of the gas taken after an evolution time t_g. Whereas for $\delta/2\pi = \pm 250$ kHz the gas expands, as expected for a repulsive BEC in states $|\uparrow\rangle$ or $|\downarrow\rangle$, for $\delta = 0$ its shape remains unchanged. Here $a_{--}/a_0 = -3.5$ and we observe the adiabatic formation of a single dressed-state bright soliton.

Quench of the interactions

In the last series of experiments, we explore the response of the system to a quench of the effective scattering length from repulsive to attractive values. As demonstrated in recent experiments [191, 192], this triggers a modulational instability in the BEC: a mechanical instability where fluctuations in the condensate density are exponentially enhanced by the attractive non-linearity. Consequently, the gas splits into several equally spaced components. The growth of the density modulation is dominated by the most unstable Bogoliubov modes, which have

characteristic momentum $k_{\mathrm{MI}} \sim 1/\xi$. Here $\xi = a_{\mathrm{ho}}/\sqrt{4\,|a_{--}|\,n_{1\mathrm{D}}}$ is the healing length of the BEC in the waveguide, $a_{\mathrm{ho}} = \sqrt{\hbar/m\omega_r}$ the radial harmonic oscillator length, and $n_{1\mathrm{D}}$ the line density of the system before the quench. The characteristic length and time scales of this process are $\lambda = 2\pi/k_{\mathrm{MI}}$ and $\tau_{\mathrm{MI}} = 2m/\hbar k_{\mathrm{MI}}^2$, respectively. For $t > \tau_{\mathrm{MI}}$, each of the components evolves into a bright soliton, forming a soliton train [36, 199–202]. For a system of size L at the moment of the quench, the average number of solitons is expected to be $N_S = L/\lambda$ from simple length scale arguments [191, 192, 200].
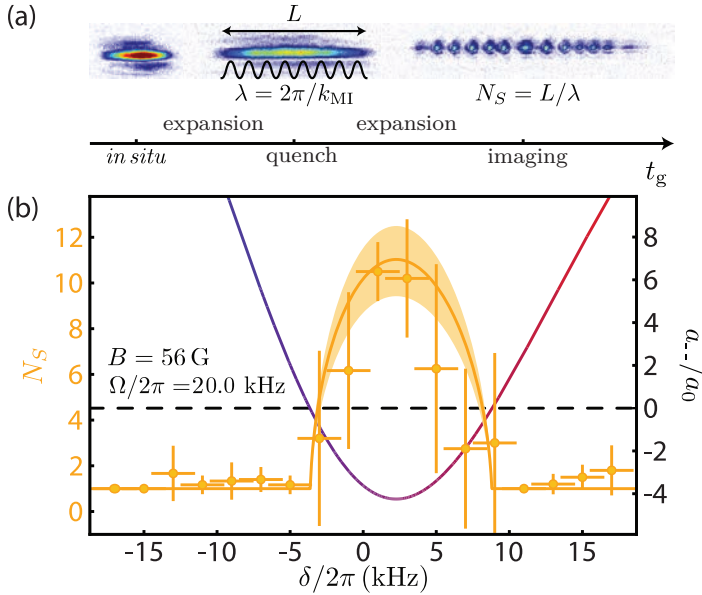

Figure 5.12: Modulational instability and formation of bright soliton trains. (a) Sketch of the experimental sequence and exemplary *in situ* images. (b) Number of components observed per image N_S vs. δ after the quench (orange circles). Error bars: standard deviation of 4 to 6 independent measurements (vertical) and uncertainty of δ (horizontal). Orange line, left axis: theory prediction $N_S = L/\lambda$ (shaded area: uncertainty due to the systematic error in the atom number). Colored line, right axis: a_{--} (colorscale: value of P).

Our experimental sequence is summarized in Fig. 5.12(a). The starting point of the experiment is a BEC of $65(15) \times 10^3$ atoms confined in a crossed optical

dipole trap[3]. At $t = 0$ we switch off the axial confinement and let the atoms expand in the waveguide (radial frequency $\omega_r/2\pi = 188(1)$ Hz) for $t_g = 11$ ms, reaching a size $L \sim 112\,\mu$m. At this point, we abruptly change δ (ramp rate 1 kHz/μs), effectively quenching the scattering length from $35.1\,a_0$ to its final value. An additional expansion time of 10 ms allows the development of the modulational instability and the formation of a soliton train[4], after which we image the cloud *in situ*.

Figure 5.12(b) shows the average number of components observed per image N_S as a function of the final detuning. We determine the number of components with an algorithm similar to the one presented in reference [192]. This algorithm was implemented by C. S. Chisholm and counts the number of morphological components in the image. To do so it applies a filter to remove noise and sets a boundary on the 45% of the maximum pixel count to binarize the image[5]. Then the algorithm counts the number of morphological domains[6]. Whereas the initial BEC has $N_S = 1$, for all values of δ such that $a_{--} < 0$ we measure $N_S > 1$. The maximum number of solitons in a train is observed at $\delta/2\pi = 2.3$ kHz, which corresponds to the most attractive value of a_{--}. Compared to previous experiments, where interactions were controlled using a magnetic Feshbach resonance [191, 192], our dressed state approach enables ramp rates orders of magnitude faster[7]. This ensures a clear separation of timescales between the duration of the ramp and τ_{MI}, and allows us to perform experiments at more attractive interaction strengths. Interestingly, our measurements show that the prediction $N_S = L/\lambda$ remains valid down to $a_{--}/a_0 = -4.2$ (solid line).

5.4   Conclusions and outlook

In conclusion, we have demonstrated fast temporal control of the collisional properties of rf-coupled ^{39}K BECs. In the attractive regime, we have observed the

---

[3]The initial trap frequencies are $(\omega_x, \omega_y, \omega_z)/2\pi = (26(1), 190(1), 188(1))$ Hz.

[4]Empirically, this is a good compromise between $\tau_{MI} \sim 5$ ms and the reduction of atom number at long times due to three-body recombination.

[5]All pixels below (above) 45% of the pixel count are 0(1).

[6]We set a threshold on the domain size. Domains below 8 pixels are not taken into account.

[7]We employ peak ramp rates $-5 \times 10^4\,a_0$/ms vs. $\sim -6\,a_0$/ms in Ref. [191].

formation of dressed-state bright solitons, and studied how the modulational instability triggered by an interaction quench develops into a bright soliton train.

In future experiments, we could exploit dressed-state changing collisions as a new source of correlated atom pairs [61–64]. Another interesting direction would be to implement the coherent coupling using instead optical Raman transitions. This would not only provide spatial control of the effective scattering length, but also allow engineering of higher partial wave collisions with tunable scattering amplitude [59]. Concerning attractive non-linear systems, we could exploit the ability to perform fast interaction quenches to study soliton excitations and breathers [149].

Moreover, in the weak coupling limit, we could study the Josephson effect with mutual attraction [203]. In this regime, the detuning of the coupling field with respect to the transition becomes density dependent for unequal intra-component interaction strengths due to their differential mean field shift. Moreover, in a similar fashion as explained in 3 and 4, we could tune the modified two-body dressed state interaction strength close to zero to reveal additional corrections to the energy of the system. Indeed, an effective three-body non-linearity has been predicted in rf-coupled BECs [171], which becomes important for smaller values of the Rabi coupling. They are expected to be attractive when arising from differential mean-field shifts, and repulsive when stemming from quantum fluctuations, stabilizing new types of quantum droplets [172, 204]. However, this experiments are very challenging in 3D due to the magnetic field sensitivity of the interaction strength which would smear out the measurement of small corrections to the energy. Instead, this experiments could be performed either in 2D or 1D, where the three-body non-linearities are more relevant and less prone to magnetic field noise [171].

Finally, due to their lack of Galilean invariance, spin-orbit coupled two-component BECs with unequal interactions should enable the observation of chiral bright solitons due to the momentum dependent differential mean field shifts [205].

Conclusions and Outlook

Summary of my thesis

In conclusion, during my thesis I have participated on the development of an experimental sequence to produce Bose-Einstein condensates of ^{39}K and a new two-component Bose-Einstein condensate of ^{39}K-^{41}K. In this period, I have upgraded the existing experimental apparatus with two major contributions.

On the one hand, I have implemented a glass cell 2D MOT which has a steady vapor pressure of $\sim 2 \times 10^{-7}$ mbar with an oven temperature below $50°$C, and with the only pumping of the NEG pump through the differential pumping tube. This cell has been operating successfully since its installation and allows us to produce atomic beams to load 10^9 and 7×10^7 atoms of ^{41}K and ^{39}K in the MOT, it could be used in the future to install a source of enriched ^{40}K, which would allow us to study Bose-Fermi mixtures in a system with small differential gravitational sag.

On the other hand, I have developed a custom-made optical system which is able to image atoms and generate optical potentials with high resolution. To improve the performance of our imaging system, we have corrected the main aberrations of our optical system: the large astigmatism introduced by our vacuum view-ports. By doing so, we have been able to measure bright solitons with a size of $3\,\mu$m and measure the point spread function of the complete optical system to be close to the $1.1\,\mu$m diffraction limit of the optical resolution. Hence, our optical system shows state of the art performance with a simplified design as compared to other custom made and commercial objectives. Moreover, this

set-up could allow us to project potentials on the atoms together with a DMD. A DMD set-up has been prepared by I. Urtiaga [89], A. Muñoz de las Heras [90] and D. Allepuz[86] to be installed in the main experiment. In particular, I have supervised the work of D. Allepuz on the holographic creation of arbitrary potentials for Bose-Einstein condensates with digital micromirror devices. In the future, we could install the DMD set-up in the main experiment and use it together with the microscope to perform different experiments. For instance, we could generate boxes and study homogeneous systems [206–209], perform Bragg spectroscopy in order to measure the dispersion relation of interacting Bose-Bose gases (in a similar fashion as performed for dipolar systems [210]) and produce moving lattices to prove the superfluidity of droplets.

Using the high resolution optical set-up, I have implemented a polarization phase contrast technique to measure the column density of optically dense atomic two-component BECs *in situ* at intermediate and high magnetic fields in open transitions. To use this technique, I have developed a direct method to observe the polarization phase shift introduced by the atoms in order to calibrate the effective Faraday coefficients, finding a good agreement with our theoretical predictions. This technique is flexible enough to measure the total column density of an atomic cloud as well as to measure the difference in column densities. Although the measurement of the difference remains challenging, the technique could be either combined with scalar phase contrast or highly saturated absorption imaging in order to probe both the total atom number and composition of the cloud. This method presents an advantage over other techniques which include a sequence to switch off the magnetic fields. Hence, we avoid any dynamical effect which may occur during this process due to the change of the interactions and observe the real distribution of the cloud without additional distortions.

These experimental upgrades, have allowed us to study the physics of two-component Bose-Einstein condensates with repulsive intra-component and attractive inter-component interactions. This system has allowed me to study different phases which arise with competing interactions with the help of the imaging set-up which I have developed.

In a first experiment, we have observed for the first time the stabilization of incoherent composite quantum droplets stabilized by beyond mean field effects

in a system with weak attractive interactions. By performing the experiments in a blue detuned lattice, we have been able to maintain the droplets in the depth of focus of the objective and provide a weak anti-confinement in order to forbid the stabilization of bright solitons in our set-up. Moreover, we have characterized the liquid to gas phase transition which occurs for low enough atom numbers obtaining a qualitative agreement with the theory. The mismatch with the theoretical predictions from reference [28] cannot be explained neither by a failure of the local density approximation nor by crossover effects towards reduced dimensions [147]. Preliminary indications from Monte Carlo calculations from the Boronat group indicate that large effective range of the mixture can play an important role in the stabilization of quantum liquid droplets. Future experimental work will be needed in order to understand the physical reasons behind the mismatch. Although, the lifetime of composite droplets limits further experiments in 3D with these states, our work opens the door to study quantum liquid droplets in reduced dimensions [123, 147].

During the completion of this thesis, other type of quantum droplets have been observed in dipolar condensates [32, 34]. Whereas dipolar droplets are anisotropic, and their description relays on the detailed modelization of the dipole-dipole interactions, composite quantum droplets allow for the study of isotropic quantum liquids with well-known interaction properties. Hence, they are promising to observe energy contributions beyond the LHY approximation.

In a second experiment, we have studied the interplay between incoherent quantum droplets and bright solitons in a quasi-1D geometry. We have measured the composition of the solitons and characterized the crossover and transition between both self-bound states. This study shows the analogy between quantum droplets and higher order non-linear solitons, such as the cubic-quintic non-linear solitons [45].

Finally, we have implemented a technique to modify the effective interactions in the presence of coherent coupling with a composite system with very unequal interactions. We have performed direct measurements of the modification of the elastic and inelastic interactions in the strong coupling limit. As compared to other atomic species with very similar intra and inter-state scattering lengths, ^{39}K offers a wider flexibility. Consequently, our system has allowed us to observe

bright solitons formed by dressed states in a quasi-1D geometry and study the modulational instability which occurs after quenching the interactions to the attractive regime. Moreover, the study of this system could be extended in the future on the weakly interacting limit in reduced dimensions in order to observe effective three-body interactions stemming from the differential mean field shift caused due to the very unequal intra-component interactions [171, 204].

Future perspectives

In chapter 5, we have studied a Bose-Einstein condensate formed by two-components which are coherently coupled with a radiofrequency field. However, the rf-coupling is homogeneous over the cloud. Instead, we could implement coherent coupling with two-photon Raman transitions. This can be realized by using two beams with frequencies ω_L and $\omega_L - \Delta\omega$ which are used to coherently couple two states, $|\uparrow\rangle$ and $|\downarrow\rangle$, with an energy splitting of $\hbar\omega_0$ via two photon transitions through a virtual state, see Fig. 5.13 (a). Hence, we could produce a spatially dependent coupling. When the two beams are co-propagating the situation is analogous to the rf-coupled system described in chapter 5. Hence, the interactions can be spatially modulated in a similar fashion as performed with optical Feshbach resonances [180, 182].

When the two beams are counter-propagating two-photon transitions result in a kick of momentum $\pm 2k_L$ depending on the initial state. Therefore, there is a coupling between the internal and external degrees of freedom, the so called spin-orbit coupling. Pioneering experiments on spin-orbit coupling were performed by the Spielman group [58]. The dispersion relation of a spin-orbit coupled system presents an avoided crossing between two parabolic dispersion relations of the bare states which are shifted by $2k_L$. The energy of the Raman coupled ground state is plotted in Fig. 5.13(b) and has been measured in references [212–214]. For Raman coupling energies $\hbar\Omega_R$ above $4E_L$, the dispersion relation of the Raman coupled ground state is described by $(p - p_{\min}(\delta))^2/2m^*$. The minimum of the dispersion relation is found at $p_{\min}$, which depends on the detuning, and m^* is the effective mass of the Raman coupled ground state. Hence, in this regime, neutral atoms behave in the same way as charged particles in a vector potential
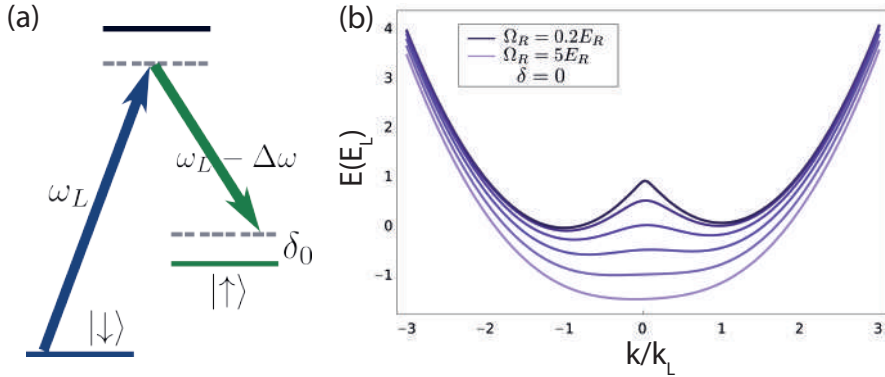
Figure 5.13: Figure taken from reference [211]. (a) A two-photon transition between the states $|\uparrow\rangle$ and $|\downarrow\rangle$ is performed with laser beams with frequencies ω_L and $\omega_L - \Delta\omega$. The energy splitting between the $|\uparrow\rangle$ and $|\downarrow\rangle$ is ω_0 and the detuning of the Raman coupling to the transition is $\delta = \Delta\omega - \omega_0$. (b) Dispersion relation of the Raman coupled ground state at resonance for different Raman coupling strengths Ω_R. Whereas for small couplings it displays two minima at $-k_L$ and k_L, for strong couplings it turns into a parabola. The energy and momentum are plotted in terms of the recoil energy and momentum.

A such that $p_{\min} = qA$, where q corresponds to an effective charge.

So far, this has allowed the observation of static gauge fields which can be externally controlled by the coupling field. In all these experiments, the systems have similar intra-component interactions $a_{\uparrow\uparrow} \approx a_{\downarrow\downarrow}$. However, as it was shown in reference [205], if $a_{\uparrow\uparrow} \neq a_{\downarrow\downarrow}$ there exists a differential mean field shift between both states. Therefore, the Raman coupling detuning, and consequently the vector potential $A = A^{(0)} + a_1 n(r)$, are density dependent, where $a_1 \propto (g_{\uparrow\uparrow} - g_{\downarrow\downarrow})$. In other words, it means that there is a back-action between the field and the matter. To understand this we can consider a time dependent variation of the density of the system. This would lead to the generation of an electric field $E = -\partial A/\partial t = -a_1 \partial n/\partial t$. At the same time, the system needs to satisfy the continuity equation $\partial n/\partial t + \vec{\nabla} \cdot \vec{j} = 0$, and thus a current $\vec{j}$ is generated which back acts on the atomic cloud. This can lead to the asymmetric expansion of the condensate, the existence of chiral solitons [205] and the coupling between the center of mass and breathing modes [215].

To date, this topic is the subject of current investigation in our team, as already described in the PhD thesis proposal from A. Frölian [211]. To perform this experiments we use a Raman laser system [216] which was developed by M. Ballu under my supervision. The experimental measurements have been mainly carried out by the PhD students A. Frölian and C. S. Chisholm, and the description of the results will be described in their thesis.

In conclusion, this shows that using two-component spin-orbit coupled ^{39}K BECs with unequal interactions also opens the door to perform quantum simulations of interacting gauge theories.

Appendix A

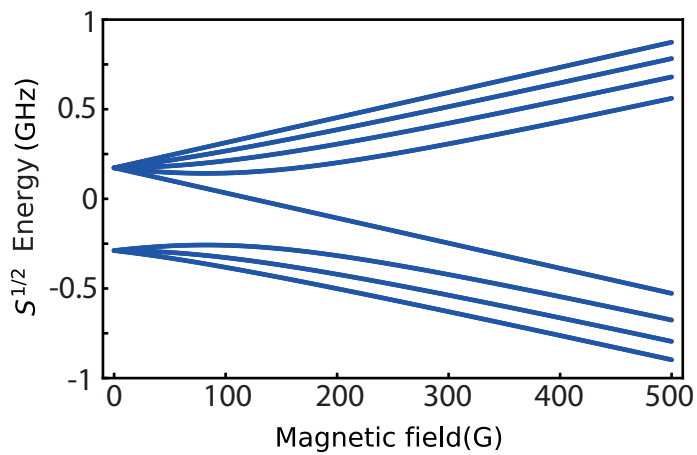# Energy spectrum vs. magnetic field

Figure A.1: Energy of the $^2S_{1/2}$ state of ^{39}K versus magnetic field. The zero of energy corresponds to the $^2S_{1/2}$ state fine structure energy.
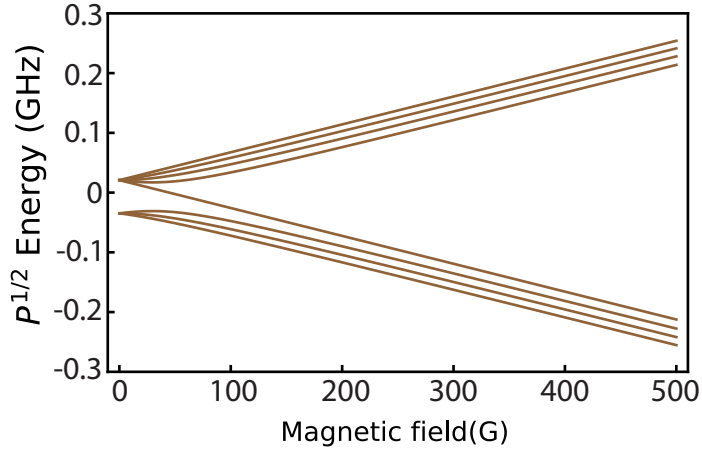
Figure A.2: Energy of the $^2P_{1/2}$ of ^{39}K state versus magnetic field. The energy is referenced with respect to the D1 transition.
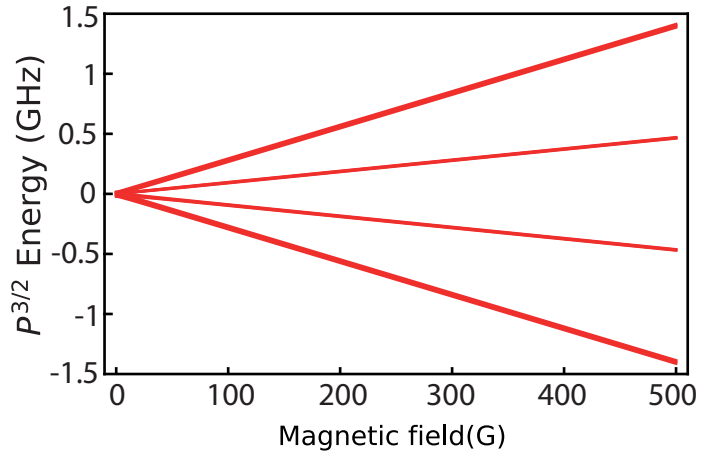

Figure A.3: Energy of the $^2P_{3/2}$ of ^{39}K state versus magnetic field. The energy is referenced with respect to the D2 transition.

Appendix B

Faraday laser detuning

The D2 master laser is used for absorption imaging of ^{39}K in time of flight on the $F = 2 \to F' = 3$ transition. To control the imaging frequency on the atoms, we tune the frequency Δ^{39}_{AOM} of a double pass acousto-optic modulator (AOM):

$$f^M_{\text{D2}} - 2\Delta^{39}_{\text{AOM}} = f_{2 \to 3'} \tag{B.0.1}$$

The D2 additional species laser is offset locked on the D2 master laser. The beat between these lasers is controlled with a VCO of frequency $\Delta^{\text{D2}}_{\text{BEAT}}$:

$$f^{39}_{\text{D2}} = f^M_{\text{D2}} - \Delta^{\text{D2}}_{\text{BEAT}} \tag{B.0.1}$$

The Faraday laser is offset locked on the D2 additional species laser. The beat between these lasers is controlled with a VCO of frequency $\Delta^{\text{FAR}}_{\text{BEAT}}$:

$$f_{\text{FAR}} = f^{39}_{\text{D2}} + \Delta^{\text{FAR}}_{\text{BEAT}} \tag{B.0.1}$$

The light that we use to image the atoms with the Polarization Phase contrast technique is switched on an off via an AOM with frequency $\Delta^{\text{FAR}}_{\text{AOM}}$:

$$f_{\text{ATOMS}} = f_{\text{FAR}} + \Delta^{\text{FAR}}_{\text{AOM}} \tag{B.0.1}$$

From these equations we get that:

$$f_{\text{ATOMS}} = f_{2\to3'} + 2\Delta_{\text{AOM}}^{39} - \Delta_{\text{BEAT}}^{D2} + \Delta_{\text{AOM}}^{\text{FAR}} - \Delta_{\text{BEAT}}^{\text{FAR}} \qquad \text{(B.0.1)}$$

where $\Delta_{\text{AOM}}^{39} = 102.2$ MHz, $\Delta_{\text{BEAT}}^{D2} = 245.2$ MHz and $\Delta_{\text{AOM}}^{\text{FAR}} = 81.8$ MHz.

To reference the frequency on the D2 transition at a particular magnetic field we use the following relation:

$$f_{2\to3'} = f_{\text{D2}} + \Delta_e - \Delta_g \qquad \text{(B.0.1)}$$

where Δ_e and Δ_g correspond to the excited and ground state shifts coming from the hyperfine splitting and the magnetic field contribution to the energy.

Appendix C

Technical details of polarization phase contrast imaging

We have performed several experimental tests to asses the validity of this technique and settle the optimum imaging parameters. In summary, we have decided to perform dark field phase contrast imaging with a 3 μs imaging pulse of 250 mW/cm^2 intensity and 1 MHz linewidth. The probe that we use for $B = 57$ G and $B = 396$ G is such that $\Delta_{\text{BEAT}}^{\text{FAR}} = 153$ MHz and $\Delta_{\text{BEAT}}^{\text{FAR}} = -515$ MHz respectively unless stated otherwise (see appendix B). In the following sections we describe the technical details that we have crosschecked to chose this experimental parameters.

Photon recoil blurring

The scattering of photons during the imaging pulse blurs the system we want to image, effectively reducing the imaging resolution. To estimate this effect we will assume that the transitions that we probe are closed. The scattering rate R is

given by:

$$R = \Gamma \rho_{\text{ee}}^{\text{st}} = \frac{\Gamma}{2} \frac{I/I_{\text{sat}}}{1 + (2\delta/\Gamma)^2 + I/I_{\text{sat}}} \tag{C.0.0}$$

where Γ is the natural linewidth of the transition, $\rho_{\text{ee}}^{\text{st}}$ is the steady-state population in the excited state and $I_{\text{sat}} = 1.75\,\text{mW/cm}^2$ is the saturation intensity for the D2 line. This estimate represents an upper bound on the real photon scattering because $\rho_{\text{ee}}^{\text{st}}$ will get reduced due to the decay of the atom to other states.

The root-mean square diffusion x_{rms} induced due to photon recoil is approximately given by:

$$x_{\text{rms}}(t) = \frac{1}{3} \sqrt{N_{\text{s}}(t)} v_{\text{rec}} t \tag{C.0.0}$$

where $N_{\text{s}}(t) = Rt$ is the number of photons scattered in a time t and $v_{\text{rec}} = \hbar k/m$ is the velocity of recoil [97]. For B = 57 G and $\Delta_{\text{BEAT}}^{\text{FAR}} = 153$ MHz $|b\rangle$ and $|c\rangle$ are red detuned by 17.5Γ and 12.2Γ from the closest transitions, leading to a $x_{\text{rms}} = 45$ nm and 33 nm far below our imaging resolution. The number of scattered photons is $N_{\text{s}} = 11.4$ and 6.2 respectively, and thus the imaging is destructive. Similarly, for B = 396 G and $\Delta_{\text{BEAT}}^{\text{FAR}} = -515$ MHz $|a\rangle$ and $|b\rangle$ are red detuned by 44.7Γ and 29.7Γ from the closest transitions, leading to a $x_{\text{rms}} = 20$ nm and 13 nm and $N_{\text{s}} = 2.3$ and 1 respectively.

Depumping

The transitions that we probe with this technique are not closed. Thus, atoms may fall into other states during the exposure. To observe this effect we measured the signal I_A for different exposure times at I = 250 mW/cm^2. As it can be seen in Fig. C.1, the signal saturates for increasing exposure times. We associate this to an optical depumping produced by the spontaneous emission of the excited states to other ground states. The characteristic time $\tau \sim 10\,\mu\text{s}$ of this process is very similar both for low field (B = 57 G, $\Delta_{\text{BEAT}}^{\text{FAR}} = 153(1)$ MHz for both states $|b\rangle$ and $|c\rangle$) and high field (B = 396 G, $\Delta_{\text{BEAT}}^{\text{FAR}} = -515(1)$ MHz for both states $|a\rangle$ and $|b\rangle$). We chose the exposure time[1] to be 3 μs , therefore 25% of the atoms decay are depumped from the transition. As a result, the calibrated

---

[1] Our experimental control program cannot deal with events shorter than 3 μs.

Faraday coefficient may differ from the theoretical expectation. Nevertheless, given that the optical depumping is a one-body process, we can calibrate the Faraday coefficient for a particular exposure time and still be able to measure the atom number properly.
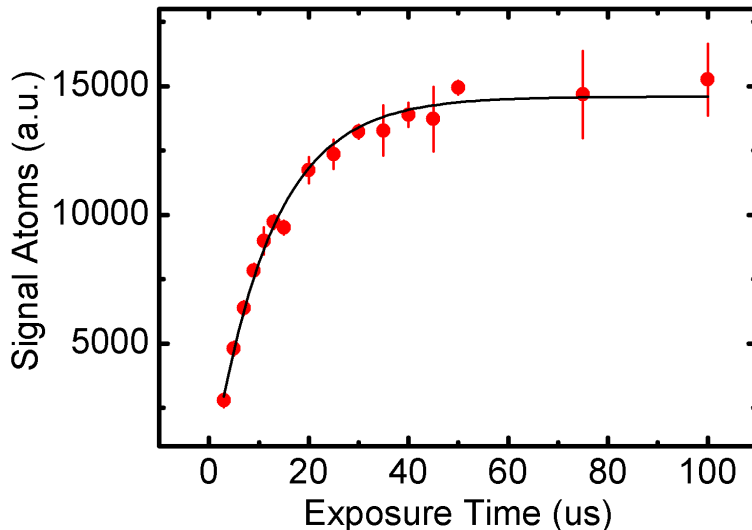

Figure C.1: Optical depumping. Red circles: Exemplary atomic signal I_A vs. exposure time for B = 396 G and $\Delta_{\text{BEAT}}^{\text{FAR}} = -515(1)MHz$ for state $|a\rangle$. Line: Phenomenological fit to $A(1 - e^{-t/\tau})$.

Linearity of signal vs. intensity

In the analysis of the phase contrast imaging we have assumed that the signal from the atomic cloud on the camera follows a linear relation with the intensity of light as expressed in equation (2.3.1a). Nevertheless, we need to use high intensities in order to have a reasonable signal with short exposure times and saturation effects could play a role. However, the imaging is performed far from resonance and thus the saturation is not really relevant. In order to prove that, we have exposed a BEC for $3\mu s$ for different intensities. Both for low field (B =

57 G, $\Delta^{\text{FAR}}_{\text{BEAT}} = 153(1)$ MHz) and high field (B = 396 G, $\Delta^{\text{FAR}}_{\text{BEAT}} = -515(1)$ MHz) we observed a linear relation with respect to the intensity. In the top panel of Fig. C.2, we show an exemplary measurement for high field far from resonance(B = 396 G, $\Delta^{\text{FAR}}_{\text{BEAT}} = -515(1)$ MHz). Instead if we perform the same measurement closer to resonance (B = 396 G, $\Delta^{\text{FAR}}_{\text{BEAT}} = -292(1)$ MHz) we observe that the signal saturates (bottom panel Fig. C.2).

Provided that the I_A depends on the intensity, the calibration relies on the intensity being constant. Stabilizing the intensity of a 3 μs imaging pulse is not a trivial task. We have crosschecked that the fluctuations of the peak pulse intensity are smaller than 5%.
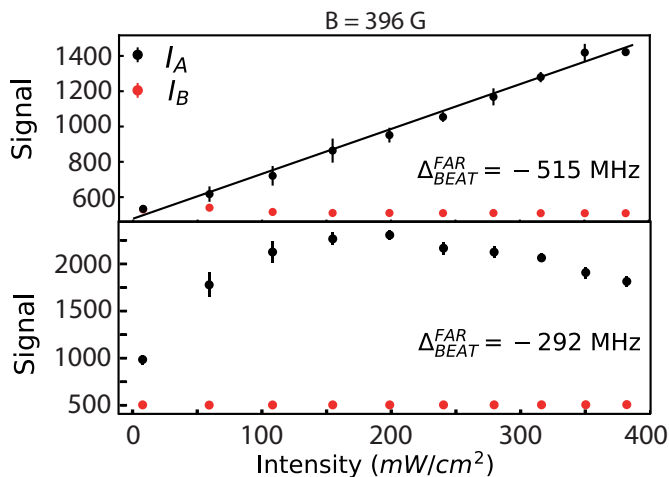

Figure C.2: I_A and I_B signals vs intensity measured at $B = 396$ G for state $|a\rangle$. The signal is taken as the average pixel count of a crop of $2.9 \, \mu$m $\times 2.9 \, \mu$m around the center of a BEC and has an offset of ~ 500 counts. Top panel: $\Delta^{\text{FAR}}_{\text{BEAT}} = -515$ MHz. The I_B signal at the smallest intensities shows the presence of atoms which have not been scattered. Bottom panel: $\Delta^{\text{FAR}}_{\text{BEAT}} = -292$ MHz.

Atomic lensing

Cold atomic clouds can act as a little lenses. In reference [98], a simple model is presented to evaluate the order of magnitude of this phenomenon. The atomic cloud is considered as a spherical ball of radius R with an index of refraction

given by the dilute media approximation as described in eq. (2.2.3). The focal length f of the atomic lens is given by:

$$f = \frac{2\pi R^2}{\theta_A^S \lambda},$$

(C.0.0)

where $\theta_A^S = 4\pi R(n-1)/\lambda$ is the scalar phase shift introduced by the atoms and λ is the imaging wavelength. This lens introduces a deflection angle θ_D:

$$\theta_D = R/f = \rho \alpha^S/\epsilon_0.$$

(C.0.0)

Therefore if θ_D was bigger than the collection angle ($\theta_C \approx 0.43$) of our imaging system, we would lose light and the effective resolution would be reduced. Instead, if $\theta_D < \theta_C$ we can just focus the imaging system accordingly to collect all the light. For typical imaging parameters we have that $\alpha_S/\epsilon_0 \sim 3 \cdot 10^{-22} m^3$. Assuming the biggest peak densities that we have experimentally observed $\rho \sim 10^{21} m^{-2}$ we would have a deflection angle $\theta_D \sim 0.15 < \theta_C$. Therefore our imaging resolution does not seem limited by atomic lensing.

Bibliography

[1] G. E. Moore. *Cramming more components onto integrated circuits.* Electronics **38** 114 (1965).

[2] P. A. Lee, N. Nagaosa, and X. G. Wen. *Doping a Mott insulator: Physics of high-temperature superconductivity.* Rev. Mod. Phys. **78** 17 (2006).

[3] O. Penrose and L. Onsager. *Bose-Einstein condensation and liquid Helium.* Phys. Rev. **104** 576 (1956).

[4] H. T. Diep. *Frustrated spin systems, 2nd edition.* World Scientific Publishing Co. (2013).

[5] N. K. Glendenning. *Compact stars : nuclear physics, particle physics, and general relativity.* Springer (2000).

[6] R. P. Feynman. *Simulating physics with computers.* Int. J. Theor. Phys. **21** 467 (1982).

[7] I. M. Georgescu, S. Ashhab, and F. Nori. *Quantum simulation.* Rev. Mod. Phys. **86** 153 (2014).

[8] W. D. Phillips. *Laser cooling and trapping of neutral atoms.* Rev. Mod. Phys. **70** 721 (1998).

[9] C. N. Cohen-Tannoudji. *Manipulating atoms with photons.* Rev. Mod. Phys. **70** 707 (1998).

[10] S. Chu. *The manipulation of neutral particles.* Rev. Mod. Phys. **70** 685 (1998).

[11] H. F. Hess. *Evaporative cooling of magnetically trapped and compressed spin-polarized Hydrogen.* Phys. Rev. B **34** 3476 (1986).

[12] K. B. Davis, M. O. Mewes, M. A. Joffe, M. R. Andrews, and W. Ketterle. *Evaporative cooling of Sodium atoms.* Phys. Rev. Lett. **74** 5202 (1995).

[13] M. H. Anderson, J. R. Ensher, M. R. Matthews, C. E. Wieman, and E. A. Cornell. *Observation of Bose-Einstein condensation in a dilute atomic vapor.* Science **269** 198 (1995).

[14] C. C. Bradley, C. A. Sackett, J. J. Tollett, and R. G. Hulet. *Evidence of Bose-Einstein condensation in an atomic gas with attractive interactions.* Phys. Rev. Lett. **75** 1687 (1995).

[15] B. DeMarco and D. S. Jin. *Onset of Fermi degeneracy in a trapped atomic gas.* Science **285** 1703 (1999).

[16] C. Chin, R. Grimm, P. Julienne, and E. Tiesinga. *Feshbach resonances in ultracold gases.* Rev. Mod. Phys. **82** 1225 (2010).

[17] M. Randeria, W. Zwerger, and M. Zwierlein. *The BCS-BEC crossover and the unitary Fermi gas.* Lect. Notes Phys. **836** 1 (2012).

[18] N. Navon, S. Piatecki, K. Günter, B. Rem, T. C. Nguyen, F. Chevy, W. Krauth, and C. Salomon. *Dynamics and thermodynamics of the low-temperature strongly interacting Bose gas.* Phys. Rev. Lett. **107** 135301 (2011).

[19] M. G. Hu, M. J. Van De Graaff, D. Kedar, J. P. Corson, E. A. Cornell, and D. S. Jin. *Bose polarons in the strongly interacting regime.* Phys. Rev. Lett. **117** 055301 (2016).

[20] N. B. Jørgensen, L. Wacker, K. T. Skalmstang, M. M. Parish, J. Levinsen, R. S. Christensen, G. M. Bruun, and J. J. Arlt. *Observation of attractive and repulsive polarons in a Bose-Einstein condensate.* Phys. Rev. Lett. **117** 055302 (2016).

[21] P. Makotyn, C. E. Klauss, D. L. Goldberger, E. A. Cornell, and D. S. Jin. *Universal dynamics of a degenerate unitary Bose gas.* Nat. Phys. **10** 116 (2014).

[22] R. J. Fletcher, R. Lopes, J. Man, N. Navon, R. P. Smith, M. W. Zwierlein, and Z. Hadzibabic. *Two- and three-body contacts in the unitary Bose gas.* Science **355** 377 (2017).

[23] B. S. Rem, A. T. Grier, I. Ferrier-Barbut, U. Eismann, T. Langen, N. Navon, L. Khaykovich, F. Werner, D. S. Petrov, F. Chevy, and C. Salomon. *Lifetime of the Bose gas with resonant interactions.* Phys. Rev. Lett. **110** 163202 (2013).

[24] R. J. Fletcher, A. L. Gaunt, N. Navon, R. P. Smith, and Z. Hadzibabic. *Stability of a unitary Bose gas.* Phys. Rev. Lett. **111** 125303 (2013).

[25] M. Greiner, O. Mandel, T. Esslinger, T. W. Hänsch, and I. Bloch. *Quantum phase transition from a superfluid to a Mott insulator in a gas of ultracold atoms.* Nature **415** 39 (2002).

[26] A. Mazurenko, C. S. Chiu, G. Ji, M. F. Parsons, M. Kanász-Nagy, R. Schmidt, F. Grusdt, E. Demler, D. Greif, and M. Greiner. *A cold-atom Fermi-Hubbard antiferromagnet.* Nature **545** 462 (2017).

[27] I. Bloch, J. Dalibard, and W. Zwerger. *Many-body physics with ultracold gases.* Rev. Mod. Phys. **80** 885 (2008).

[28] D. S. Petrov. *Quantum mechanical stabilization of a collapsing Bose-Bose mixture.* Phys. Rev. Lett. **115** 155302 (2015).

[29] C. R. Cabrera, L. Tanzi, J. Sanz, B. Naylor, P. Thomas, P. Cheiney, and L. Tarrue. *Quantum liquid droplets in a mixture of Bose-Einstein condensates.* Science **359** 301 (2018).

[30] P. Cheiney, C. R. Cabrera, J. Sanz, B. Naylor, L. Tanzi, and L. Tarruell. *Bright soliton to quantum droplet transition in a mixture of Bose-Einstein condensates.* Phys. Rev. Lett. **120** 135301 (2018).

[31] G. Semeghini, G. Ferioli, L. Masi, C. Mazzinghi, L. Wolswijk, F. Minardi, M. Modugno, G. Modugno, M. Inguscio, and M. Fattori. *Self-bound quantum droplets of atomic mixtures in free space.* Phys. Rev. Lett. **120** 235301 (2018).

[32] H. Kadau, M. Schmitt, M. Wenzel, C. Wink, T. Maier, I. Ferrier-Barbut, and T. Pfau. *Observing the Rosensweig instability of a quantum ferrofluid.* Nature **530** 194 (2016).

[33] M. Schmitt, M. Wenzel, F. Böttcher, I. Ferrier-Barbut, and T. Pfau. *Self-bound droplets of a dilute magnetic quantum liquid.* Nature **539** 259 (2016).

[34] L. Chomaz, S. Baier, D. Petter, M. J. Mark, F. Wächtler, L. Santos, and F. Ferlaino. *Quantum-fluctuation-driven crossover from a dilute Bose-Einstein condensate to a macrodroplet in a dipolar quantum fluid.* Phys. Rev. X **6** 041039 (2016).

[35] F. Böttcher, M. Wenzel, J.-N. Schmidt, M. Guo, T. Langen, I. Ferrier-Barbut, T. Pfau, R. Bombín, J. Sánchez-Baena, J. Boronat, and F. Mazzanti. *Dilute dipolar quantum droplets beyond the extended Gross-Pitaevskii equation.* Phys. Rev. Res. **1** 033088 (2019).

[36] K. E. Strecker, G. B. Partridge, A. G. Truscott, and R. G. Hulet. *Formation and propagation of matter-wave soliton trains.* Nature **417** 150 (2002).

[37] L. Khaykovich, F. Schreck, G. Ferrari, T. Bourdel, J. Cubizolles, L. D. Carr, Y. Castin, and C. Salomon. *Formation of a matter-wave bright soliton.* Science **296** 1290 (2002).

[38] P. Medley, M. A. Minar, N. C. Cizek, D. Berryrieser, and M. A. Kasevich. *Evaporative production of bright atomic solitons.* Phys. Rev. Lett. **112** 060401 (2014).

[39] S. L. Cornish, S. T. Thompson, and C. E. Wieman. *Formation of bright matter-wave solitons during the collapse of attractive Bose-Einstein condensates.* Phys. Rev. Lett. **96** 170401 (2006).

[40] A. L. Marchant, T. P. Billam, T. P. Wiles, M. M. Yu, S. A. Gardiner, and S. L. Cornish. *Controlled formation and reflection of a bright solitary matter-wave.* Nat. Commun. **4** 1865 (2013).

[41] G. D. McDonald, C. C. Kuhn, K. S. Hardman, S. Bennetts, P. J. Everitt, P. A. Altin, J. E. Debs, J. D. Close, and N. P. Robins. *Bright solitonic matter-wave interferometer.* Phys. Rev. Lett. **113** 013002 (2014).

[42] S. Lepoutre, L. Fouché, A. Boissé, G. Berthet, G. Salomon, A. Aspect, and T. Bourdel. *Production of strongly bound 39K bright solitons.* Phys. Rev. A **94** 053626 (2016).

[43] T. MeŽnaršič, T. Arh, J. Brence, J. Pišljar, K. Gosar, Ž. Gosar, R. Žitko, E. Zupanič, and P. Jeglič. *Cesium bright matter-wave solitons and soliton trains.* Phys. Rev. A **99** 033625 (2019).

[44] T. Dauxois and M. Peyrard. *Physics of solitons.* Cambridge University Press (2006).

[45] B. A. Malomed, D. Mihalache, F. Wise, and L. Torner. *Spatiotemporal optical solitons.* J. Opt. B **7** R53 (2005).

[46] V. M. Pérez-García, H. Michinel, and H. Herrero. *Bose-Einstein solitons in highly asymmetric traps.* Phys. Rev. A **57** 3837 (1998).

[47] L. Salasnich, A. Parola, and L. Reatto. *Condensate bright solitons under transverse confinement.* Phys. Rev. A **66** 7 (2002).

[48] L. D. Carr and Y. Castin. *Dynamics of a matter-wave bright soliton in an expulsive potential.* Phys. Rev. A **66** 636021 (2002).

[49] R. N. Bisset, R. M. Wilson, D. Baillie, and P. B. Blakie. *Ground-state phase diagram of a dipolar condensate with quantum fluctuations.* Phys. Rev. A **94** 033619 (2016).

[50] F. Wächtler and L. Santos. *Quantum filaments in dipolar Bose-Einstein condensates.* Phys. Rev. A **93** 061603(R) (2016).

[51] A. J. Moerdijk, B. J. Verhaar, and T. M. Nagtegaal. *Collisions of dressed ground-state atoms.* Phys. Rev. A **53** 4343 (1996).

[52] C. P. Search and P. R. Berman. *Manipulating the speed of sound in a two-component Bose-Einstein condensate.* Phys. Rev. A **63** 1 (2001).

[53] T. Zibold, E. Nicklas, C. Gross, and M. K. Oberthaler. *Classical bifurcation at the transition from rabi to Josephson dynamics.* Phys. Rev. Lett. **105** 204101 (2010).

[54] D. S. Hall, M. R. Matthews, J. R. Ensher, C. E. Wieman, and E. A. Cornell. *Dynamics of component separation in a binary mixture of Bose-Einstein condensates.* Phys. Rev. Lett. **81** 1539 (1998).

[55] E. Nicklas, H. Strobel, T. Zibold, C. Gross, B. A. Malomed, P. G. Kevrekidis, and M. K. Oberthaler. *Rabi flopping induces spatial demixing dynamics.* Phys. Rev. Lett. **107** 193001 (2011).

[56] E. Nicklas, M. Karl, M. Höfer, A. Johnson, W. Muessel, H. Strobel, J. Tomkovič, T. Gasenzer, and M. K. Oberthaler. *Observation of scaling in the dynamics of a strongly quenched quantum gas.* Phys. Rev. Lett. **115** 245301 (2015).

[57] K. Shibata, A. Torii, H. Shibayama, Y. Eto, H. Saito, and T. Hirano. *Interaction modulation in a long-lived Bose-Einstein condensate by rf coupling.* Phys. Rev. A **99** 013622 (2019).

[58] Y. J. Lin, K. Jiménez-García, and I. B. Spielman. *Spin-orbit-coupled Bose-Einstein condensates.* Nature **471** 83 (2011).

[59] R. A. Williams, L. J. LeBlanc, K. Jiménez-García, M. C. Beeler, A. R. Perry, W. D. Phillips, and I. B. Spielman. *Synthetic partial waves in ultracold atomic collisions.* Science **335** 314 (2012).

[60] R. A. Williams, M. C. Beeler, L. J. Leblanc, K. Jiménez-García, and I. B. Spielman. *Raman-induced interactions in a single-component fermi gas near an s-wave Feshbach resonance.* Phys. Rev. Lett. **111** 095301 (2013).

[61] M. Greiner, C. A. Regal, J. T. Stewart, and D. S. Jin. *Probing pair-correlated fermionic atoms through correlations in atom shot noise*. Phys. Rev. Lett. **94** 110401 (2005).

[62] A. Perrin, H. Chang, V. Krachmalnicoff, M. Schellekens, D. Boiron, A. Aspect, and C. I. Westbrook. *Observation of atom pairs in spontaneous four-wave mixing of two colliding Bose-Einstein condensates*. Phys. Rev. Lett. **99** 150405 (2007).

[63] B. Lücke, M. Scherer, J. Kruse, L. Pezzé, F. Deuretzbacher, P. Hyllus, O. Topic, J. Peise, W. Ertmer, J. Arlt, L. Santos, A. Smerzi, and C. Klempt. *Twin matter waves for interferometry beyond the classical limit*. Science **334** 773 (2011).

[64] R. Bücker, J. Grond, S. Manz, T. Berrada, T. Betz, C. Koller, U. Hohenester, T. Schumm, A. Perrin, and J. Schmiedmayer. *Twin-atom beams*. Nat. Phys. **7** 608 (2011).

[65] C. R. Cabrera. *Quantum liquid droplets in a mixture of Bose-Einstein condensates*. Ph.D. thesis, Institute of Photonic Sciences, Universitat Politècnica de Catalunya (2018).

[66] M. Inguscio and L. Fallani. *Atomic physics: precise measurements and ultracold matter*. Oxford University Press (2013).

[67] G. Modugno, G. Ferrari, G. Roati, R. J. Brecha, A. Simoni, and M. Inguscio. *Bose-Einstein condensation of potassium atoms by sympathetic cooling*. Science **294** 1320 (2001).

[68] G. Roati, F. Riboli, G. Modugno, and M. Inguscio. *Fermi-Bose quantum degenerate 40K - 87Rb mixture with attractive interaction*. Phys. Rev. Lett. **89** 150403 (2002).

[69] G. Roati, M. Zaccanti, C. D'Errico, J. Catani, M. Modugno, A. Simoni, M. Inguscio, and G. Modugno. *39K Bose-Einstein condensate with tunable interactions*. Phys. Rev. Lett. **99** 010403 (2007).

[70] T. Loftus, C. A. Regal, C. Ticknor, J. L. Bohn, and D. S. Jin. *Resonant control of elastic collisions in an optically trapped Fermi gas of atoms.* Phys. Rev. Lett. **88** 1732011 (2002).

[71] C. A. Regal, C. Ticknor, J. L. Bohn, and D. S. Jin. *Tuning p-wave interactions in an ultracold Fermi gas of atoms.* Phys. Rev. Lett. **90** 053201 (2003).

[72] C. D'Errico, M. Zaccanti, M. Fattori, G. Roati, M. Inguscio, G. Modugno, and A. Simoni. *Feshbach resonances in ultracold 39K.* New J. Phys. **9** 223 (2007).

[73] T. Kishimoto, J. Kobayashi, K. Noda, K. Aikawa, M. Ueda, and S. Inouye. *Direct evaporative cooling of 41K into a Bose-Einstein condensate.* Phys. Rev. A **79** 031602(R) (2009).

[74] C. H. Wu, I. Santiago, J. W. Park, P. Ahmadi, and M. W. Zwierlein. *Strongly interacting isotopic Bose-Fermi mixture immersed in a Fermi sea.* Phys. Rev. A **84** 011601(R) (2011).

[75] L. Tanzi, C. R. Cabrera, J. Sanz, P. Cheiney, M. Tomza, and L. Tarruell. *Feshbach resonances in potassium Bose-Bose mixtures.* Phys. Rev. A **98** 062712 (2018).

[76] M. Bosch. *An experimental setup for gray molasses sub-Doppler cooling of Potassium gases.* Master thesis, Institut de Ciències Fotòniques, Universitat Politècnica de Catalunya .

[77] P. Thomas. *Optical dipole potentials for multi-component Bose-Einstein condensates.* Master thesis, Institut de Ciències Fotòniques, Universitat Politècnica de Catalunya (2017).

[78] J. Catani, P. Maioli, L. De Sarlo, F. Minardi, and M. Inguscio. *Intense slow beams of bosonic Potassium isotopes.* Phys. Rev. A - At. Mol. Opt. Phys. **73** 033415 (2006).

[79] T. Uehlinger. *A 2D Magneto-optical trap as a high-flux source of cold Potassium atoms.* Master thesis, Swiss federal institute of technology Zurich ETH (2008).

[80] M. Landini. *A tunable Bose-Einstein condensate for quantum interferometry.* Ph.D. thesis, University of Trento (2011).

[81] M. Fattori. *Private communications* .

[82] T. Petelski. *Atom interferometers for precision gravity measurements.* Ph.D. thesis, University of Florence (2005).

[83] R. L. Campbell, R. P. Smith, N. Tammuz, S. Beattie, S. Moulder, and Z. Hadzibabic. *Efficient production of large 39K Bose-Einstein condensates.* Phys. Rev. A **82** 063611 (2010).

[84] L. Saemisch. *Development of an imaging system for a quantum gas experiment.* Erasmus internship, Institut de Ciències Fotòniques, Universitat Politècnica de Catalunya (2015).

[85] J. Sanz. *Development of a fluorescence imaging system for a quantum gas experiment.* Master thesis, Institut de Ciències Fotòniques, Universitat Politècnica de Catalunya (2015).

[86] D. Allepuz. *Holographic creation of arbitrary potentials for Bose-Einstein condensates with digital micromirror devices.* Bachelor thesis, Universitat de Barcelona (2019).

[87] P. L. Kapitza and P. A. Dirac. *The reflection of electrons from standing light waves.* Math. Proc. Cambridge Philos. Soc. **29** 297 (1933).

[88] C. J. Pethick and H. Smith. *Bose–Einstein condensation in dilute gases.* Cambridge University Press (2008).

[89] I. Urtiaga. *Generating arbitrary potentials with a digital micromirror device.* Internship report, Institut de Ciències Fotòniques (2016).

[90] A. M. de las Heras. *Generating arbitrary potentials for ultracold Bose gases with a digital micromirror device.* Internship report, Institut de Ciències Fotòniques (2017).

[91] P. Zupancic, P. M. Preiss, R. Ma, A. Lukin, M. Eric Tai, M. Rispoli, R. Islam, and M. Greiner. *Ultra-precise holographic beam shaping for microscopic quantum control.* Opt. Express **24** 13881 (2016).

[92] S. Kuhr. *Quantum-gas microscopes: A new tool for cold-atom quantum simulators.* Natl. Sci. Rev. **3** 170 (2016).

[93] J. Billy, V. Josse, Z. Zuo, A. Bernard, B. Hambrecht, P. Lugan, D. Clément, L. Sanchez-Palencia, P. Bouyer, and A. Aspect. *Direct observation of Anderson localization of matter waves in a controlled disorder.* Nature **453** 891 (2008).

[94] G. Reinaudi, T. Lahaye, Z. Wang, and D. Guéry-Odelin. *Strong saturation absorption imaging of dense clouds of ultracold atoms.* Opt. Lett. **32** 3143 (2007).

[95] T. Yefsah, R. Desbuquois, L. Chomaz, K. J. Günter, and J. Dalibard. *Exploring the thermodynamics of a two-dimensional Bose gas.* Phys. Rev. Lett. **107** 130401 (2011).

[96] K. Hueck, N. Luick, L. Sobirey, J. Siegl, T. Lompe, H. Moritz, L. W. Clark, and C. Chin. *Calibrating high intensity absorption imaging of ultracold atoms.* Opt. Express **25** 8670 (2017).

[97] M. A. Joffe, W. Ketterle, A. Martin, and D. E. Pritchard. *Transverse cooling and deflection of an atomic beam inside a Zeeman slower.* J. Opt. Soc. Am. B **10** 2257 (1993).

[98] M. R. Andrews, M.-O. Mewes, N. J. van Druten, D. S. Durfee, D. M. Kurn, and W. Ketterle. *Direct, Nondestructive Observation of a Bose Condensate.* Science **273** 84 (1996).

[99] J. K. . Stockton. *Continuous quantum measurement of cold alkali-atom spins.* Ph.D. thesis, California Institute of Technology (2007).

[100] M. Napolitano. *Interaction-based nonlinear quantum metrology with a cold atomic ensemble*. Ph.D. thesis, Institute of Photonic Sciences, Universitat Politècnica de Catalunya (2014).

[101] W. Ketterle, D. S. Durfee, and D. M. Stamper-Kurn. *Making, probing and understanding Bose-Einstein condensates*. arXiv:cond-mat/9904034 (1999).

[102] C. C. Bradley, C. A. Sackett, and R. G. Hulet. *Bose-Einstein condensation of Lithium: observation of limited condensate number*. Phys. Rev. Lett. **78** 985 (1997).

[103] M. Gajdacz, P. L. Pedersen, T. Mørch, A. J. Hilliard, J. Arlt, and J. F. Sherson. *Non-destructive Faraday imaging of dynamically controlled ultracold atoms*. Rev. Sci. Instrum. **84** 083105 (2013).

[104] H. A. Lorentz. *The theory of electrons and its applications to the phenomena of light and radiant heat*. Dover Publications (2003).

[105] C. J. Foot. *Atomic Phyics*. Oxford University Press (2004).

[106] T. G. Tiecke. *Feshbach resonances in ultracold mixtures of the fermionic quantum gases 6Li and 40K*. Ph.D. thesis, University of Amsterdam (2009).

[107] J. J. Sakurai and J. Napolitano. *Modern quantum mechanics*. Cambridge University Press (2017).

[108] L. J. LeBlanc. *Exploring many-body physics with ultracold atoms*. Ph.D. thesis, University of Toronto (2011).

[109] U. Schünemann, H. Engler, R. Grimm, M. Weidemüller, and M. Zielonkowski. *Simple scheme for tunable frequency offset locking of two lasers*. Rev. Sci. Instrum. **70** 242 (1999).

[110] R. Meppelink, R. A. Rozendaal, S. B. Koller, J. M. Vogels, and P. Van Der Straten. *Thermodynamics of Bose-Einstein-condensed clouds using phase-contrast imaging*. Phys. Rev. A **81** (2010).

[111] S. Giorgini, L. P. Pitaevskii, and S. Stringari. *Condensate fraction and critical temperature of a trapped interacting Bose gas.* Phys. Rev. A **54** R4633(R) (1996).

[112] Y. Castin and R. Dum. *Bose-Einstein condensates in time dependent traps.* Phys. Rev. Lett. **77** 5315 (1996).

[113] F. Dalfovo and S. Stringari. *Helium nanodroplets and trapped Bose-Einstein condensates as prototypes of finite quantum fluids.* J. Chem. Phys. **115** 10078 (2001).

[114] M. Barranco, R. Guardiola, S. Hernández, R. Mayol, J. Navarro, and M. Pi. *Helium nanodroplets: an overview* (2006).

[115] D. Baillie, R. M. Wilson, R. N. Bisset, and P. B. Blakie. *Self-bound dipolar droplet: a localized matter wave in free space.* Phys. Rev. A **94** 021602(R) (2016).

[116] F. Cinti, A. Cappellaro, L. Salasnich, and T. Macrì. *Superfluid filaments of dipolar bosons in free space.* Phys. Rev. Lett. **119** 215302 (2017).

[117] C. Staudinger, F. Mazzanti, and R. E. Zillich. *Self-bound Bose mixtures.* Phys. Rev. A **98** 023633 (2018).

[118] V. Cikojević, K. DŽelalija, P. Stipanović, L. Vranješ Markić, and J. Boronat. *Ultradilute quantum liquid drops.* Phys. Rev. B **97** 140502(R) (2018).

[119] F. Böttcher, J. N. Schmidt, M. Wenzel, J. Hertkorn, M. Guo, T. Langen, and T. Pfau. *Transient supersolid properties in an array of dipolar quantum droplets.* Phys. Rev. X **9** 011051 (2019).

[120] J. M. Gerton, D. Strekalov, I. Prodan, and R. G. Hulet. *Direct observation of growth and collapse of a Bose-Einstein condensate with attractive interactions.* Nature **408** 692 (2000).

[121] E. A. Donley, N. R. Claussen, S. L. Cornish, J. L. Roberts, E. A. Cornell, and C. E. Wieman. *Dynamics of collapsing and exploding Bose-Einstein condensates.* Nature **412** 295 (2001).

[122] T. D. Lee, K. Huang, and C. N. Yang. *Eigenvalues and eigenfunctions of a Bose system of hard spheres and its low-temperature properties.* Phys. Rev. Lett. **106** 1135 (1957).

[123] D. S. Petrov and G. E. Astrakharchik. *Ultradilute low-dimensional liquids.* Phys. Rev. Lett. **117** 100401 (2016).

[124] F. Wächtler and L. Santos. *Ground-state properties and elementary excitations of quantum droplets in dipolar Bose-Einstein condensates.* Phys. Rev. A **94** 033619 (2016).

[125] H. Kadau. *Rosensweig instability and droplets in a quantum ferrofluid of Dysprosium atoms.* Ph.D. thesis, University of Stuttgart (2016).

[126] A. Bulgac. *Dilute quantum droplets.* Phys. Rev. Lett. **89** 050402 (2002).

[127] I. Ferrier-Barbut, H. Kadau, M. Schmitt, M. Wenzel, and T. Pfau. *Observation of Quantum Droplets in a Strongly Dipolar Bose Gas.* Phys. Rev. Lett. **116** (2016).

[128] I. Ferrier-Barbut, M. Schmitt, M. Wenzel, H. Kadau, and T. Pfau. *Liquid quantum droplets of ultracold magnetic atoms.* J. Phys. B **49** 214004 (2016).

[129] M. Schmitt. *A self-bound dilue quantum liquid of Dysprosium atoms.* Ph.D. thesis, University of Stuttgart (2017).

[130] I. Ferrier-Barbut, M. Wenzel, M. Schmitt, F. Böttcher, and T. Pfau. *Onset of a modulational instability in trapped dipolar Bose-Einstein condensates.* Phys. Rev. A **97** 11604 (2018).

[131] Y. Tang, A. Sykes, N. Q. Burdick, J. L. Bohn, and B. L. Lev. *s-wave scattering lengths of the strongly dipolar bosons 162Dy and 164Dy.* Phys. Rev. A - At. Mol. Opt. Phys. **92** 022703 (2015).

[132] D. Baillie, R. M. Wilson, and P. B. Blakie. *Collective excitations of self-bound droplets of a dipolar quantum fluid.* Phys. Rev. Lett. **119** 255302 (2017).

[133] I. Ferrier-Barbut and T. Pfau. *Quantum liquids get thin: a mix of two bosonic particles develops attractive forces to create a quantum liquid.* Science **359** 274 (2018).

[134] L. Tanzi, E. Lucioni, F. Famà, J. Catani, A. Fioretti, C. Gabbanini, R. N. Bisset, L. Santos, and G. Modugno. *Observation of a dipolar quantum gas with metastable supersolid properties.* Phys. Rev. Lett. **122** 130405 (2019).

[135] G. Natale, R. M. Van Bijnen, A. Patscheider, D. Petter, M. J. Mark, L. Chomaz, and F. Ferlaino. *Excitation spectrum of a trapped dipolar supersolid and its experimental evidence.* Phys. Rev. Lett. **123** 050402 (2019).

[136] L. Tanzi, S. M. Roccuzzo, E. Lucioni, F. Famà, A. Fioretti, C. Gabbanini, G. Modugno, A. Recati, and S. Stringari. *Supersolid symmetry breaking from compressional oscillations in a dipolar quantum gas.* Nature **574** 382 (2019).

[137] G. Thalhammer, G. Barontini, J. Catani, F. Rabatti, C. Weber, A. Simoni, F. Minardi, and M. Lnguscio. *Collisional and molecular spectroscopy in an ultracold Bose-Bose mixture.* New J. Phys. **11** 055044 (2009).

[138] G. Barontini, C. Weber, F. Rabatti, J. Catani, G. Thalhammer, M. Inguscio, and F. Minardi. *Observation of heteronuclear atomic Efimov resonances.* Phys. Rev. Lett. **103** 043201 (2009).

[139] L. Wacker, N. B. Jørgensen, D. Birkmose, R. Horchani, W. Ertmer, C. Klempt, N. Winter, J. Sherson, and J. J. Arlt. *Tunable dual-species Bose-Einstein condensates of 39K and 87Rb.* Phys. Rev. A **92** 053602 (2015).

[140] T. A. Schulze, T. Hartmann, K. K. Voges, M. W. Gempel, E. Tiemann, A. Zenesini, and S. Ospelkaus. *Feshbach spectroscopy and dual-species Bose-Einstein condensation of 23Na - 39K mixtures.* Phys. Rev. A **97** 023623 (2018).

[141] L. Salasnich. *Dynamics of a Bose-Einstein condensate bright soliton in an expulsive potential.* Phys. Rev. A **70** 053617 (2004).

[142] S. Roy, M. Landini, A. Trenkwalder, G. Semeghini, G. Spagnolli, A. Simoni, M. Fattori, M. Inguscio, and G. Modugno. *Test of the universality of the three-body Efimov parameter at narrow Feshbach resonances.* Phys. Rev. Lett. **111** 053202 (2013).

[143] F. Chevy and C. Salomon. *Strongly correlated Bose gases* (2016).

[144] X. Antoine and R. Duboscq. *GPELab, a Matlab toolbox to solve Gross-Pitaevskii equations I: computation of stationary solutions.* Comput. Phys. Commun. **185** 2969 (2014).

[145] S. Falke, H. Knöckel, J. Friebe, M. Riedmann, E. Tiemann, and C. Lisdat. *Potassium ground-state scattering parameters and Born-Oppenheimer potentials from molecular spectroscopy.* Phys. Rev. A **78** 012503 (2008).

[146] V. Cikojević, L. V. Markić, G. E. Astrakharchik, and J. Boronat. *Universality in ultradilute liquid Bose-Bose mixtures.* Phys. Rev. A **99** 023618 (2019).

[147] T. Ilg, J. Kumlin, L. Santos, D. S. Petrov, and H. P. Büchler. *Dimensional crossover for the beyond-mean-field correction in Bose gases.* Phys. Rev. A **98** 051604(R) (2018).

[148] J. Boronat. *Private communications* .

[149] A. Di Carli, C. D. Colquhoun, G. Henderson, S. Flannigan, G. L. Oppo, A. J. Daley, S. Kuhr, and E. Haller. *Excitation modes of bright matter-wave solitons.* Phys. Rev. Lett. **123** 123602 (2019).

[150] G. Ferioli, G. Semeghini, L. Masi, G. Giusti, G. Modugno, M. Inguscio, A. Gallemí, A. Recati, and M. Fattori. *Collisions of self-bound quantum droplets.* Phys. Rev. Lett. **122** 090401 (2019).

[151] C. D'Errico, A. Burchianti, M. Prevedelli, L. Salasnich, F. Ancilotto, M. Modugno, F. Minardi, and C. Fort. *Observation of quantum droplets in a heteronuclear bosonic mixture.* arXiv:1908.00761 (2019).

[152] S. Burger, K. Bongs, S. Dettmer, W. Ertmer, K. Sengstock, A. Sanpera, G. V. Shlyapnikov, and M. Lewenstein. *Dark solitons in Bose-Einstein condensates.* Phys. Rev. Lett. **83** 5198 (1999).

[153] J. Denschlag. *Generating solitons by phase engineering of a Bose-Einstein condensate.* Science **287** 97 (2000).

[154] C. A. Sackett, H. T. Stoof, and R. G. Hulet. *Growth and collapse of a Bose-Einstein condensate with attractive interactions.* Phys. Rev. Lett. **80** 2031 (1998).

[155] J. L. Roberts, N. R. Claussen, S. L. Cornish, E. A. Donley, E. A. Cornell, and C. E. Wieman. *Controlled collapse of a Bose-Einstein condensate.* Phys. Rev. Lett. **86** 4211 (2001).

[156] C. Eigen, A. L. Gaunt, A. Suleymanzade, N. Navon, Z. Hadzibabic, and R. P. Smith. *Observation of weak collapse in a Bose-Einstein condensate.* Phys. Rev. X **6** 041058 (2016).

[157] P. A. Ruprecht, M. J. Holland, K. Burnett, and M. Edwards. *Time-dependent solution of the nonlinear Schrödinger equation for Bose-condensed trapped neutral atoms.* Phys. Rev. A **51** 4704 (1995).

[158] A. Gammal, T. Frederico, and L. Tomio. *Critical number of atoms for attractive Bose-Einstein condensates with cylindrically symmetrical traps.* Phys. Rev. A **64** 556021 (2001).

[159] V. M. Pérez-García, H. Michinel, J. I. Cirac, M. Lewenstein, and P. Zoller. *Dynamics of Bose-Einstein condensates: variational solutions of the Gross-Pitaevskii equations.* Phys. Rev. A - At. Mol. Opt. Phys. **56** 1424 (1997).

[160] A. Simoni. *Private communications* .

[161] M. Tomza. *Private communications* .

[162] I. Ferrier-Barbut, M. Wenzel, F. Böttcher, T. Langen, M. Isoard, S. Stringari, and T. Pfau. *Scissors mode of dipolar quantum droplets of Dysprosium atoms.* Phys. Rev. Lett. **120** (2018).

[163] J. H. Nguyen, P. Dyke, D. Luo, B. A. Malomed, and R. G. Hulet. *Collisions of matter-wave solitons.* Nat. Phys. **10** 918 (2014).

[164] G. E. Astrakharchik and B. A. Malomed. *Dynamics of one-dimensional quantum droplets.* Phys. Rev. A **98** 013631 (2018).

[165] Y. Li, Z. Chen, Z. Luo, C. Huang, H. Tan, W. Pang, and B. A. Malomed. *Two-dimensional vortex quantum droplets.* Phys. Rev. A **98** 063602 (2018).

[166] S. K. Adhikari. *Statics and dynamics of a self-bound matter-wave quantum ball.* Phys. Rev. A **95** 023606 (2017).

[167] S. Gautam and S. K. Adhikari. *Self-trapped quantum balls in binary Bose-Einstein condensates.* J. Phys. B **52** 055302 (2019).

[168] I. Bešlić, L. V. Markić, and J. Boronat. *Quantum Monte Carlo study of large spin-polarized Tritium clusters.* J. Chem. Phys. **131** 244506 (2009).

[169] A. Boudjemâa. *Quantum dilute droplets of dipolar bosons at finite temperature.* Ann. Phys. (N. Y). **381** 68 (2017).

[170] M. R. Matthews, B. P. Anderson, P. C. Haljan, D. S. Hall, M. J. Holland, J. E. Williams, C. E. Wieman, and E. A. Cornell. *Watching a superfluid untwist itself: recurrence of Rabi oscillations in a Bose-Einstein condensate.* Phys. Rev. Lett. **83** 3358 (1999).

[171] D. S. Petrov. *Three-body interacting bosons in free space.* Phys. Rev. Lett. **112** 103201 (2014).

[172] A. Cappellaro, T. Macrì, G. F. Bertacco, and L. Salasnich. *Equation of state and self-bound droplet in Rabi-coupled Bose mixtures.* Sci. Rep. **7** (2017).

[173] J. Sanz, A. Frölian, C. S. Chisholm, C. R. Cabrera, and L. Tarruell. *Interaction control and bright solitons in coherently-coupled Bose-Einstein condensates.* arXiv:1912.06041 (2019).

[174] A. Schirotzek, C. H. Wu, A. Sommer, and M. W. Zwierlein. *Observation of fermi polarons in a tunable fermi liquid of ultracold atoms*. Phys. Rev. Lett. **102** (2009).

[175] S. Inouye, M. R. Andrews, J. Stenger, H. J. Mlesner, D. M. Stamper-Kurn, and W. Ketterle. *Observation of Feshbach resonances in a Bose-Einstein condensate*. Nature **392** 151 (1998).

[176] M. Theis, G. Thalhammer, K. Winkler, M. Hellwig, G. Ruff, R. Grimm, and J. H. Denschlag. *Tuning the scattering length with an optically induced Feshbach resonance*. Phys. Rev. Lett. **93** 123001 (2004).

[177] K. Enomoto, K. Kasa, M. Kitagawa, and Y. Takahashi. *Optical Feshbach resonance using the intercombination transition*. Phys. Rev. Lett. **101** 203201 (2008).

[178] D. M. Bauer, M. Lettner, C. Vo, G. Rempe, and S. Dürr. *Control of a magnetic Feshbach resonance withlaser light*. Nat. Phys. **5** 339 (2009).

[179] Z. Fu, P. Wang, L. Huang, Z. Meng, H. Hu, and J. Zhang. *Optical control of a magnetic Feshbach resonance in an ultracold Fermi gas*. Phys. Rev. A **88** 041601(R) (2013).

[180] L. W. Clark, L. C. Ha, C. Y. Xu, and C. Chin. *Quantum dynamics with spatiotemporal control of interactions in a stable Bose-Einstein Condensate*. Phys. Rev. Lett. **115** 155301 (2015).

[181] A. Jagannathan, N. Arunkumar, J. A. Joseph, and J. E. Thomas. *Optical control of magnetic Feshbach resonances by closed-channel electromagnetically induced transparency*. Phys. Rev. Lett. **116** 075301 (2016).

[182] N. Arunkumar, A. Jagannathan, and J. E. Thomas. *Designer spatial control of interactions in ultracold gases*. Phys. Rev. Lett. **122** 040405 (2019).

[183] L. W. Clark, A. Gaj, L. Feng, and C. Chin. *Collective emission of matter-wave jets from driven Bose-Einstein condensates*. Nature **551** 356 (2017).

[184] H. Fu, L. Feng, B. M. Anderson, L. W. Clark, J. Hu, J. W. Andrade, C. Chin, and K. Levin. *Density waves and jet emission asymmetry in Bose fireworks.* Phys. Rev. Lett. **121** 243001 (2018).

[185] L. Feng, J. Hu, L. W. Clark, and C. Chin. *Correlations in high-harmonic generation of matter-wave jets revealed by pattern recognition.* Science **363** 521 (2019).

[186] A. Rapp, X. Deng, and L. Santos. *Ultracold lattice gases with periodically modulated interactions.* Phys. Rev. Lett. **109** 203005 (2012).

[187] S. Greschner, G. Sun, D. Poletti, and L. Santos. *Density-dependent synthetic gauge fields using periodically modulated interactions.* Phys. Rev. Lett. **113** 215303 (2014).

[188] B. D. Josephson. *Possible new effects in superconductive tunnelling.* Phys. Lett. **1** 251 (1962).

[189] S. V. Pereverzev, A. Loshak, S. Backhaus, J. C. Davis, and R. E. Packard. *Quantum oscillations between two weakly coupled reservoirs of superfluid 3He.* Nature **388** 449 (1997).

[190] K. Sukhatme, Y. Mukharsky, T. Chul, and D. Pearson. *Observation of the ideal josephson effect in superfluid 4He.* Nature **411** 280 (2001).

[191] J. H. Nguyen, D. Luo, and R. G. Hulet. *Formation of matter-wave soliton trains by modulational instability.* Science **356** 422 (2017).

[192] P. J. Everitt, M. A. Sooriyabandara, M. Guasoni, P. B. Wigley, C. H. Wei, G. D. McDonald, K. S. Hardman, P. Manju, J. D. Close, C. C. Kuhn, S. S. Szigeti, Y. S. Kivshar, and N. P. Robins. *Observation of a modulational instability in Bose-Einstein condensates.* Phys. Rev. A **96** https://journals.aps.org/pra/abstract/10.1103/Phys (2017).

[193] L. Landau, E. Lifshitz, V. Berestetskii, and L. Pitaevskii. *Quantum mechanics : non-relativistic theory.* Pergamon, London.

[194] H. Bethe and R. Peierls. *Quantum theory of the diplon.* Proc. R. Soc. London. Ser. A **148** 146 (1935).

[195] E. W. Hansen and P.-L. Law. *Recursive methods for computing the Abel transform and its inverse.* J. Opt. Soc. Am. A **2** 510 (1985).

[196] J. R. Gascooke. *Energy transfer in polyatomic-rare gas collisions and van der Waals molecule dissociation.* Ph.D. thesis, Flinders University (2000).

[197] V. Dribinski, A. Ossadtchi, V. A. Mandelshtam, and H. Reisler. *Reconstruction of Abel-transformable images: the Gaussian basis-set expansion Abel transform method.* Rev. Sci. Instrum. **73** 2634 (2002).

[198] N. R. Thomas, N. Kjærgaard, P. S. Julienne, and A. C. Wilson. *Imaging of s and d partial-wave interference in quantum scattering of identical bosonic atoms.* Phys. Rev. Lett. **93** 173201 (2004).

[199] U. Al Khawaja, H. T. Stoof, R. G. Hulet, K. E. Strecker, and G. B. Partridge. *Bright soliton trains of trapped Bose-Einstein condensates.* Phys. Rev. Lett. **89** 200404 (2002).

[200] L. Salasnich, A. Parola, and L. Reatto. *Modulational instability and complex dynamics of confined matter-wave solitons.* Phys. Rev. Lett. **91** https://journals.aps.org/prl/abstract/10.1103/Phys (2003).

[201] L. D. Carr and J. Brand. *Spontaneous soliton formation and modulational instability in Bose-Einstein condensates.* Phys. Rev. Lett. **92** 4 (2004).

[202] L. D. Carr and J. Brand. *Pulsed atomic soliton laser.* Phys. Rev. A **70** 033607 (2004).

[203] P. Tommasini, E. J. De Passos, A. F. De Toledo Piza, M. S. Hussein, and E. Timmermans. *Bogoliubov theory for mutually coherent condensates.* Phys. Rev. A **67** 023606 (2003).

[204] D. S. Petrov and A. Recati. *Private communications* .

[205] M. J. Edmonds, M. Valiente, G. Juzeliunas, L. Santos, and P. Öhberg. *Simulating an interacting gauge theory with ultracold Bose gases.* Phys. Rev. Lett. **110** 085301 (2013).

[206] A. L. Gaunt, T. F. Schmidutz, I. Gotlibovych, R. P. Smith, and Z. Hadzibabic. *Bose-Einstein condensation of atoms in a uniform potential.* Phys. Rev. Lett. **110** 200406 (2013).

[207] B. Mukherjee, Z. Yan, P. B. Patel, Z. Hadzibabic, T. Yefsah, J. Struck, and M. W. Zwierlein. *Homogeneous Atomic Fermi Gases.* Phys. Rev. Lett. **118** 123401 (2017).

[208] M. Aidelsburger, J. L. Ville, R. Saint-Jalm, S. Nascimbène, J. Dalibard, and J. Beugnon. *Relaxation dynamics in the merging of N independent condensates.* Phys. Rev. Lett. **119** 190403 (2017).

[209] J. L. Ville, R. Saint-Jalm, Le Cerf, M. Aidelsburger, S. Nascimbène, J. Dalibard, and J. Beugnon. *Sound propagation in a uniform superfluid two-dimensional Bose gas.* Phys. Rev. Lett. **121** 145301 (2018).

[210] D. Petter, G. Natale, R. M. Van Bijnen, A. Patscheider, M. J. Mark, L. Chomaz, and F. Ferlaino. *Probing the roton excitation spectrum of a stable dipolar Bose gas.* Phys. Rev. Lett. **122** 183401 (2019).

[211] A. Frölian. *Coherently-coupled Bose-Einstein condensates with tunable interactions.* PhD thesis proposal, Institut de Ciències Fotòniques, Universitat Politècnica de Catalunya (2019).

[212] L. W. Cheuk, A. T. Sommer, Z. Hadzibabic, T. Yefsah, W. S. Bakr, and M. W. Zwierlein. *Spin-injection spectroscopy of a spin-orbit coupled Fermi gas.* Phys. Rev. Lett. **109** 095302 (2012).

[213] L. Huang, Z. Meng, P. Wang, P. Peng, S. L. Zhang, L. Chen, D. Li, Q. Zhou, and J. Zhang. *Experimental realization of two-dimensional synthetic spin-orbit coupling in ultracold Fermi gases.* Nat. Phys. **12** 540 (2016).

[214] X. T. Xu, C. R. Yi, B. Z. Wang, W. Sun, Y. Deng, X. J. Liu, S. Chen, and J. W. Pan. *Precision mapping the topological bands of 2D spin-orbit coupling with microwave spin-injection spectroscopy.* Sci. Bull. **63** 1464 (2018).

[215] M. J. Edmonds, M. Valiente, and P. Öhberg. *Elementary excitations of chiral Bose-Einstein condensates.* EPL **110** 36004 (2015).

[216] M. Ballu. *Développment d'un système laser Raman pour le couplage cohérent de deux condensats de Bose-Einstein de potassium.* Master thesis, Institut de Ciències Fotòniques (2018).

Declaration

I declare that this thesis has been composed solely by myself and that it has not been submitted, as a whole or in part, in any previous application for a degree. I confirm that appropriate credit has been given within this thesis where reference has been made to the work of others.

Barcelona, January 2020

Julio Sanz Sánchez